The Pennsylvania State University

The Graduate School

Department of Materials Science and Engineering

# CHEMICAL SOLUTION DEPOSITION OF SILVER TANTALATE NIOBATE, $Ag(Ta_xNb_{1-x})O_3$, THIN FILMS

A Thesis in

Materials Science and Engineering

by

Mustafa Burak Telli



Submitted in Partial Fulfillment
of the Requirements
for the Degree of

Doctor of Philosophy

May 2005

The thesis of Mustafa Burak Telli was reviewed and approved* by the following:

Susan Trolier-McKinstry
Professor of Ceramic Science and Engineering
Thesis Advisor
Chair of Committee

Clive A. Randall
Professor of Materials Science and Engineering

Michael Lanagan
Associate Professor of Engineering Science and Mechanics and Materials Science and Engineering

Jerzy Ruzyllo
Professor of Electrical Engineering

James Runt
Professor of Polymer Science
Associate Head for Graduate Studies

*Signatures are on file in the Graduate School

## ABSTRACT

Chemical solution deposited $Ag_x(Ta_yNb_{1-y})O_z$ thin films on (111)Pt/Ti/$SiO_2$/(001)Si, (001)$LaAlO_3$, (001)$SrRuO_3$/(001)$LaAlO_3$, Ag, Ag/$SiO_2$/(001)Si and Ag/Ti/$SiO_2$/(001)Si substrates are investigated. Deposition of the films involved synthesis of stable chemical solutions, spinning and heat treatments of the spun layers.

$Ag(Ta_{0.5}Nb_{0.5})O_3$ (ATN) films that were deposited on (111)Pt/Ti/$SiO_2$/(001)Si (Pt/Si) substrates contained a minimum of two phases: a randomly oriented pseudocubic perovskite and a (00*l*) oriented natrotantite phase. The dielectric constants of the two phase ATN films with a max of ~270±25 were lower than that observed for ceramics ~ 410 at room temperature and at 100 kHz. Natrotantite films had lower dielectric constants (70 to 135) than those with the perovskite structure.

$Ag(Ta_{0.5}Nb_{0.5})O_3$ (ATN), $AgTaO_3$ (ATO) and $AgNbO_3$ (ANO) films that were prepared on (001)$LaAlO_3$ (LAO) and (001)$SrRuO_3$/(001)$LaAlO_3$ (SRO/LAO) substrates had all (00*l*) epitaxial perovskite phases at crystallization temperatures of 500 °C and above. With an increase in crystallization temperature from 500 °C to 800 °C, the dielectric constants of ATN films on SRO/LAO substrates were increased from 260±25 to 360±35 at 100 kHz at room temperature and crystallinity of the films were improved. The DC field tunability of ATN film was not hysteretic but small, 4.8 % at 100 kHz and 150 kV/cm. While ATO film had a slightly lower dielectric constant of 110±10 than the bulk ceramic value of 150, the ANO film had high room temperature permitivities of 550±55 than the bulk ceramic value of 120 at 100 kHz and at room temperature. Although the DC field tunability of ATO film was not hysteretic but limited to 1.6 % at

100 kHz and at 230 kV/cm field, the DC field tunability of the ANO film was higher, with a 12.8 % at a negative bias of -140 kV/cm and 21.4 % at 190 kV/cm.

When $Ag(Ta_{0.5}Nb_{0.5})O_3$ thin films that were deposited on Ag foils, $Ag/SiO_2/Si$ and $Ag/Ti/SiO_2/Si$ substrates at temperatures from 550 to 750 °C, they did not have any extensive reaction with silver and the orientation of the films was dependent on the substrate used as well as the followed heat treatment steps.

# TABLE OF CONTENTS

## LIST OF FIGURES

# LIST OF TABLES

## ACKNOWLEDGEMENTS

I would like to thank to Prof. Susan Trolier-McKinstry and my Ph. D. committee members, for their guidance and mentorship, to my beautiful wife for her patience, to my two smart kids for making my life enjoyable, to STM group members for surviving my bad jokes and to MRL staff for teaching me about practical aspects of the research.

*Dedicated to*

*My beautiful wife, Guler Telli*

*and my two smart  kids, Meltem and Mert Telli*

# Chapter 1

# Introduction

## 1.1 Background:

New tunable dielectric thin films having temperature stable high dielectric permittivity and low loss at microwave frequencies (1 to 40 GHz) are required for next generation wireless telecommunication applications such as satellite broadcasting, radar antennas and cell phones.[1] While stability in the dielectric properties of the films between -55 to 125 °C is important to minimize the effect of temperature on devices like tunable filters and phase shifters, a high dielectric constant ($\varepsilon_r$ >20) enables miniaturization of the devices. For example, the dimensions of a tunable filter depends linearly on the wavelength of the electromagnetic wave propagating in the dielectric medium, which is inversely related to the square root of the dielectric permittivity (Equation **1.1**).[2]

$$l = \frac{c}{f_0\sqrt{\varepsilon}} \qquad \text{(Equation 1.1)}$$

where:

$l$ = Wavelength of electromagnetic wave in dielectric medium.

$c$ = Speed of light in vacuum, $3\text{x}10^8$ m/s.

$f_0$ =Frequency of electromagnetic wave.

It is possible to tune the response of microwave devices by using semiconductor varactors, ferrites or voltage tunable dielectric films.[3] For example, Figure **1.1** shows the change in the transmission ($S_{21}$) and reflectance ($S_{11}$) characteristics of a tunable 3-pole band-pass filter by applying DC bias to the flip chip planar capacitors utilizing a tunable dielectric film.[2, 4] The performance of semiconductor varactors suffers at high frequencies (>10 GHz) due to their poor power handling capabilities and high losses.[3] Tunable devices based on ferrites require expensive, power consuming circuitry; therefore their usage is limited to only high–cost applications.[3, 5] On the contrary, dielectric thin films need lower power levels for tuning and are cheaper to produce.[3] Consequently, this literature review will focus on tunable dielectrics.

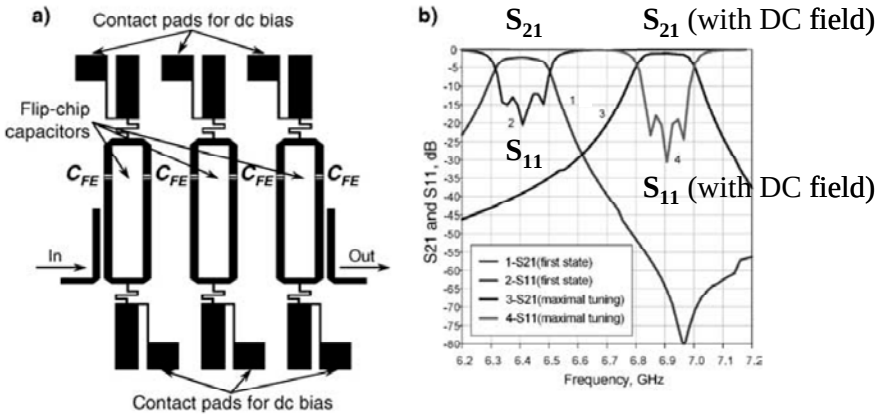


Figure **1.1**: Layout of a tunable 3-pole filter and simulated transmission ($S_{21}$) and reflection ($S_{11}$) coefficients at different values of DC bias.[2, 4]

Both high dielectric tunability, the relative change in dielectric permittivity with applied DC bias field (Equation **1.2**), and low loss are necessary for a tunable dielectric material.[2] This is shown in one of the figures of merit for the quality of a tunable dielectric material. The K factor is calculated by taking the ratio of the tunability ($n_r$) to the loss (Equation **1.3**).[3] In order to have a high K factor, a high tunability and a low loss are needed together.

$$n_r = \frac{\varepsilon(0) - \varepsilon(E_0)}{\varepsilon(0)} \qquad \text{(Equation 1.2)}$$

where;

$\varepsilon(0)$: Dielectric permittivity without a DC field bias.

$\varepsilon(E_0)$: Dielectric permittivity at DC field bias level of $E_0$.

$$K = \frac{\varepsilon(0) - \varepsilon(E_0)}{\varepsilon(0)\tan\delta_0} \qquad \text{(Equation 1.3)}$$

where;

$\tan\delta_0$: Loss without DC bias.

Most candidate tunable dielectrics belong to the paraelectric phase of a ferroelectric material having high dielectric permittivity.[2] This is because high tunabilities are generally correlated with high dielectric constants and paraelectric phases

have lower losses than the corresponding ferroelectric phases due to the elimination of domain wall contributions to the loss.[2] It should be noted that use of a ferroelectric phase might be possible for frequencies higher than 20 GHz, since losses associated with domain wall motions or piezoelectric responses are usually not observed at these frequencies.[5] In general, ferroelectric materials showing relaxor behavior are often not desirable for tunable applications because of large decreases seen in dielectric constants and large increases seen in losses at high frequencies (GHz).[2, 6]

A ferroelectric relaxor material shows a diffuse ferroelectric-paraelectric phase transition where the maximum in dielectric constant is broad and takes place over a temperature range.[7] In addition, the dielectric maximum of a ferroelectric relaxor is strongly frequency dependent in the range of 1kHz to 1 MHz and an increase in the frequency leads a shift in the position of the dielectric maximum to higher temperature.[7] Figure **1.2** shows temperature dependent dielectric properties as a function of frequency of a candidate dielectric material, perovskite $Ba(Ti_{0.90}Ga_{0.05}Nb_{0.05})O_3$ ceramics showing dielectric relaxation.[8]

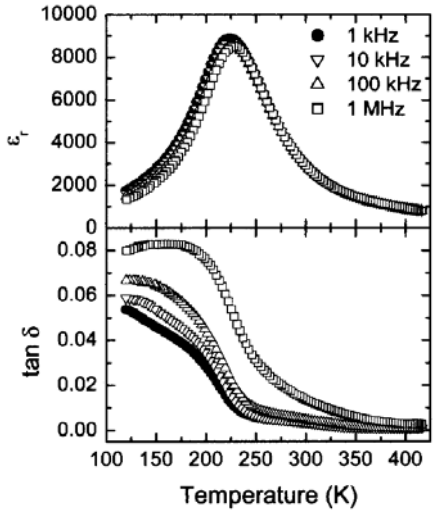


Figure **1.2**: Temperature dependence of dielectric constant and loss as a function of frequency for a $Ba(Ti_{0.90}Ga_{0.05}Nb_{0.05})O_3$ ceramic.[8]

$(Ba_{1-x}Sr_x)TiO_3$, (BST), with compositions near x=0.4 is the most investigated bulk tunable dielectric material because of the relatively high tunabilities observed around room temperature. Table **1.1** shows the dielectric properties of some of the BST compositions as well as some alternative tunable dielectric materials described in the literature. Although BST ceramics have high tunabilities, they can also have high loss values and their dielectric properties (including tunability) are strongly temperature dependent due to the ferroelectric-paraelectric phase transition (Figure **1.3**). The tunabilities of several other candidate materials such as $Ba(Ti_{0.90}Ga_{0.05}Nb_{0.05})O_3$, the paraelectric cubic perovskites $Ba(Zr_{0.2}Ti_{0.8})O_3$, $Ba(Ti_{0.85}Sn_{0.15})O_3$ and the paraelectric pyrochlore $Cd_2Nb_2O_7$ are also high. But, their loss values are high and the dielectric properties are temperature dependent as well. For $Ba(Ti_{0.90}Ga_{0.05}Nb_{0.05})O_3$ ceramics

showing dielectric relaxor behavior, a decrease in dielectric permittivity and an increase in loss was observed with an increase in frequency to GHz range. In the case of the $Ba(Ti_{0.85}Sn_{0.15})O_3$, $Ba(Zr_{0.2}Ti_{0.8})O_3$ and $Cd_2Nb_2O_7$ ceramics, the high frequency dielectric properties are not reported.

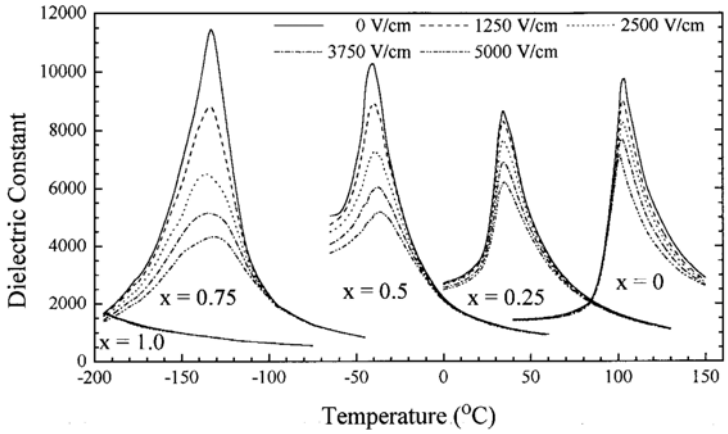


Figure **1.3**: Dielectric permittivity of $(Ba_{1-x}Sr_x)TiO_3$ ceramics as function of temperature, composition and DC bias at 10 kHz.[9]

Table **1.1**: Dielectric properties of some of the candidate tunable dielectric materials

| Material | $\varepsilon_r$ | Tunability (%) | Freq. | Temp. (K) | DC Bias (kV/cm) | Loss (tanδ) | Ref. |
|---|---|---|---|---|---|---|---|
| $SrTiO_3$ | 8000 | 70 | 1 kHz | 35 | 10 | 0.001 | 10 |
| $(Ba_{0.6}Sr_{0.4})TiO_3$ | 8000 | 70 | 10 kHz | 273 | 16 | 0.012 | 11 |
| $(Ba_{0.8}Sr_{0.2})TiO_3$ | 8500 | 55 | 1 MHz | 330 | 5 | 0.016 | 12 |
| $Ba(Ti_{0.90}Ga_{0.05}Nb_{0.05})O_3$ | 8700 | 70 | 10 kHz | 265 | 20 | 0.008 | 8 |
| $Ba(Zr_{0.2}Ti_{0.8})O_3$ | 8000 | 86 | 10 kHz | 300 | 20 | 0.011 | 13 |
| $Ba(Ti_{0.85}Sn_{0.15})O_3$ | 8500 | 55 | 10 kHz | 298 | 7.6 | 0.008 | 14 |
| $Cd_2Nb_2O_7$ | 1100 | 64 | 5 kHz | 80 | 15 | 0.016 | 15 |

Thin films only require lower voltages for tuning and are potentially easier to integrate with other circuitry compared to bulk dielectrics.[2, 3] However, the dielectric properties of thin films depends on the substrates used for deposition and are often different than the dielectric properties of bulk ceramics due to interfacial chemical reactions, diffusion between the film and substrate, large levels of in-plane stress, built-in electric fields, passive layers at the film – electrode interface, or clamping of the film by the substrate.[16, 17] For an example, 70 nm thick $Ba_{0.7}Sr_{0.3}TiO_3$ films deposited on $Pt/SiO_2/Si$ substrate have high tunabilities (71% observed at 1300 kV/cm DC field) and K-factors (~88.8 observed at 1300 kV/cm DC field) but the field levels are typically far higher in films than in bulk ceramics in order to obtain the same tunability.[18] The dielectric properties, including the tunability of the films show strong temperature (Figure **1.4**) and thickness dependence (Figure **1.5**).[19, 20] While temperature dependence is expected due to the ferroelectric-paraelectric phase transition, the thickness dependence

typically arises (at least in part) from formation of thin surface layers having poor dielectric properties.[2, 20]

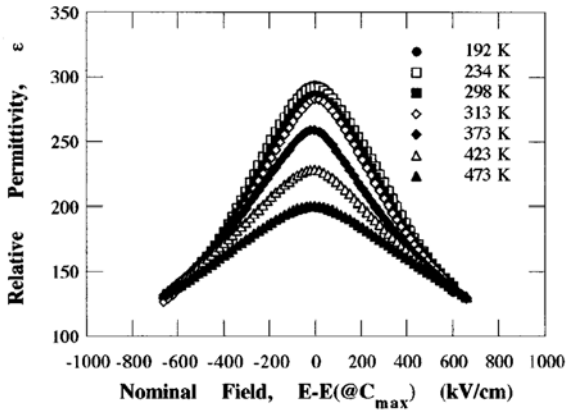


Figure **1.4**: Tunability of 50 nm thick $Ba_{0.7}Sr_{0.3}TiO_3$ film as a function of temperature. The film was deposited on $Pt/SiO_2/Si$ substrates and measurements were performed at 1 kHz with evaporated Pt top electrodes.[19]

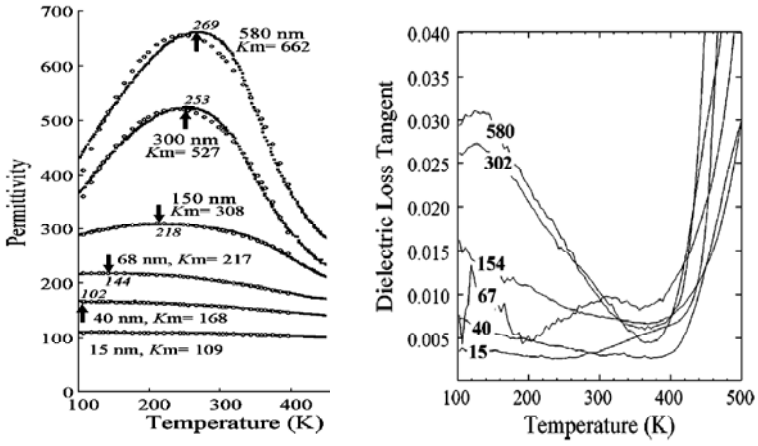


Figure **1.5**: Temperature dependence of dielectric constant and loss for $Ba_{0.7}Sr_{0.3}TiO_3$ films having different thickness. Films were deposited on $Pt/SiO_2/Si$ substrates and measurements were performed at 4 kHz with sputtered Pt top electrodes.[20]

Thin films of bismuth zinc niobate (BZN) pyrochlores and zirconolites have also been investigated in the literature.[21, 22] Table **1.2** shows the dielectric properties and tunabilities of BZN pyrochlores and zirconolite thin films that were deposited on $Pt/SiO_2/Si$ substrates. The BZN films show relatively high tunabilities (as high as 55 % for the cubic pyrochlores) and low losses (<0.005), but requires relatively high electric fields (>1800 kV/cm). However, cubic pyrochlore $Bi_{1.5}Zn_{1.0}Nb_{1.5}O_7$ ceramics (for which the highest tunabilities were observed in thin film form) show temperature and frequency dependent dielectric relaxation.[23] With an increase in frequency to GHz region or above, an increase in loss and decrease in dielectric permittivity was observed for the $Bi_{1.5}Zn_{1.0}Nb_{1.5}O_7$ ceramics at room temperature (Figure **1.6**).[24]

Table **1.2**: Dielectric properties of bismuth zinc niobate thin films

| Composition | Structure | $\varepsilon_r$ | Tunability (%) | DC Bias (kV/cm) | Loss (tanδ) | Freq. (kHz) | Ref. |
|---|---|---|---|---|---|---|---|
| $Bi_{1.5}Zn_{1.0}Nb_{1.5}O_{6.5}$ | Pyrochlore | 180 | 26 | 1800 | 0.002 | 10 | 20 |
| $Bi_{1.5}Zn_{1.0}Nb_{1.5}O_7$ | Pyrochlore | 150 | 45 | 3000 | 0.005 | 10 | 20 |
| $Bi_{1.5}Zn_{1.05}Nb_{1.5}O_{7.05}$ | Pyrochlore | 200 | 55 | 2400 | 0.0005 | 1000 | 21 |
| $Bi_2Zn_{2/3}Nb_{4/3}O_7$ | Zirconolite | 80 | 20 | 4000 | 0.005 | 10 | 20 |

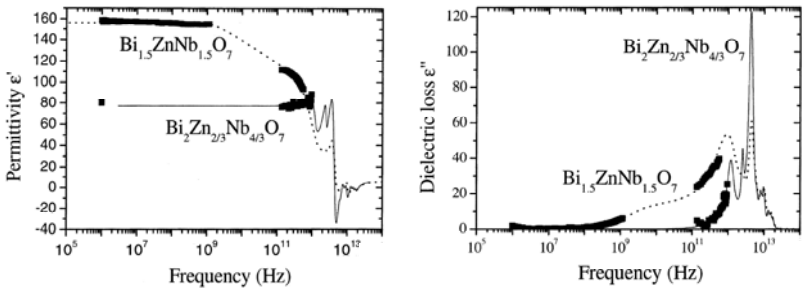


Figure **1.6**: Frequency dependent dielectric properties of bismuth zinc niobate ceramics.[24]

Silver tantalate niobate, $Ag(Ta_xNb_{1-x})O_3$, has been proposed as an alternative dielectric with modest tunability and good dielectric properties at microwave frequencies. $Ag(Ta_xNb_{1-x})O_3$ ceramics, where $0.4 \leq x \leq 0.6$, show reasonably temperature stable properties (Figure **1.7**) and high dielectric constants (around 400) at room temperature with little frequency dispersion up to 100 GHz.[25, 26] $Ag(Ta_{0.5}Nb_{0.5})O_3$ has a dielectric constant of ~410 and a $Q_0$*f of 770 GHz at 2 GHz at room temperature with a capacitance change, $\Delta C/C$, of less than 8 % over the temperature range of –20 to 120 °C at 1 MHz.[27, 28] Table **1.3** shows the tunabilities of some $Ag(Ta_xNb_{1-x})O_3$ ceramics.[29]

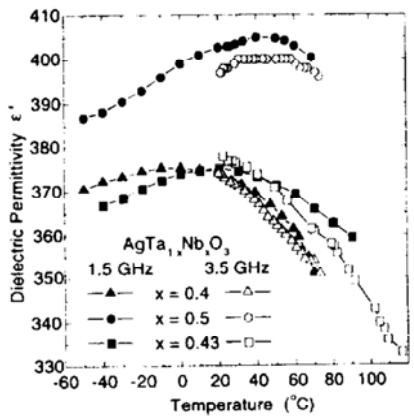


Figure **1.7**: Dielectric permittivity of $Ag(Ta_{1-x}Nb_x)O_3$ ceramics having compositions near x=0.5 as a function of temperature and composition at 1.5 and 3.5 GHz.[27]

Table **1.3**: Tunabilities of $Ag(Ta_xNb_{1-x})O_3$ ceramics at 100 kHz.[29]

| Composition | $\varepsilon_r$ | Tunability (%) | Temp. (°C) | DC Bias (kV/cm) | Loss (tanδ) |
|---|---|---|---|---|---|
| $Ag(Ta_{0.2}Nb_{0.8})O_3$ | 370 | 27 | -26 | 8 | <0.014 |
| $Ag(Ta_{0.1}Nb_{0.9})O_3$ | 300 | 16 | 17 | 10 | <0.015 |

$Ag(Ta_xNb_{1-x})O_3$ ceramics have derivatives of the cubic perovskite crystal structure (Figure **1.8**) and show several cell distortions, originally identified as monoclinic (M), tetragonal (T), orthorhombic (O) and rhombohedral (R), as a function of composition and temperature (Figure **1.9**).[30] Table **1.4** shows the lattice parameters of $AgTaO_3$, $Ag(Ta_{0.5}Nb_{0.5})O_3$ and $AgNbO_3$ ceramics at room temperature. For a $Ag(Ta_{0.5}Nb_{0.5})O_3$ ceramic, the phase transition sequence is as follows; cubic to tetragonal

at ~560 °C, tetragonal to orthorhombic at ~400 °C, orthorhombic to $M_3$ at ~360 °C, $M_3$ to $M_2$ at ~50 °C and $M_2$ to $M_1$ at ~0 °C.[30] The low temperature $M_1$, $M_2$ and $M_3$ phases were reported to have monoclinic crystal structures in early studies, but a recent neutron diffraction study suggests that these phases might all belong to the orthorhombic crystal class.[31]

Table **1.4**: Unit cell parameters of $Ag(Ta_xNb_{1-x})O_3$ ceramics at room temperature. [31, 32, 33]

| Composition | Unit Cells | Lattice Parameters | Angles |
|---|---|---|---|
| $AgTaO_3$ | Rhombohedral (R) | a : 3.928 Å | α=89.30° |
| $Ag(Ta_{0.5}Nb_{0.5})O_3$ | Monoclinic ($M_2$) | a : 3.929 Å<br>b: 3.926 Å<br>c: 3.930 Å | α=γ : 90.00°<br>β: 90.49° |
| $AgNbO_3$ | Monoclinic ($M_1$) | a : 3.929 Å<br>b: 3.926 Å<br>c: 3.930 Å | α=γ : 90.00°<br>β: 90.52° |
| $AgNbO_3$ | Orthorhombic | a : 5.547 Å<br>b: 5.604 Å<br>c: 15.642 Å | α=γ=β : 90.00° |

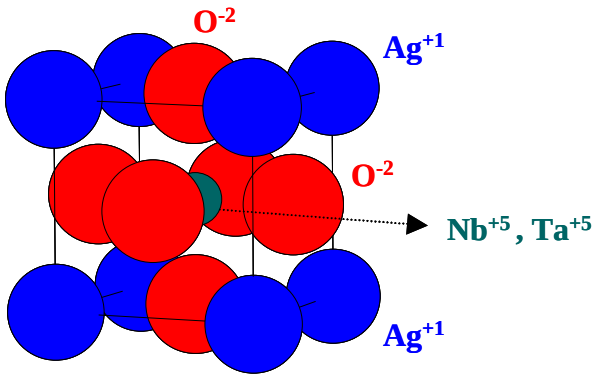


Figure **1.8**: Pseudocubic perovskite crystal structure of silver tantalate niobate.

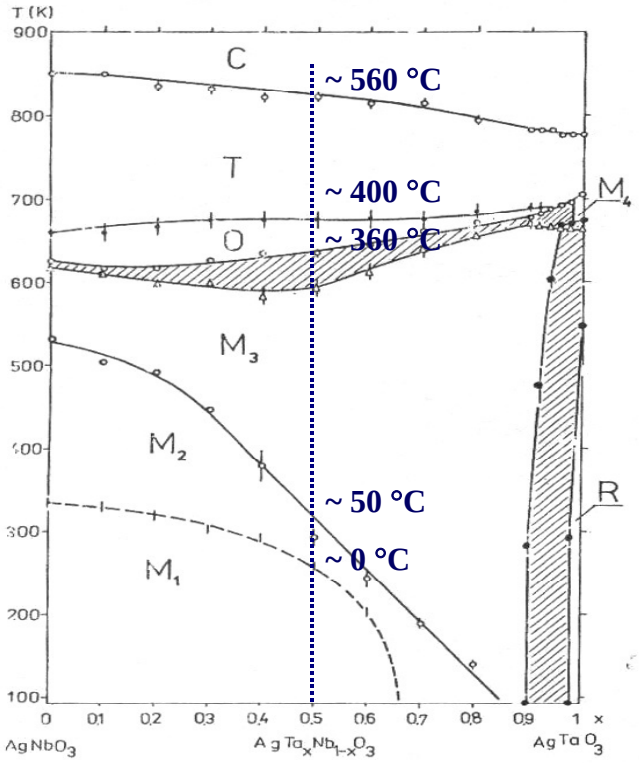


Figure **1.9**: Phase diagram of silver tantalate niobate, $Ag(Ta_xNb_{1-x})O_3$ ceramics.[30]

The dielectric properties of $Ag(Ta_xNb_{1-x})O_3$ ceramics depend on the crystal distortion and the composition. The high temperature T and O phases are reported to be paraelectric, the $M_3$ and $M_2$ phases to be antiferroelectric, and the $M_1$ and R phases as weakly ferroelectric.[27, 34] The nature of $M_4$ is not reported as yet. Paraelectric orthorhombic (O) and tetragonal (T) distortions are explained based on oxygen octahedral tilts.[22] In contrast, the M distortions are believed to be due to different states of Nb ion displacements from the center of the tilted oxygen octahedra.[30, 35] The diffuse nature of the $M_3$-$M_2$ and $M_2$-$M_1$ phase transitions were suggested to be due to the disorder in Nb ion displacements.[30, 35] In addition, the $M_1$ phase showed tunability in the dielectric constant (Figure **1.10**).[29]

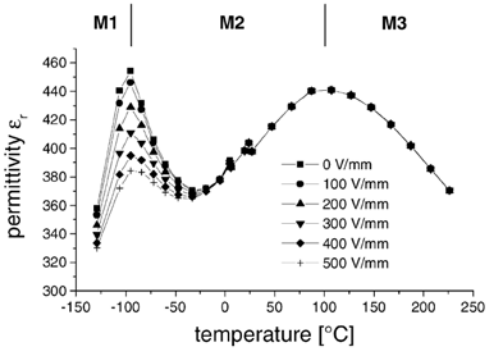


Figure **1.10**: Temperature and DC field dependence of $Ag(Ta_{0.4}Nb_{0.6})O_3$ ceramics at 100 kHz.[29]

The composition of $Ag(Ta_xNb_{1-x})O_3$ ceramics, namely the Nb/Ta ratio, greatly affects the dielectric properties and their temperature dependence (Figure **1.11**).[36] While

$AgTaO_3$ has a dielectric constant of ~150 at 1 MHz at room temperature with only a slight decrease with an increase in temperature, the compositions having higher niobium contents have higher dielectric constants and show stronger temperature dependence. There are two dielectric permittivity maxima that are more clearly seen for higher Nb concentrations corresponding to the phase transitions between $M_3$-O and $M_2$-$M_3$ distortions. The diffuse $M_2$-$M_3$ phase transition occurs close to room temperature for $Ag(Ta_xNb_{1-x})O_3$ ceramics having compositions of $0.4 \leq x \leq 0.6$ resulting in high dielectric constants about 400 and modest temperature stability.[27, 36] For compositions having higher niobium contents, the $M_2$-$M_3$ phase transition occurs at higher temperatures, and is associated with higher peak dielectric constants. In $AgNbO_3$ ceramics, the dielectric constant is ~120 at 1 MHz at room temperature and it increases continuously to ~700 at 270 °C where the $M_2$-$M_3$ phase transition occurs. After a slight decrease with temperature, the dielectric constant of $AgNbO_3$ ceramics increases sharply to ~850 at ~370 °C with the $M_3$-O phase transition and drops rapidly with further increase in temperature.

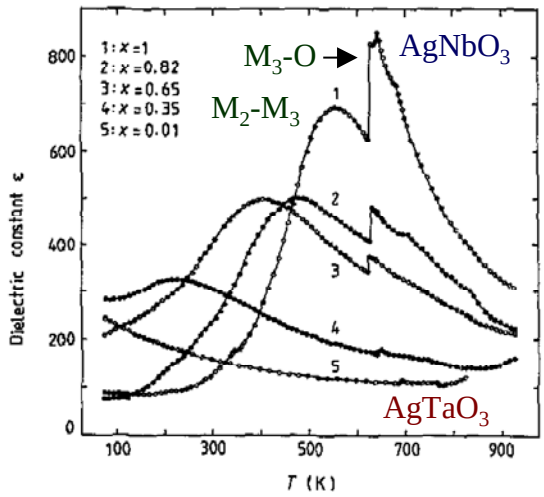


Figure **1.11**: Temperature dependent dielectric permittivities of $Ag(Nb_xTa_{1-x})O_3$ ceramics at 1 MHz.[36]

When a dielectric material is introduced into an electric field, electric charges appear on the surface of the insulator and this phenomenon is known as dielectric polarization.[37] The polarization (P) is defined as the surface charge density of the bound charges on the capacitor plates (which have the same value but the opposite sign of the induced charges on the surface of the dielectric) and can be written in terms of the applied electric field and the dielectric constant of the insulator (Equation **1.2**).[37, 38] The polarization also corresponds to the dipole moment per unit volume and can be written in terms of the local electric field, polarizability and number of dipoles per unit volume (Equation **1.3**).[38] The polarizability is the proportionality factor between the induced dipole moment and the applied local electric field and is a measure of the average dipole moment per unit of local electric field strength.[38] In the case of only ionic and electronic

polarizations, the Clausius-Mossotti equation relates the atomic polarizability and the dielectric constant (Equation **1.4**).[38, 39]

$$P = \varepsilon_0(\varepsilon_r - 1)E \qquad \text{(Equation 1.2)}$$

where:

$\varepsilon_0$ : Permittivity of free space

$\varepsilon_r$ : Dielectric constant

$E$ : Applied electric field

$$P = N\alpha E' \qquad \text{(Equation 1.3)}$$

where:

$N$ : Number of dipoles per unit volume

$\alpha$ : Polarizability

$E'$ : Local electric field

$$\frac{N\alpha}{3\varepsilon_0} = \frac{\varepsilon_r - 1}{\varepsilon_r + 2} \qquad \text{(Equation 1.4)}$$

The temperature coefficient of capacitance ($\tau_C$) and permittivity ($\tau_\varepsilon$) describe the change in capacitance and in dielectric permittivity, respectively with temperature. They are calculated using Equation **1.5** and Equation **1.6**.[40] For a parallel plate capacitor,

$\tau_C$ can be written in terms of $\tau_\varepsilon$ and the linear expansion coefficient ($\alpha_L$) (Equation **1.7**).[40]

$$\tau_C = \frac{1}{C}\frac{\partial C}{\partial T} \qquad \text{(Equation 1.5)}$$

$$\tau_\varepsilon = \frac{1}{\varepsilon}\left(\frac{\partial \varepsilon}{\partial T}\right) \qquad \text{(Equation 1.6)}$$

$$\tau_C = \tau_\varepsilon + \alpha_L \qquad \text{(Equation 1.7)}$$

$\tau_C$ can also be written in terms of the dielectric permittivity, the linear expansion coefficient ($\alpha_L$) and derivatives of the macroscopic polarizability ($\alpha_L$) (Equation **1.8** derived by using the Clausius-Mossotti equation).[41] Due to volume dependent terms, $\tau_C$ is sensitive to any phase transitions involving slight volume changes.[41] For example, in $Ba_xSr_{1-x}(Zn_{1/3}Nb_{2/3})O_3$ ceramics, octahedra tilt transitions and the appearance of ferroelastic domains results in changes in the $\tau_C$ values (Figure **1.12**).[42] The first octahedra tilt transition from high temperature cubic phase produces a minimum in $\tau_C$, formation of ferroelastic domains leads to a local sharp maximum and a phase transition involving change in oxygen octahedra tilts produces a jump in $\tau_C$ to positive values.[42]

It may not be possible to observe such a $\tau_C$ response for the low temperature M phase transitions in $Ag(Ta_xNb_{1-x})O_3$ ceramics. This is because the M phase transitions are believed to be due to different states of Nb ion displacements from the center of the same tilted oxygen octahedra.[30, 31, 35]

$$\tau_C = \frac{(\varepsilon_r - 1)(\varepsilon_r + 2)}{\varepsilon_r}(-\alpha_L + B + C) + 0.05\tan\delta + \alpha_L$$
$$B = \frac{1}{3\alpha_m}\left(\frac{\partial\alpha_m}{\partial V}\right)_T\left(\frac{\partial V}{\partial T}\right)_P, C = \frac{1}{3\alpha_m}\left(\frac{\partial\alpha_m}{\partial T}\right)_V \quad \text{(Equation 1.8)}$$

where:

$\alpha_m$ : Polarizability of a macroscopic small sphere of volume V

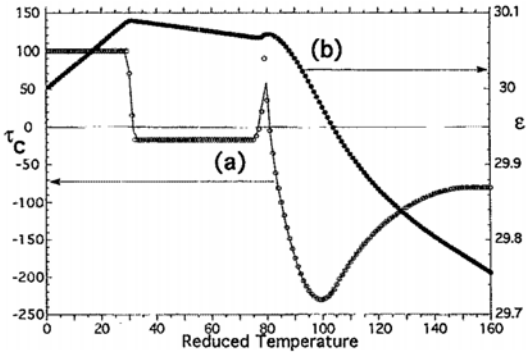


Figure 1.12: Schematic showing temperature dependent $\tau_C$ response observed for $Ba_xSr_{1-x}(Zn_{1/3}Nb_{2/3})O_3$ ceramics (a) and expected behavior of the relative permittivity calculated from as the integral of the $\tau_C$ (b).[42]

The dielectric properties depend on the frequency (Figure **1.13**) and for microwave frequencies (1-100 GHz), the polarization mechanisms contributing to the dielectric permittivity are dipolar, ionic and electronic.[43] For $Ag(Ta_xNb_{1-x})O_3$ ceramics, the main ionic polarization mechanism was attributed to the presence of Nb ions and Nb-O vibrations, but the exact nature of the Nb ion motions still remains unclear.[27, 36, 44] Figure **1.14** shows the high frequency dielectric properties for some $Ag(Ta_xNb_{1-x})O_3$ ceramics.[44]

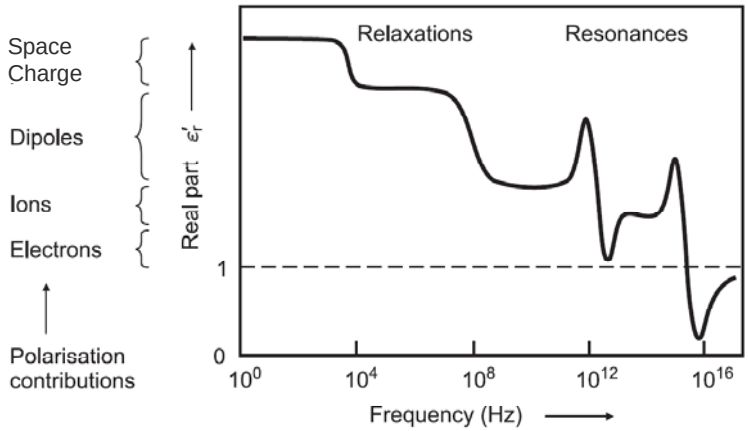


Figure **1.13**: Frequency dependence of generic polarization mechanisms contributing to dielectric permittivity.[43]

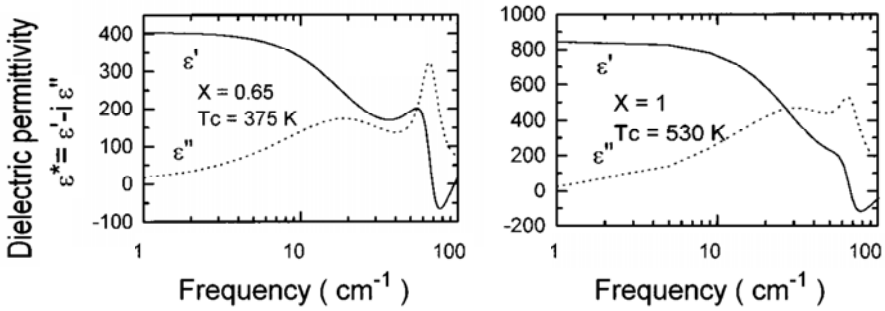


Figure **1.14**: High frequency dielectric properties of $Ag(Nb_xTa_{1-x})O_3$ ceramics as a function of composition at $M_2$-$M_3$ phase transition temperatures.[44]

Processing of $Ag(Ta_xNb_{1-x})O_3$ ceramics involves sintering of precursor oxide powders at temperatures above 1100 °C.[27, 45] At these temperatures, silver deficient secondary phases form due to silver volatilization.[45] This is a significant problem, especially for $AgTaO_3$ ceramics requiring sintering temperatures of ~1200 °C, and makes homogeneous sample preparation even more difficult.[26] When silver deficient secondary phases form, lower dielectric constants and higher losses were seen.[28]

If such a silver deficiency occurs during processing of the films, there would be negatively charged silver vacancies on the $Ag^+$ sites ($V_{Ag}^{'}$). These negatively charged silver vacancies then could be compensated either ionically by creation of positively charged oxygen vacancies ($V_O^{\cdot\cdot}$) or electronically by creation of positively charged holes ($h^{\cdot}$) to preserve charge neutrality.[38] Equations **1.9** and **1.10** show the corresponding defect chemistry reactions for ionic and electronic compensation of the silver vacancies.[38]

$$2V_{Ag}^{'} + V_{O}^{\cdot\cdot} \leftrightarrow Null \qquad \text{(Equation 1.9)}$$

$$V_{Ag}^{'} + h^{\cdot} \leftrightarrow Null \qquad \text{(Equation 1.10)}$$

Although many binary compounds of $Ag_x(Ta_yNb_{1-y})O_z$ and a ternary compound have been reported for the $2Ag/Ag_2O$-$Nb_2O_5$–$Ta_2O_5$ system, a ternary phase diagram is not established yet. Figure **1.15** shows a ternary phase map based on the reported binary and ternary compounds for the system.[26, 35, 46, 47] A more complete ternary phase diagram especially around perovskite compositions is necessary to optimize processing conditions and the dielectric properties.

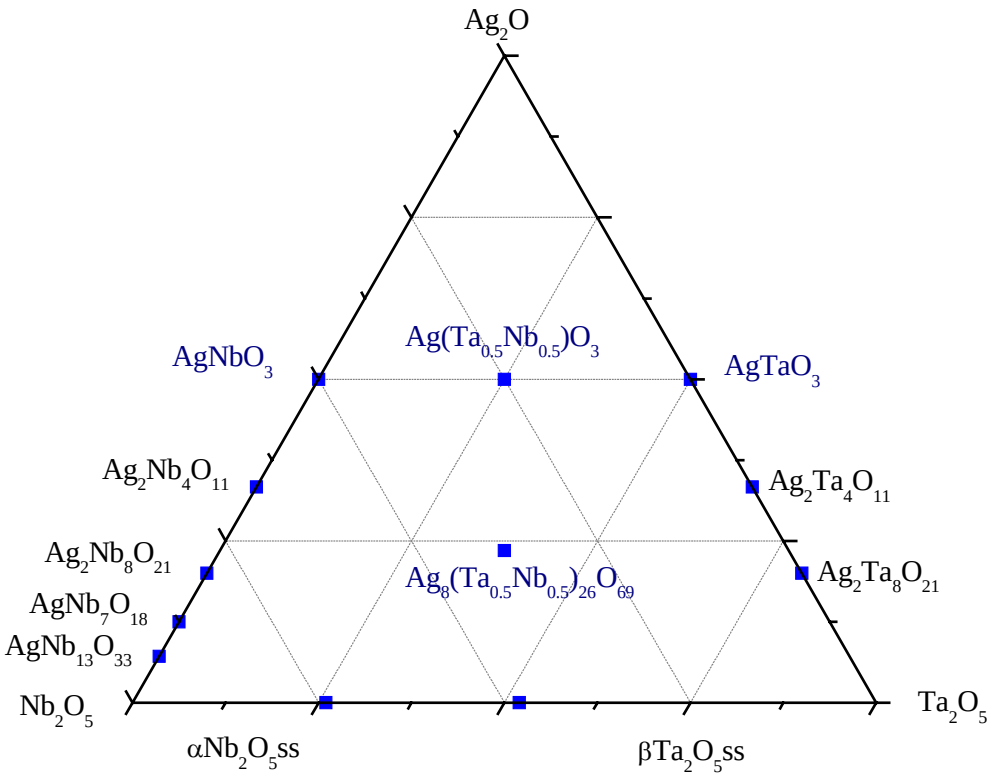


Figure **1.15**: Phase map for $Ag_2O$-$Nb_2O_5$–$Ta_2O_5$ system showing reported binary and ternary compounds.[45-47]

Silver tantalate niobate thin films with a targeted composition of $Ag(Ta_{0.4}Nb_{0.6})O_3$ have been grown by pulsed laser deposition (PLD) earlier. The grown films were silver deficient, with a composition of $Ag_{0.9}(Ta_{0.42}Nb_{0.58})O_{3-\delta}$, as determined by Rutherford Back Scattering.[48] A secondary phase, $Ag_2Nb_4O_{11}$ (ICDD 21-1086), was observed for the films that were deposited on $Pt_{0.8}Ir_{0.2}$ substrates at crystallization temperatures above 550 °C (Figure **1.16**).[49] The measured dielectric constant of ~225 at 1 MHz for a (00*l*) epitaxial film deposited on a (001)$LaAlO_3$ substrate was lower than the dielectric constant of ~450 observed for the $Ag(Ta_{0.4}Nb_{0.6})O_3$ ceramic.[36, 48]

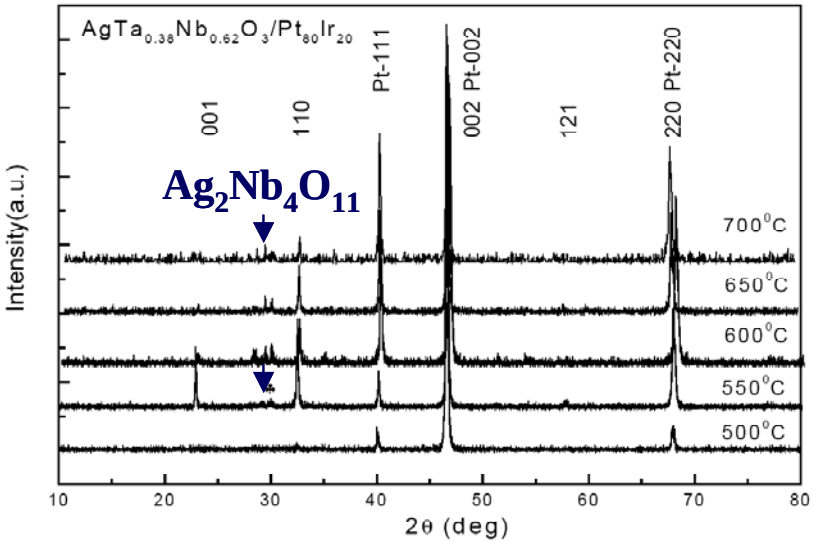


Figure **1.16**: X-Ray diffraction patterns of pulsed laser deposited $Ag_{0.9}(Ta_{0.42}Nb_{0.58})O_{3-\delta}$ films on $Pt_{0.8}Ir_{0.2}$ substrates as a function of crystallization temperature.[49] Second phase peaks are marked with arrows.

## 1.2 Objectives:

Despite the potential promise offered by ATN thin films, there are no current reports of phase pure thin films with dielectric properties comparable to the bulk material. Consequently, the goal of this work was to investigate an alternative means of synthesizing such films. Chemical solution deposition (CSD), a widely used method for deposition of ferroelectric thin films was chosen because of the potential for composition control, and composition homogeneity.[50, 51] Towards this end, it was necessary to develop a CSD route for film preparation. In order to elucidate mechanisms responsible for deviations from bulk properties, $Ag_x(Ta_yNb_{1-y})O_z$ thin films deposited on

(111)Pt/Ti/$SiO_2$/(001)Si, (001)$LaAlO_3$, (001)$SrRuO_3$/(001)$LaAlO_3$, Ag, Ag/$SiO_2$/(001)Si and Ag/Ti/$SiO_2$/(001)Si substrates by chemical solution deposition were investigated using structural and dielectric probes. In addition, thin films of $Ag_x(Ta_{0.5}Nb_{0.5})O_z$ that were silver deficient compared to the perovskite were investigated to further explore the crystal structures observed for $Ag(Ta_{0.5}Nb_{0.5})O_3$ thin films deposited on (111)Pt/Ti/$SiO_2$/(001)Si substrates. The crystal structure development results from these films might be helpful in developing the ternary phase diagram. Processing of the chemical solution deposited films requires lower crystallization temperatures (~550 °C) than bulk ceramics (>1100 °C). Therefore, it might be possible to investigate many other $Ag_x(Ta_yNb_{1-y})O_z$ compositions that are difficult to prepare in the bulk due to silver volatilization at high temperatures.

## 1.3 References:

[1] D. J. Taylor and M. H. Francombe, *Handbook of Thin Film Devices*, Academic Press, 2000.

[2] A. K. Tagantsev, V. O. Sherman, K. F. Astafiev, J. Venkatesh and N. Setter, "Ferroelectric materials for microwave tunable applications," *Journal of Electroceramics*, **11** 5-66 (2003).

[3] D. Dimos and C. H. Mueller, "Perovskite thin films for high frequency capacitor applications," *Annual Review of Materials Science*, **28** 397-419 (1998).

[4] I. Vendik, O. Vendik, V. Pleskachev, A. Svishchev and R. Woerdenweber, "Design of tunable ferroelectric filters with a constant fractional band width," *IEEE MTT-S Digest*, **3** 1461 (2001).

[5] S. S. Gevorgian, E. L. Kollberg, "Do we really need ferroelectrics in paraelectric phase only in electrically controlled microwave devices?," *IEEE Transactions on Microwave Theory and Techniques*, **49** [11] 2117-2124 (2001).

[6] V. Bovtun, J. Petzelt, V. Porokhonskyy, S. Kamba and Y. Yakimenko, "Structure of the dielectric spectrum of relaxor ferroelectrics," *Journal of the European Ceramic Society*, **21** 1307-1311 (2001).

[7] C. A. Randall, *A Transmission Electron Microscope Study of Normal and Relaxor Perovskite Ferroelectric Materials*, Ph. D. Thesis in Experimental Physics, University of Essex, Colchester, U.K., 1987.

[8] A. Feteira, D. C. Sinclair, I. M. Reaney, Y. Somiya and M. T. Lanagan, "$BaTiO_3$ based ceramics for tunable microwave applications," *Journal of the American Ceramic Society*, **87** [6] 1082-1087 (2004).

[9] J. W. Liou and B. S. Chiou, "Effect of direct-current biasing on the dielectric properties of barium strontium titanate," *Journal of the American Ceramic Society*, **80** [12] 3093-3099 (1997).

[10] A. Erikson, A. Deleniv and S. Gevorgian, "Orientation and direct current field dependent dielectric properties of bulk single crystal $SrTiO_3$ at microwave frequencies," *Journal of Applied Physics*, **93** [5] 2848- 2854 (2003).

[11] Z. Jiwei, Y. Xi, C. Xiaogang, Z. Liangying and H. Chen "Dielectric properties under dc-bias field of $Ba_{0.6}Sr_{0.4}TiO_3$ with various grain sizes," *Materials Science and Engineering B: Solid-state Materials for Advanced Technology*, **94** 164-169 (2002).

[12] X. Wei and X. Yao, "Nonlinear dielectric properties of barium strontium titanate ceramics," *Materials Science and Engineering B: Solid-state Materials for Advanced Technology*, **99** 74-78 (2003).

[13] X. G. Tang, K. H. Chew and H. L. W. Chan, "Diffuse phase transition and dielectric tunability of $Ba(Zr_yTi_{1-y})O_3$ Nonlinear dielectric properties of barium strontium titanate ceramics," *Materials Science and Engineering B: Solid-state Materials for Advanced Technology*, **99** 74-78 (2003).

[14] T. Wang, X. M. Chen and X. H. Zheng, "Dielectric characteristics and tunability of barium stannate titanate ceramics," *Journal of Electroceramics*, **11** 173-178 (2003).

[15] C. Ang, A. S. Bhalla, R. Guo and L. E. Cross, "Effect of dc bias on dielectric properties of $Cd_2Nb_2O_7$ ceramics," *Journal of Applied Physics*, **90** [5] 2465-2468 (2001).

[16] T. M. Shaw, S.Trolier-McKinstry and P. C. McIntyre, "The properties of ferroelectric films at small dimensions," *Annual Review of Materials Science*, **30** 263-298 (2000).

[17] N. A. Pertsev, A. G. Zembilgotov, S. Hoffman, R. Waser and A. K. Tagantsev, "Ferroelectric thin films grown on tensile substrates: renormalization of the Curie-Weiss law and apparent absence of ferroelectricity," *Journal of Applied Physics*, **85** [3] 1698-1701 (1999).

[18] A. Tombak, J. P. Maria, F. Ayguavives, Z. Jin, G. T. Stauf, A. I. Kingon and A. Mortazawi, "Tunable barium strontium titanate thin film capacitors for RF and microwave applications," *IEEE Microwave and Wireless Component Letters*, **12** [1] 3-5 (2002).

[19] C. Basceri, S. K. Streiffer, A. I. Kingon and R. Waser, "The dielectric response as a function of temperature and film thickness of fiber-textured (Ba,Sr)$TiO_3$ thin films grown by chemical vapor deposition," *Journal of Applied Physics*, **85** [5] 2497-2504 (1997).

[20] C. B. Parker, J. P. Maria, "Temperature and thickness dependence of (Ba,Sr)$TiO_3$ thin films," *Applied Physics Letters*, **81** [2] 340-342 (2002).

[21] R. L. Thayer, C. A. Randall and S. Trolier-McKinstry, "Medium permittivity bismuth zinc niobate thin film capacitors," *Journal of Applied Physics*, **94** [3] 1940-1947 (2003).

[22] J. Lu and S. Stemmer, "Low loss tunable bismuth zinc niobate films deposited by rf magnetron sputtering," *Applied Physics Letters*, **83** [12] 2411-2414 (2003).

[23] J. C. Nino, M. T. Lanagan and C. A. Randall, "Dielectric relaxation in $Bi_2O_3$–ZnO-$Nb_2O_5$ cubic pyrochlore," *Journal of Applied Physics*, **89** [8] 4512-4516 (2001).

[24] J. Petzelt and S. Kamba, "Submillimetre and infrared response of microwave materials: extrapolation to microwave properties," *Materials Chemistry and Physics*, **79** 175–180 (2003).

[25] A. A. Volkov, B. P. Gorshunov, G. Komandin, W. Fortin, G. E. Kugel, A. Kania and J. Grigas, "High frequency dielectric spectra of $AgTaO_3$-$AgNbO_3$ mixed ceramics," *Journal of Physics Condensed Materials*, **7** 785-793 (1995).

[26] A. Kania, "$AgTa_xNb_{1-x}O_3$ solid solutions: dielectric properties and phase transitions," *Phase Transitions*, **3** 131-139 (1983).

[27] J. Petzelt, S. Kamba, E. Buixaderas, V. Bovtun, Z. Zikmund, A. Kania, V. Koukal, J. Pokorny, J. Polivka, V. Pashkov, G. Komandin and A. Volkov, "Infrared and microwave

dielectric response of the disordered antiferroelectric $Ag(Ta,Nb)O_3$ system," F*erroelectrics*, **223** 235-246 (1999).

[28] M. Valant and D. Suvorov, "New high permittivity $AgNb_{1-x}Ta_xO_3$ microwave ceramics: part 2, dielectric characteristics," *Journal of the American Ceramic Society*, **82** [11] 88-93 (1999).

[29] F. Zimmermann, W. Menesklou, E. Ivers-Tiffee, "Investigation of $Ag(Ta,Nb)O_3$ as tunable microwave dielectric," *Journal of the European Ceramic Society*, **24** 1811-1814 (2004).

[30] M. Pawelczyk, "Phase transitions in $AgTa_xNb_{1-x}O_3$ solid solutions," *Phase Transitions*, **8** 273-292 (1987).

[31] P. Sciau, A. Kania, B. Dkhil, E. Suard and A. Ratuszna, "Structural investigation of $AgNbO_3$ phases using x-ray and neutron diffraction," *Journal of Physics Condensed Matter*, **16** 2795-2810 (2004).

[32] Powder diffraction file ICDD 89-7738, International Center for Diffraction Data, Newtown Square, PA, USA.

[33] Powder diffraction file ICDD 22-0471, International Center for Diffraction Data, Newtown Square, PA, USA.

[34] A. Kania and K. Roleder, "Ferroelectricity in $Ag(Nb_{1-x}Ta_x)O_3$ solid solutions," *Ferroelectric Letters*, **2** 51-54 (1984).

[35] A. Kania, "Dielectric properties of $Ag_{1-x}A_xNbO_3$ (A:K, Na and Li) and $AgNb_{1-x}Ta_xO_3$ solid solutions in the vicinity of diffuse phase transitions," *Journal of Physics D-Applied Physics*, **34** [10] 1447-1455 (2001).

[36] M. Hafid, G. E. Kugel, A. Kania, K. Roleder and M. D. Fontana, "Study of the phase transition sequence of mixed silver tantalate niobate $Ag(Nb_{1-x}Ta_x)O_3$ by inelastic light scattering," *Journal of Physics Condensed Matter*, **4** [9] 2333-2345 (1992).

[37] A. Chelkowski, *Dielectric Physics*, Elsevier Scientific Publishing, 1980.

[38] W. D. Kingery, H. K. Bowen and D. R. Uhlmann, *Introduction to Ceramics, 2nd Edition*, Wiley-Interscience Publishing, 1976.

[39] R. Waser, *Nanoelectronics and Information Technology*, Wiley Publishing, 2003.

[40] A. J. Moulson and J. M. Herbert, *Electroceramics: Materials, Properties and Applications*, Chapman and Hall Publishing, 1990.

[41] A. G. Cockbain and P. J. Harrop, "The temperature coefficient of capacitance," *British Journal of Applied Physics,* **1** [9] 1109-1115 (1968).

[42] E. L. Colla, I. M. Reaney and N. Setter, "Effect of structural changes in complex perovskites on the temperature coefficient of the relative permittivity," *Journal of Applied Physics*, **74** [5] 3414-3425 (1993).

[43] R. Waser, U. Bottger and S. Teidke, *Polar Oxides: Properties, Characterization and Imaging*, Wiley Publishing, 2005.

[44] G. E. Kugel, W. Fortin, J. Grigas and A. Kania, "Manifestation of Nb dynamics in raman, microwave and infrared spectra of the $AgTaO_3$-$AgNbO_3$ mixed system," *Journal of Applied Physics*, **79** [8] 4273-4282 (1996).

[45] M. Valant, D. Suvorov and A. Meden, "New high permittivity $AgNb_{1-x}Ta_xO_3$ microwave ceramics: part 1, crystal structures and phase decomposition relations," *Journal of American Ceramic Society*, **82** [11] 81-87 (1999).

[46] Powder Diffraction Files: 89-7738, 51-0374, 21-1344, 21-1345, 22-473, 21-1083, 21-1084, 21-1085, 21-1086, 22-471. International Center for Diffraction Data, Newtown Square, PA, USA.

[47] E. M. Levin, H. F. McMurdie and M. K. Reser, *Phase Diagrams for Ceramists 1975 Supplement*, The American Ceramic Society, Columbus, OH, 1975.

[48]J. H. Koh and A. Grishin, "$Ag(Ta,Nb)O_3$ Thin film low-loss variable interdigital capacitors," *Applied Physics Letters*, **79** [14] 2234-2236 (2001).

[49] J. H. Koh, S. I. Khartsev, A. Grishin and V. Petrovsky, "Crystalline and electrical properties of ferroelectric silver niobate tantalate thin films," *Material Research Society Proceedings* **655**, CC11.5.1, (2001).

[50] J. D. Mackenze and Y. Xu, "Ferroelectric materials by the sol-gel method," *Journal of Sol-Gel Science and Technology*, **8** 673-679 (1997).

[51] H. Schmidt, "Chemistry of material preparation by the sol-gel process," *Journal of Non-Crystalline Solids*, **100** 51-64 (1988).

# Chapter 2

## Experimental Procedure

### 2.1 Chemical Solution Deposition of $Ag_x(Ta_yNb_{1-y})O_z$ Thin Films:

$Ag_x(Ta_yNb_{1-y})O_z$ thin films were deposited by spinning of the chemical solutions on the substrates with subsequent heat treatment. Prior to deposition, the substrates were heat treated at temperatures 110 °C or higher (depending on the type of the substrates) to remove adsorbed water to promote wetting by the chemical solutions. The chemical solutions were dispensed onto the substrate using a 10 cc syringe (BD Injection Systems, Franklin Lakes, NJ) filtered through a 0.1 μm PTFE membrane (Whatman Inc., Clifton, NJ) (Figure 2.1). When the surface was fully covered with the chemical solution, the substrate was spun using a PWM32 model spinner (Headway Research Inc., Garland, TX) with a rate of either 1500 or 4000 rpm for 30 seconds. The spun layer was heat treated by hot plate baking in air and crystallized either using a quartz tube furnace or a rapid thermal anneal furnace (RTP600S model) in an $O_2$ ambient.

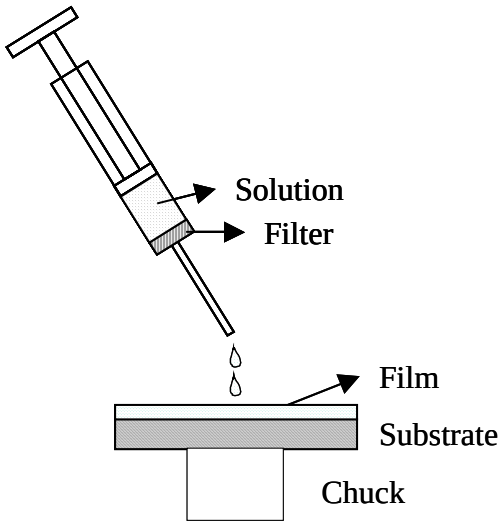


Figure **2.1**: Schematic showing dispensation of silver tantalate niobate solution onto a substrate.

## 2.2 Substrate Surface Preparation:

The commercial and in-house prepared substrates were used for the deposition of $Ag_x(Ta_yNb_{1-y})O_z$ thin films: (111)Pt/Ti/$SiO_2$/(100)Si (Ramtron International Corp., Colorado Springs, CO and NOVA Crystal Inc.-Gemfire Corp., Fremont, CA), $SiO_2$/(100)Si (NOVA Crystal Inc.-Gemfire Corp., Fremont, CA) and (001)$LaAlO_3$ (MTI Corporation, Richmond, CA) $SrRuO_3$/(001)$LaAlO_3$, Ag (0.25 mm thick, Alfa-Aesar Company, Ward Hill, MA), Ag sputtered $SiO_2$/(001)Si (Silicon Quest Int., Santa Clara, CA) and Ag/Ti sputtered $SiO_2$/(001)Si (Silicon Quest Int., Santa Clara, CA). The $SrRuO_3$ layer (~150 nm thick) was pulsed laser deposited on (001)$LaAlO_3$ substrates at 680 °C and a 160 mTorr chamber pressure (10% $O_3$/90% $O_2$) with a Lambda Physik EMG 150

KrF excimer laser.[1] Sputtering of ~100 nm thick Ag and ~20 nm thick Ti layers on $SiO_2$/(100)Si substrates was done using a Lesker CMS-18 model sputtering tool with a chamber pressure of 5 mTorr (Argon) at room temperature. The substrate was placed 20 cm away from the targets and rotated at 10 rpm while both of the layers were RF sputtered at a gun setting of 200 Watts for 110 seconds for Ti and 600 seconds for Ag.

Some of the substrates were exposed to different cleaning and annealing treatments prior to the chemical solution deposition. (111)Pt/Ti/$SiO_2$/(100)Si (Pt/Si), $SiO_2$/(001)Si (Si) and Ag substrates were rinsed with isopropyl alcohol (IPA) (Sigma-Aldrich Chemical Company, Milwaukee, WI) and blown dry using $N_2$. Following surface cleaning, Pt/Si and Si substrates were annealed at 700 °C for a minute in air using a rapid thermal anneal furnace (RTA). The Ag substrate was baked on a hot plate at 450 °C for one minute to remove organic or water contaminants. This likely introduced $Ag_2O$ at the substrate surface during cooling down to room temperature as shown in phase diagram of the silver-oxygen system (Figure **2.2**). Prior to sputtering Ag or Ag/Ti layers, the Si substrates were also cleaned in the same manner used for Pt/Si substrates. No IPA rinse was used with the pulsed laser deposited (001)$SrRuO_3$/(001)$LaAlO_3$ (SRO/LAO) or Ag and Ag/Ti sputtered Si substrates prior to the annealing, since they were cleaned prior to electrode deposition. The moisture-removal annealing procedure for the SRO/LAO substrates was the same as for Pt/Si substrates (700 °C for a minute in air by RTA). However, the annealing for the Ag/Ti coated Si substrates was lowered to 110 °C for 5 seconds to minimize hillocking.

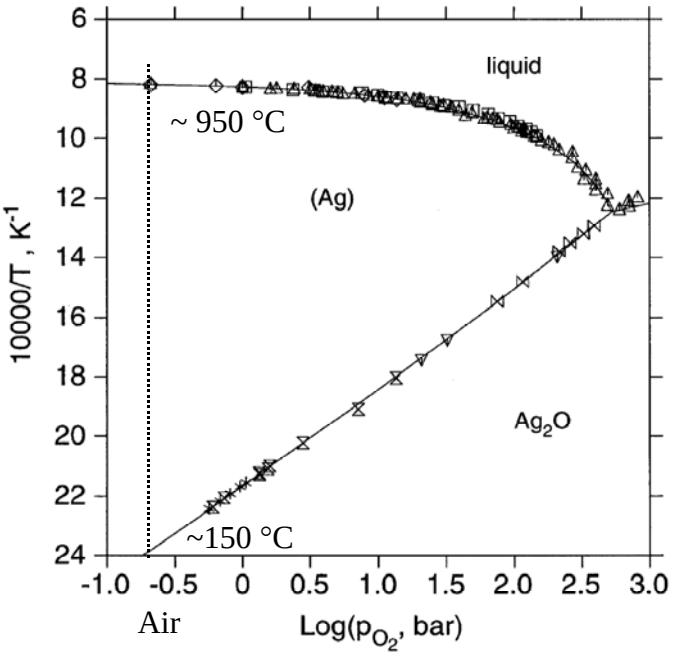


Figure **2.2**: Phase diagram for silver-oxygen system. Dashed line corresponds to oxygen partial pressure in air.[2]

### 2.3 Structural Characterization of $Ag_x(Ta_yNb_{1-y})O_z$ Thin Films:

X-ray diffraction (XRD) and transmission electron microscopy (TEM) were used for structural characterization of the $Ag_x(Ta_yNb_{1-y})O_z$ thin films. XRD analysis included conventional 2θ scans, as well as rocking curve measurements (in θ) and φ scans to check crystal structure formation, crystallinity and the in-plane orientation of the films. TEM analysis involved bright and dark field imaging to investigate the morphology of the films and the existence of interfacial reactions between the substrate and films. Selected area electron diffraction was also used for identification of the observed phases

and energy dispersive x-ray spectroscopy for compositional investigation of secondary phases.

Diffraction of X-Rays from crystalline phases having interplanar spacings of d is described by Bragg's Law (Equation **2.1**).[3] XRD peak positions therefore both depend on the wavelength of X-Rays used and the interplanar d-spacings of the crystalline phases. For XRD investigations, a Cu target was used. In addition to XRD peaks from the $Cu_{K\alpha}$ radiation, additional peaks due to $Cu_{K\beta}$ radiation as well as $W_{L\alpha}$ and $W_{L\beta}$ radiation (due to tube contamination) were observed for some of the strongly diffracting planes.

$$n\lambda = 2dSin\theta \qquad \text{(Equation 2.1)}$$

where:

$n$ : Order of reflection

$\lambda$ : Wavelength of diffracting X-rays

$d$ : Interplanar spacing of the diffracting planes

$\theta$ : Bragg angle

θ - 2θ XRD scans were performed to check crystal structure formation using a Scintag Pad V x-ray diffractometer with a 2θ scanning rate of 2° or 4°/minute. For a θ - 2θ XRD scan, both sample and XRD detector were rotated about an axis O (Figure **2.3**) perpendicular to the plane of the drawing with rates of θ and 2θ °/minute. In this scanning setup, only X-rays diffracting from planes that were parallel to surface of the film were detected.[2]

Rocking curves (θ scans) of the 004 perovskite XRD peak were performed to check the crystallinity of the $Ag(Ta_{0.5}Nb_{0.5})O_3$ films deposited on $(001)SrRuO_3/(001)LaAlO_3$ substrates using a Scintag Pad V x-ray diffractometer. For the θ scan, the XRD detector was fixed at an angle of $2\theta_B$, the receiving slits were removed and the sample was rotated ±10 degree from $\theta_B$ (Bragg Angle) with a step size of 0.01° and step duration of 0.5 second. The full width at half maximum intensity (FWHM) of the resulting XRD peaks were reported. Films having better crystallinity had lower FWHM values due to having less mosaicity.

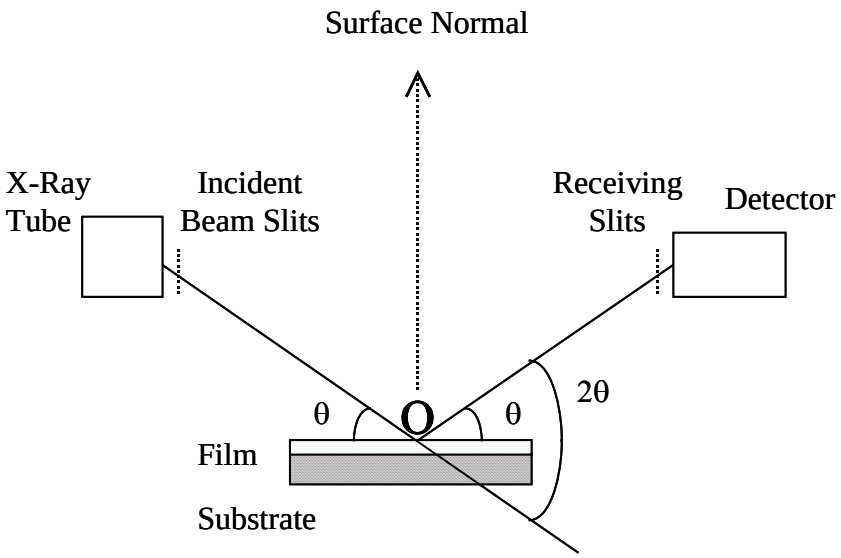


Figure **2.3**: Schematic explaining sample and diffractometer layout for θ - 2θ XRD scans. Both sample and XRD detector were rotated about an axis O perpendicular to the plane of the drawing with rates of θ and 2θ °/minute for a θ - 2θ XRD scans.

φ XRD scans of the off-axis 321 and 231 planes were performed using a Picker 4-circle x-ray diffractometer to check for the existence of in-plane orientation in the $Ag(Ta_yNb_{1-y})O_3$ films that were deposited on $(001)SrRuO_3/(001)LaAlO_3$ substrates. In order to detect the 321 and 231 pseudocubic perovskite peaks, the sample was tilted off axis from a χ position of 90.0° to a χ position of 15.23° (Figure **2.4** shows the definition of the diffractometer axes). The detector position was fixed at the $2\theta_B$ position, and the sample was rotated with a step size of 0.5° and a count time of 5 sec/step for a φ scan.[4]

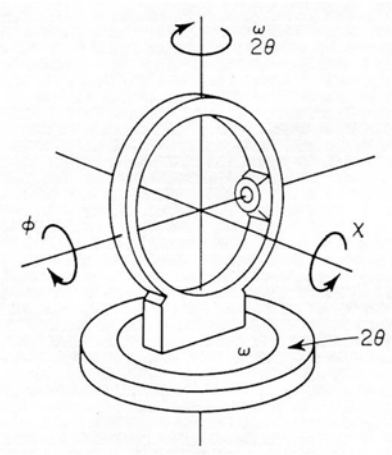


Figure **2.4**: Schematic showing definition of 4 circle diffractometer axes.[5]

TEM investigation of the films was performed using three different instruments: a Philips 420 TEM (120 kV), a Jeol 2010 $LaB_6$ TEM (200 kV) and a Jeol 2010F (200 kV) field emission TEM with an energy dispersive x-ray spectroscopy detector (EDAX Si(Li) model detector with super ultra thin window). Bright and dark field imaging of transverse

and plan-view samples were used for checking interfacial reactions between the substrate and the film, the morphology of the films and secondary phase formation in the films. In bright field imaging, the bright central spot made up of directly transmitted electrons are used for imaging.[6] In the case of dark field imaging, one of the diffracted beams is used for imaging instead of the bright central spot.[6] Electron diffraction was used for identifying phases and energy dispersive x-ray spectroscopy was used for checking the chemical composition of secondary phases.

Two different techniques were used to prepare transverse and plan view samples.[7,8] In order to prepare transverse samples, two pieces of the film were fractured and glued face to face using quick setting epoxy resin. The sandwich structure was mounted onto a Gatan disc grinder using Crystalbond resin, then was ground and polished using 600 grit silicon carbide paper till its thickness was reduced to around ~20 μm. The sample was removed from the grinder, epoxy glued on a copper ring and thinned to electron transparency using a Fischione (model 3000) ion miller. In order to prepare plan view samples, a piece of film was ground and polished from the silicon side, epoxy glued on a copper ring and ion milled from the silicon side to electron transparency.

Electron diffraction patterns (EDP) were used to identify the crystal structures observed for some of the films. EDP can be explained by the use of reciprocal lattices and the Ewald sphere. In a reciprocal lattice, sets of parallel (*hkl*) atomic planes are represented by a single point located a distance $1/d_{hkl}$ from the lattice origin.[6] Figure **2.5** shows the simulated reciprocal lattice of perovskite $Ag(Ta_{0.5}Nb_{0.5})O_3$ with the monoclinic unit cell reported in ICDD 89-7738 (created using CaRine Crystallography software).[9]

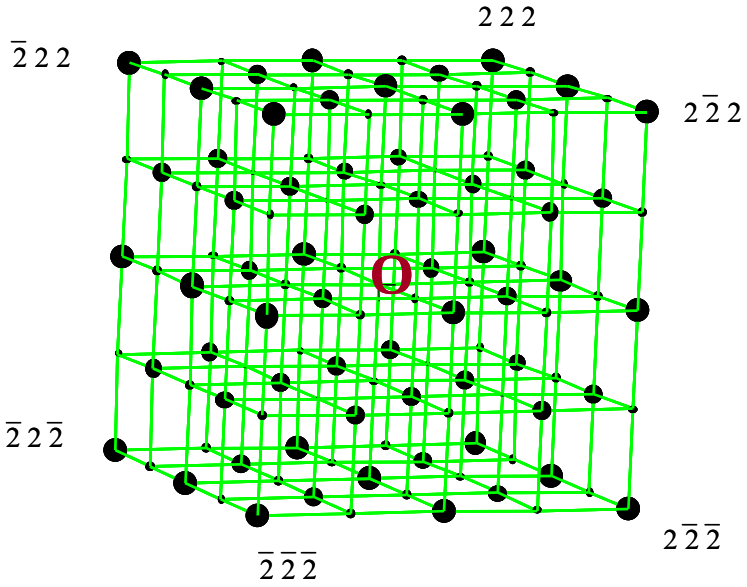


Figure **2.5**: Simulated reciprocal lattice of $Ag(Ta_{0.5}Nb_{0.5})O_3$ having the monoclinically distorted perovskite crystal structure reported in ICDD 89-7738. Only the indices of 222 family planes are shown for clarity.

The Ewald sphere is used for finding the strongly diffracting planes based on an incident electron beam vector, $k_I$, and the known energy of the electrons used for diffraction.[6] An Ewald sphere having a radius $1/\lambda$ (where $\lambda$ is the wavelength of the electrons and depends on the energy of the electrons used, which is in turn determined by the TEM's kV setting) is placed on a position (C) in the reciprocal lattice that is defined by the incident electron beam vector $k_I$ (vector CO where O is the origin in Figure **2.6**).[6] When the surface of the Ewald sphere intersects any point in the reciprocal lattice, the set of planes corresponding to that point satisfies Bragg's Law and these planes diffract strongly.[6]

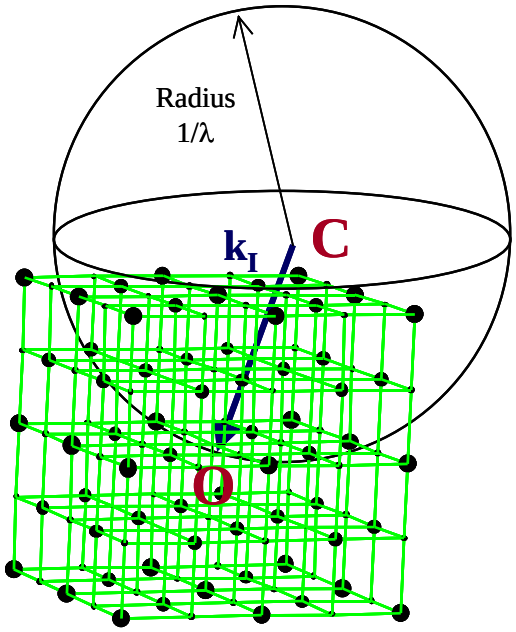


Figure 2.6: Schematic representing the Ewald sphere and the reciprocal lattice of $Ag(Ta_{0.5}Nb_{0.5})O_3$ (ICDD 89-7733). The reciprocal lattice points intersecting the Ewald sphere surface diffracts strongly. The radius of the Ewald sphere is not to scale in the sketch; the real radius is much bigger than shown, so that the surface is almost planar for electrons accelerated either at 120 and 200 kV.

The zone axis electron diffraction patterns are characteristic of the crystal system and were used for identification of the crystal structures observed for some of the films.[6] A zone axis [UVW] is a direction that is common to all the planes of the zone.[6] For a [UVZ] zone axis electron diffraction pattern, all of the (*hkl*) planes of the zone axis have to satisfy the Weiss zone law, $hU+kV+lZ=0$. Figure 2.7 shows a simulated [001] diffraction pattern of $Ag(Ta_{0.5}Nb_{0.5})O_3$ (ICDD 89-7738) using CaRine Crystallography software.

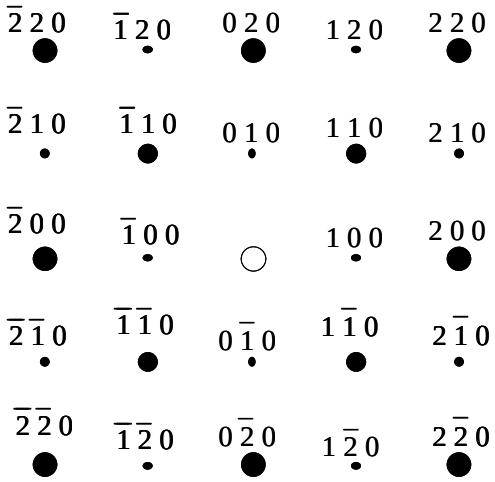


Figure 2.7: Simulated [001] zone axis electron diffraction pattern of $Ag(Ta_{0.5}Nb_{0.5})O_3$ (ICDD 89-7738). Only planes having indices between $2\,2\,0$ and $\bar{2}\,\bar{2}\,0$ are shown. Note that the reflective intensities of the planes having indices with (h+k+l)=2n is stronger than the reflective intensities of the planes having indices with (h+k+l)=2n+1, which is typical of the perovskite structure.

## 2.4 Electrical Property Characterization of $Ag_x(Ta_yNb_{1-y})O_z$ Thin Films:

Electrical property characterization of $Ag_x(Ta_yNb_{1-y})O_z$ films was performed by preparing parallel plate capacitor structures. The platinum top electrodes were sputtered through shadow masks or prepared by a bilayer photoresist lift off technique. The type of bottom electrode depended on the substrate used for the deposition. Prior to sputtering the top Pt electrodes, the substrates and a stainless steel shadow mask (having hole diameters from 300 to 120 μm) were rinsed with IPA, blown by $N_2$ and dried at 110 °C for 30 seconds by hot plate baking in air. The clean shadow masks were attached to the film surface using small pieces of Kapton Tape (DuPont Chemical Company, Circleville,

OH). Pt top electrodes ~150 nm thick were sputtered using a Baltec SCD 50 model sputter coater with a 0.05 mbar chamber pressure (Argon) at room temperature. The samples was placed 5 cm away from the target and Pt was DC sputtered for 180 seconds at 63 mA sputtering current onto the films through the shadow mask.

For silver deficient $Ag_x(Ta_yNb_{1-y})O_z$ compositions, smaller Pt electrodes (50 μm squares) were prepared by a bilayer photoresist lift off technique. The substrates were rinsed with IPA, blown by $N_2$ and hot plate baked at 180 °C for 40 seconds before depositing the photoresists. A LOR 5A (Microchem Chemical Company, Newton, MA) lift-off resist was spun onto the substrate at 4000 rpm for 40 seconds and hot plate baked at 180 °C for 2 minutes. Over this resist layer, a SPR 3012 (Shipley L.L.C.-Rohm and Haas Electronic Materials, Marlborough, MA) positive photoresist was spun at 4000 rpm for 30 seconds and hot plate baked at 95 °C for 1 minute. In order to pattern 50 μm squares, the photoresist bilayer was exposed to ultraviolet light through a photomask using a Suss MJB3 photomask aligner (Suss Microtech Inc. VT). The exposed bilayer was developed using CD-26 developer (Shipley L.L.C.-Rohm and Haas Electronic Materials, Marlborough, MA). The (~150 nm thick) top platinum electrode was sputtered onto the patterned photoresist bilayer using a Lesker CMS-18 model sputtering tool with a chamber pressure of 5 mTorr (Argon) at room temperature. The samples were placed 20 cm away from target and rotated at 10 rpm while Pt was DC sputtered at a gun setting of 200 Watts for 600 seconds. The sputtered Pt on top of the remaining bilayer resist was lifted off by rinsing the sample in acetone until only the patterned Pt remained on the film. The substrate was rinsed with IPA and deionized water and dried at 60 °C. In order

to decrease the high losses seen with as-sputtered Pt electrodes, all of the samples were annealed at 500 °C for 30 minutes in $O_2$ ambient in a quartz tube furnace.

In order to access the bottom electrodes, the dielectric film was locally removed. Although it was possible to acid etch silver deficient $Ag_x(Ta_yNb_{1-y})O_z$ compositions using HF (48 weight %, Sigma-Aldrich Chemical Company, Milwaukee, WI), it was not possible to acid etch films having the $Ag(Ta_{0.5}Nb_{0.5})O_3$ composition and the perovskite crystal structure. Instead, these films were scratched using a diamond scribe. Pt sputtered onto the scratched region was used to contact the bottom electrode.

Measurements of the film thickness and top electrode areas were needed for the dielectric constant calculations. Acid etching of silver deficient compositions permitted preparation of a step and measurement of film thickness using an alpha step profiler (model 500). In order to prepare the step, the substrate was cleaned by rinsing with IPA, blown by $N_2$ and dried at 60 °C. The film was partially painted with Shipley 1811 photoresist (Shipley L.L.C.-Rohm and Haas Electronic Materials, Marlborough, MA) and hot plate baked at 60 °C. The uncovered region was acid etched by swabbing with cotton tips dipped in HF (48 weight %). After the film was completely removed in one area, the Pt surface was cleaned using cotton tips dipped in HCl (38 weight %, J. T. Baker, Phillipsburg, NJ) and rinsed with deionized water. The photoresist layer was removed with acetone and the substrate was cleaned by rinsing with IPA and deionized water and dried at 60 °C. The thickness of the perovskite $Ag(Ta_yNb_{1-y})O_3$ films was determined from cross sectioned samples using a field emission scanning electron microscope (Jeol

model 6700F). All of the top electrode areas were measured using light microscope images having calibrated scale marks.

The dielectric properties were measured within the frequency range of 1 Hz to 100 kHz. The low frequency measurements < 1 kHz were performed using an HP/Agilent 3562A dynamic signal analyzer. The measurements at a higher frequency range (1 to 100 kHz) were done either using an HP/Agilent 4284A precision LCR meter or an HP/Agilent 4192A LF impedance analyzer. In all cases, an oscillation level of 30 mV was used. Polarization – electric field measurements were performed at 0.5 kHz using a Radiant Technologies RT66A standard ferroelectric tester. Temperature dependent measurements were done while heating the sample from room temperature with a rate of 3 °C/min using a probe station with a heated stage (Probing Solutions Inc. model 400 TM). The low temperature measurement was performed after the sample was wire bonded to a ceramic package (24 LD S/B type, Spectrum Semiconductor Materials, San Jose, CA) with a 25 μm thick gold wire using a Kulicke&Soffa 4123 model ultrasonic wedge wire bonder. The sample was cooled in a Delta design chamber to –190 °C with a cooling rate of 2 °C/min during data acquisition. The liquid nitrogen temperature (77 K) measurements were performed by immersing the sample in a liquid nitrogen filled plastic beaker and using the probe station.

## 2.5 References:

[1] J.P. Maria, S. Trolier-McKinstry, D. G. Schlom, M.E. Hawley and G. W. Brown, "The influence of energetic bombardment on the structure and properties of epitaxial $SrRuO_3$ thin films grown by pulsed laser deposition," *Journal of Applied Physics*, **83** [8] 4373-4379 (1998).

[2] J. Assal, B. Hallstedt and L. J. Gauckler, "Thermodynamic assessment of the silver-oxygen system," *Journal of American Ceramic Society*, **80** [12] 3054-3060 (1997).

[3] B. D. Cullity, *Elements of X-Ray Diffraction, 2nd Edition*, Addison-Wesley Publishing Inc., 1978.

[4] J. P. Maria, *Epitaxial $Pb(Mg_{1/3}Nb_{2/3})O_3$–$PbTiO_3$ Thin Films*, Ph. D. Thesis, The Pennsylvania State University, 1998.

[5] www.scintag.com

[6] D. B. Williams and C. B. Carter, *Transmission Electron Microscopy*, Plenum Press, 1996.

[7] I. M. Reaney, K. Brooks, R. Klissurska, C. Pawlaczyk and N. Setter, "Use of transmission electron microscopy for the characterization of rapid thermally annealed solgel lead-zirconate-titanate films," *Journal of American Ceramic Society*, **77** [5] 1209-1216 (1994).

[8] Z. Zhou, I. M. Reaney, D. Hind, S. J. Milne, A. P. Brown and R. Brydson, "Microstructural evolution during pyrolysis of triol based sol-gel single layer $Pb(Zr_{0.53}Ti_{0.47})O_3$ thin films," *Journal of Materials Research*, **17** [8] 2066-2074 (2002).

[9] http://pro.wanadoo.fr/carine.crystallography/

# Chapter 3

## Chemical Solution Synthesis of $Ag_x(Ta_yNb_{1-y})O_z$

### 3.1 Introduction:

The first research objective was synthesis of a chemical solution for the silver tantalate niobate system, $Ag_x(Ta_yNb_{1-y})O_z$. This route was chosen as it should enable films with a variety of well-controlled stoichiometries to be realized. There was no chemical solution synthesis route for the silver tantalum niobate system reported in the literature. Therefore, the first step in the work was to develop one.

Synthesizing a new solution involves selection of precursors and solvents, controlling the reactions between precursors and solvents, and slowing down any fast reactions leading to precipitation. When a solution precipitates, it loses its physical and chemical homogeneity and therefore cannot be used for the deposition.

The precursors and solvents determine the reactions that need to be controlled to prevent precipitation during synthesis of a chemical solution. Metal alkoxides, $M(OR)_n$, (where M stands for metal and R stands for alkyl ($C_nH_{2n+1}$)) are the most commonly used precursors to prepare chemical solutions.[1, 2] In the presence of water, hydrolysis, condensation and alcohol exchange are the main reactions between metal alkoxides and alcohols.[3]

In hydrolysis reactions, the metal alkoxide ($M(OR)_n$) reacts with water and exchanges one of its alkoxy (OR) groups with an hydroxyl (OH) group and produces an hydroxo-metal alkoxide ($M(OR)_{n-1}OH$) and an alcohol (ROH). Equation **3.1** shows the hydrolysis reactions that can continue until the metal alkoxide exchanges all of its alkoxy groups and a metal hydroxide, $M(OH)_n$, is formed.[3]

$$M(OR)_n + H_2O \rightarrow M(OR)_{n-1}(OH) + ROH$$

$$M(OR)_{n-1}(OH) + H_2O \rightarrow M(OR)_{n-2}(OH)_2 + ROH$$

. . . . (Equation **3.1**)

. . . .

$$M(OR)(OH)_{n-1} + H_2O \rightarrow M(OR)_n + ROH$$

Hydroxo-metal alkoxides produced in hydrolysis reactions are very reactive and act as monomers in condensation reactions or polymerization reactions.[3] Condensation reactions start with a reaction of two monomers of hydroxo-metal alkoxides to form a dimer and an alcohol (Equation **3.2**). The resulting dimers and monomers further react to form longer chains, and polymerization continues with the reactions of longer chains with monomers, dimers and other chains.[3]

$$2\ M(OR)_{n-1}(OH) \rightarrow (OR)_{n-1}M\text{-}O\text{-}M(OR)_{n-2}(OH) + ROH \quad \text{(Equation 3.2)}$$

In alcohol exchange reactions, a metal alkoxide ($M(OR)_n$) reacts with the dissolved parent alcohol (R'OH) and exchange its alkyl group (R) with a dissolved alcohols' alkyl group (R').[4] Equation **3.3** is a set of the alcohol exchange reactions that can continue until all alkyl groups have exchanged with the dissolved alcohols alkyl groups.

$$M(OR)_n + R'OH \rightarrow M(OR)_{n-1}(OR') + ROH$$

$$M(OR)_{n-1}(OR') + R'OH \rightarrow M(OR)_{n-2}(OR')_2 + ROH$$

. . . . (Equation **3.3**)

. . . .

$$M(OR)(OR')_{n-1} + R'OH \rightarrow M(OR')_n + ROH$$

All these reactions can occur to different extents and can produce many different species during solution synthesis. Although it is difficult to decide exactly which condensation reaction causes precipitation, it is possible to slow down the condensation reactions by minimizing hydrolysis reactions. This is true because the condensation reactions start and continue with the reactive hydroxo-metal alkoxides that were produced in hydrolysis reactions.[4]

Minimizing hydrolysis reactions requires minimizing the presence of water in solvents and precursors and chemically modifying the metal alkoxides to make them more stable against hydrolysis reactions.[5] The first point demands use of dry precursors and solvents and minimization of adsorbed water from atmosphere. Therefore, the chemical solution needs to be synthesized under dry atmospheric conditions using dry

precursors and solvents. For this reason, all solution synthesis done in this work was performed under a dry argon ambient.

Chemical modification of metal alkoxides to make them more stable against hydrolysis reactions is based on removal of easily hydrolysable, weakly bonded alkyl (R) groups with more strongly bonded groups.[6] Reacting metal alkoxides with organic acids (RCOOH) or with an alcohol having longer alkyl (R') groups are commonly used methods for chemical modification.

When a metal alkoxide $(OR)_n$ reacts with an organic acid (R''COOH), it exchanges its alkoxy (OR) group with a carboxylate group (R''COO) and produces a metal alkoxide carboxylate, $(M(OR)_{n-1}OOCR'')$ and an alcohol (ROH). Equation **3.4** shows the reactions between a metal alkoxide and an organic acid that can continue by further exchange of alkoxy (OR) groups with carboxylate groups. When all of the alkoxide groups are exchanged, a metal salt $(M(OOCR'')_n)$ forms.[6]

$$M(OR)_n + R''COOH \rightarrow M(OR)_{n-1}(OOCR'') + ROH$$
$$M(OR)_{n-1}(OOCR'') + R''COOH \rightarrow M(OR)_{n-2}(OOCR'')_2 + ROH$$
$$\vdots \qquad \vdots \qquad \vdots \qquad \vdots \qquad \text{(Equation 3.4)}$$
$$M(OR)(OOCR'')_{n-1} + R''COOH \rightarrow M(OOCR'')_n + ROH$$

Different metal alkoxides can react at different rates in all these reactions and therefore can lead to formation of different chemical complexes.[3] One of the ways of improving the chemical homogeneity of a solution is by reacting two or more metal

alkoxides to form a heterometallic alkoxide.[7] Equation **3.5** shows formation of a double metal alkoxide from two different metal alkoxides having the same alkoxide (OR) groups.

$$M(OR)_n + M'(OR)_n \rightarrow MM'(OR)_{2n} \qquad \text{(Equation 3.5)}$$

When a metal alkoxide precursor is not available for the required metal or the metal alkoxide is not soluble in the selected alcohol, a metal salt like a nitrate ($M(NO_3)_n$) or an acetate ($M(CH_3COO)_n$) can be used instead.[6] However, use of the metal salts provides new anions that can modify chemical reactions.

### 3.2 Precursor and Solvent Selection for Silver Tantalum Niobate System:

Synthesis of a chemical solution for the silver tantalum niobate, $Ag_x(Ta_yNb_{1-y})O_z$, system requires precursors of silver, tantalum and niobium and solvents that can dissolve the precursors and stabilize the reactions between precursors and solvents. An ideal way of synthesizing a new solution is through the use metal alkoxide precursors with an alcohol solvent having a long alkyl group to keep the chemical reactions simple while providing some stability against hydrolysis reactions. However, depending on the availability of metal alkoxide precursors and the reactions between precursors and solvents, both selected precursors and solvents may need to be modified.

Although there were several niobium and tantalum alkoxide precursors available, there was no available silver alkoxide precursor. Therefore, niobium and tantalum

alkoxides and a silver salt were selected as precursors. Niobium ethoxide ($Nb(OCH_2CH_3)_5$) and tantalum ethoxide ($Ta(OCH_2CH_3)_5$) were chosen as precursors because they were used successfully together in synthesis of potassium tantalum niobate solutions and sol-gel derived powders.[8, 9] Silver acetate ($AgOOCCH_3$) and silver nitrate ($AgNO_3$) were two available silver salt precursors. Silver nitrate was selected over silver acetate in this work because it had a better solubility in 2-methoxyethanol ($CH_3OCH_2CH_2OH$) than silver acetate. It should, however, be noted that there are relatively few references on the preparation of silver oxide-containing compounds by a sol-gel process. The majority of the literature concentrates on the precipitation of Ag to form oxide–metallic nanoparticle composites.[10, 11] For example, silver nitrate was used successfully in investigation of silver in sol-gel derived silica glass and $YBa_2Cu_3O_{7-x}$ superconductor composite powders requiring a homogenous distribution of the silver precursor. Consequently, it was realized that the silver-containing solutions utilized here may have a propensity for phase separation of the Ag component.

2-methoxyethanol (2-MOE) was selected as the main solvent. It dissolves all of the selected precursors well and has been used successfully to synthesize many other solutions involving titanium, zirconium and niobium alkoxides by providing hydrolysis stability to the alkoxide precursors.[12]

### 3.3 Silver Tantalate Niobate Chemical Solution Synthesis:

This section details the attempts made to produce stable solutions for production of $AgNb_{1-x}Ta_xO_3$ films. Initial efforts focused on use of 2-MOE alone as the solvent.

However, it was subsequently determined that double alkoxide formation in combination with pyridine modification of the solution resulted in improved solutions.

### 3.3.1 Investigation of Precursor Stabilities with 2-Methoxyethanol as a Single Solvent:

In order to observe the stability of the precursors with each other in 2-MOE, equimolar amounts of niobium ethoxide, tantalum ethoxide, (Chemat Technology, Northridge, CA) and silver nitrate (Alfa-Aesar Company, Ward Hill, MA) were dissolved in 2-methoxyethanol (Sigma-Aldrich Chemical Company, Milwaukee, WI) to produce a 0.25 M Ag-Ta-Nb solution at room temperature (Figure **3.1**). (Here, this solution had a 1/1/1 molar ratio of Ag/Ta/Nb precursors.) The solution was stirred at 120 rpm under a dry Argon ambient. The solution had a light yellow color initially. However, it turned brownish within 20 minutes and Ag (ICDD 4-783) was found to precipitate out in 4 hrs at room temperature. This showed clearly that the precursors were not stable with each other in 2-MOE.

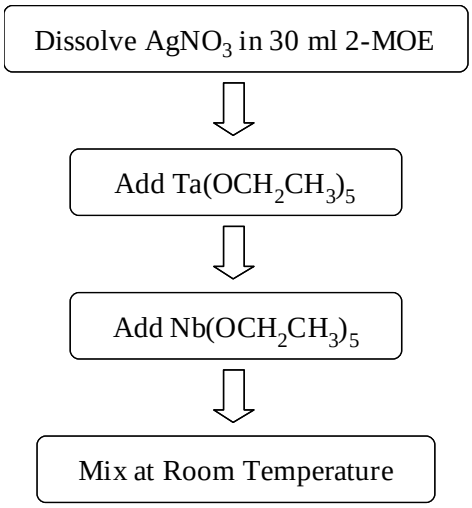


Figure **3.1**: 0.25 M Ag-Ta-Nb solution trial at room temperature.

To identify the reactions that were leading to precipitation, niobium and tantalum ethoxides were prereacted with each other and then reacted with the silver nitrate in 2-MOE (Figure **3.2**). A 0.15 M Ag-Ta-Nb solution was prepared as follows: niobium and tantalum ethoxides were dissolved in 2-MOE and reacted at 110 °C for 2 hours. The resulting solution had a light yellow color without showing precipitation, suggesting that niobium and tantalum ethoxides were stable with each other in 2-MOE. Silver nitrate was dissolved in 2-MOE in a separate flask and reacted for 2 hours at 110°C. When the silver nitrate solution was added into the niobium and tantalum double alkoxide solution at 110 °C, the mixture turned brown in seconds and precipitated out mostly silver in a minute. Thus, the silver precursor was determined to be unstable with niobium and tantalum ethoxides in 2-MOE.

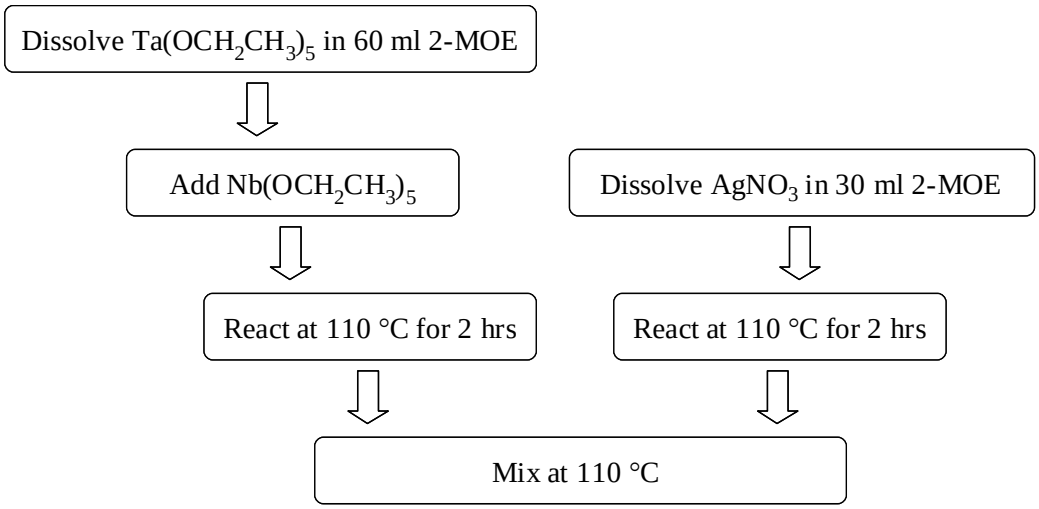


Figure **3.2**: 0.15 M Ag-Ta-Nb solution trial at 110 °C.

In order to investigate the individual stabilities of niobium and tantalum ethoxide precursors with the silver nitrate precursor, a 0.10 M $Ag_{0.4}$-Nb solution (having Ag/Nb molar ratio of 0.4/1) and a 0.08 M $Ag_{0.5}$-Ta solution were prepared separately in the same manner at 110 °C (Figure **3.3**). While the $Ag_{0.4}$-Nb solution precipitated in 5 minutes, the $Ag_{0.5}$-Ta solution precipitated after an hour. This suggested that both the niobium and tantalum precursors were reacting with the silver precursor, though with different rates, and that both needed to be modified.

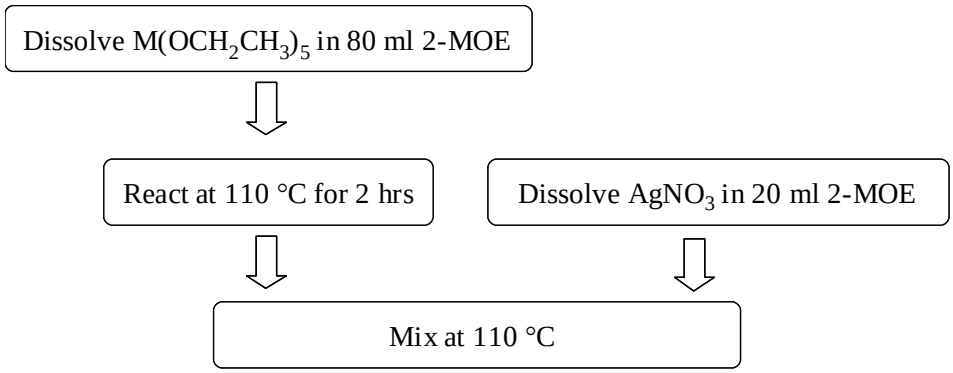


Figure **3.3**: 0.10 M $Ag_{0.4}$-Nb and 0.08 M $Ag_{0.5}$-Ta solutions trial at 110 °C.

### 3.3.2 Chemical Modification of Niobium and Tantalum Precursors to Inhibit Silver Precipitation:

Acetic acid ($CH_3COOH$) is one of the organic acids used to modify metal alkoxide precursors chemically to make them more stable against hydrolysis reactions.[4, 5] When acetic acid is reacted with a metal alkoxide, the acetate group ($OOCCH_3$) replaces some of weakly bounded alkoxide groups (OR) and therefore is expected to slow down hydrolysis reactions. [13]

Niobium and tantalum ethoxides were modified with glacial acetic acid (J. T. Baker Chemical Company, Phillipsburg, NJ) separately to slow down reactions between the silver and alkoxide precursors in 2-MOE. In order to find the optimal amount of acetic acid, 1/1, 3/1, 5/1 and 8/1 acetic acid to niobium ethoxide concentrations were prepared for 0.25 M Ag-Nb solutions (Figure **3.4**). While the solution having a 1:1 acetic

acid: niobium ethoxide concentration was stable for only 20 min., the stability of the solutions increased to a day for a 3:1 ratio and to 3 days for a 5:1 ratio. However, further increases in the acetic acid to niobium ethoxide ratio decreased the stability of the solution to less than a day. A similar decrease in stability with excess acetic acid was also observed in other systems due to the reaction between the excess acetic acid and removed ethyl alcohol groups, producing ester and water (Equation **3.6**).[5]

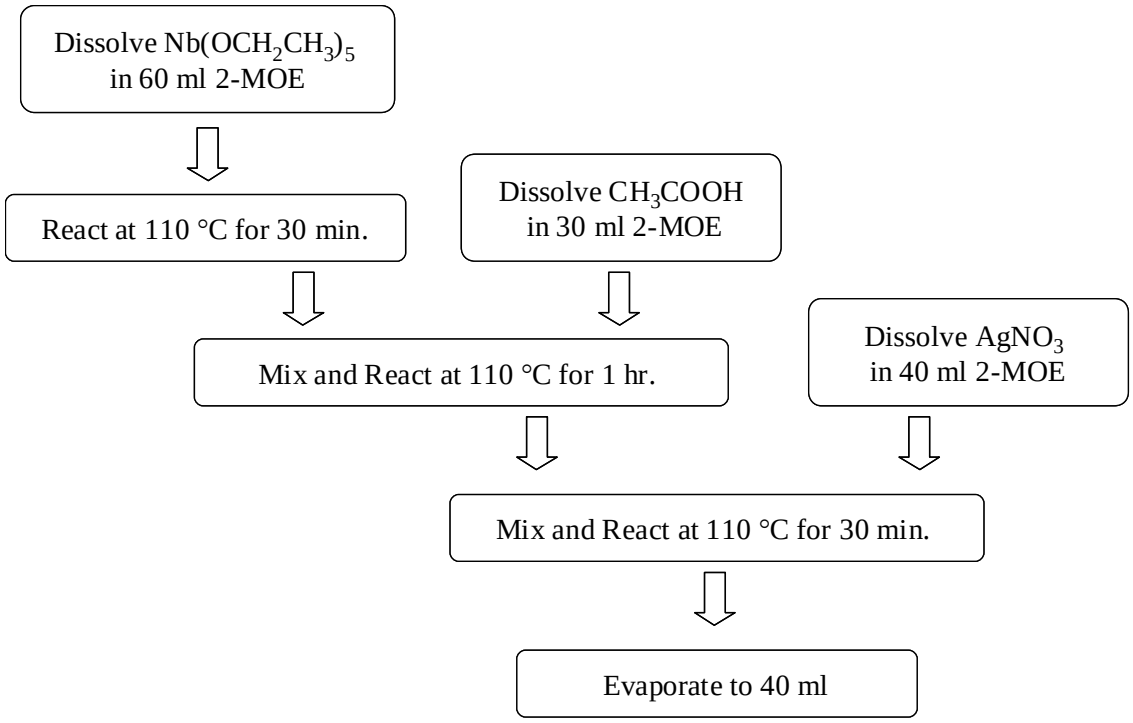


Figure **3.4**: 0.25 M Ag-Nb Solution trial with acetic acid modifications of niobium ethoxide precursor.

$$C_2H_5OH + CH_3COOH \rightarrow CH_3COOC_2H_5 + H_2O \qquad \text{(Equation 3.6)}$$

When tantalum ethoxide was modified with acetic acid at 2:1 and 5:1 acetic acid to tantalum ethoxide concentrations and then reacted with silver nitrate, both solutions were found to precipitate in 30 min. Therefore, acetic acid modification of tantalum ethoxide was not effective in slowing down the reactions between silver nitrate and tantalum ethoxide in 2-MOE.

### 3.3.3 Chemical Modification of Silver Precursor with Use of Pyridine as a Second Solvent:

Modifying alkoxide precursors chemically with acetic acid failed to slow down the reactions between silver nitrate and niobium and tantalum ethoxides with 2-MOE as a single solvent. The next approach was modifying the silver precursor by using pyridine as a second solvent. Pyridine was chosen because it was known to form complexes with silver and has been successfully used together with 2-MOE in synthesis of bismuth zinc niobate solutions.[14, 15]

A 0.5 M Ag-Ta-Nb solution was prepared using 2-MOE and pyridine (Sigma-Aldrich Chemical Company, Milwaukee, WI) as follows: niobium and tantalum ethoxides were dissolved in 2-MOE and reacted for 2 hrs at 110 °C, silver nitrate was dissolved in pyridine at room temperature and added into the 2-MOE mixture at room temperature (Figure **3.5**). The resulting solution had a light yellow color after mixing and was stable for more than 2 weeks.

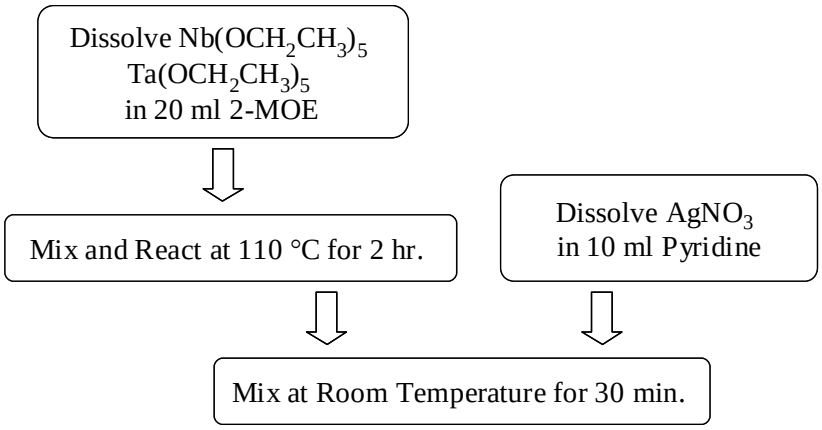


Figure **3.5**: 0.5 M Ag-Ta-Nb solution trial by using pyridine–2-MOE solvents.

Following the same procedure, a more concentrated (0.75 M) Ag-$Ta_{0.5}$-$Nb_{0.5}$ solution was also synthesized successfully. Thus, use of pyridine as a second solvent proved to be a powerful way to stabilize the solution against reactions leading to silver precipitation. Pyridine is known to react with silver and form many pyridine–silver complexes.[16] Formation of silver pyridine complexes and their slower reaction rates with other precursors may be responsible for the increased stability.

In order to investigate the effects of modifications in the solution preparation steps on the stability of the solution, the reaction duration of niobium and tantalum precursors in 2-MOE at 110 °C, the reaction temperature of pyridine-2-MOE solutions, the volume ratio of pyridine to 2-MOE, and the reaction duration of pyridine -2-MOE solutions at 110 °C were varied. For a 0.3 M solution, decreasing the duration of the niobium–tantalum reaction in 2-MOE from 2 to 1 hour, increasing the reaction temperature of pyridine–2-MOE solutions from room temperature to 110 °C and

increasing the reaction duration of pyridine-2-MOE solutions from 5 to 15 minutes at 110 °C did not lead to any precipitation of the solution. However, when the duration of the reaction between pyridine-2-MOE solutions increased to 1 hour at 110 °C, the solution was found to precipitate. Therefore, this step was kept shorter. When the volume ratio of pyridine to 2-MOE solutions was decreased from 0.5 to 0.25, the solution precipitated. Thus, the volume ratio of the pyridine to 2-MOE solvents was kept as 0.5 in the synthesis of all subsequent solutions.

The optimal process conditions for the solution synthesis for a 0.3 M Ag-$Ta_{0.5}$-$Nb_{0.5}$ solution were as follows: stoichiometric amounts of niobium and tantalum ethoxides were added into 2-methoxyethanol (2-MOE) in a glove box and the mixture was transferred to a rotary evaporator. About 2 ml of the 2- MOE mixture was evaporated under vacuum at 110 °C to remove any water absorbed during transfer. The 2-MOE mixture was then reacted at 110 °C by rotating the glass flask at 120 rpm for an hour under dry argon flow in a rotary evaporator. The 2-MOE solution had a bright light yellow color at the end of the reaction. In a separate flask, the silver nitrate was dissolved at room temperature in pyridine under a dry argon atmosphere in a glove box. Subsequently, the pyridine mixture was added into the 2-MOE solution and reacted at 110 °C for 5 min under dry argon in the rotary evaporator while rotating at 120 rpm. The resulting 0.3 M solution had a light yellow color and was stable up to a month when kept sealed under a dry ambient. When a $AgTa_{0.5}Nb_{0.5}$ solution precipitated, it followed the following steps; first it turned dark yellow, then brownish and it ended with blackish silver precipitates.

### 3.4 Analysis of Ag-$Ta_{0.5}$-$Nb_{0.5}$ Solution and Dried Powders:

Thermogravimetric analysis and differential thermal analysis (TGA and DTA) analysis of the Ag-$Ta_{0.5}$-$Nb_{0.5}$ solution were performed simultaneously by using a TA instrument (model SDT2960) to investigate the organic removal and crystallization steps. In order to prepare the powder used in the TGA-DTA study, the chemical solution was dried overnight at 200 °C in air. The measurement was performed by heating the dried powder at 2 °C/min. to 200 °C under $O_2$ flow. After stabilizing at 200 °C for 10 min., the powder was heated to 800 °C at a rate of 10 °C/min. and then held at this temperature for 30 min. Finally, the powder was cooled down to room temperature under oxygen $O_2$ flow.

TGA and DTA curves of the dried powder (Figure **3.6**) show a large weight loss and a broad exothermic peak as the temperature reached 350 °C, where most of the organics were removed. With further heating, a small additional weight loss continued slowly until the temperature reached 630 °C. At this temperature, there was a small exothermic peak in the DTA curve showing crystallization of the powder. No weight loss or thermal peaks were observed at higher temperatures, suggesting no reaction occurred on further heating the powder to 800 °C, holding for 30 min. and cooling back to room temperature. X-ray diffraction profile of the resulting powder (Figure **3.7**) showed only the pseudocubic perovskite crystal structure (ICDD 89-7738).

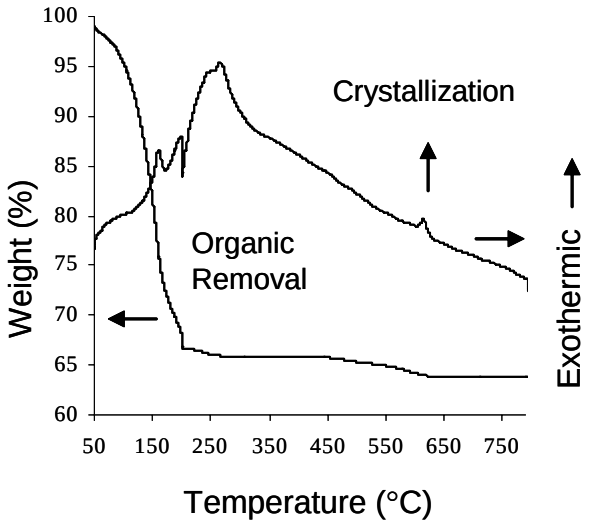


Figure **3.6**: TGA and DTA curves of Ag-$Ta_{0.5}$-$Nb_{0.5}$ solution dried powder heated at 10 °C/min. under $O_2$ ambient.

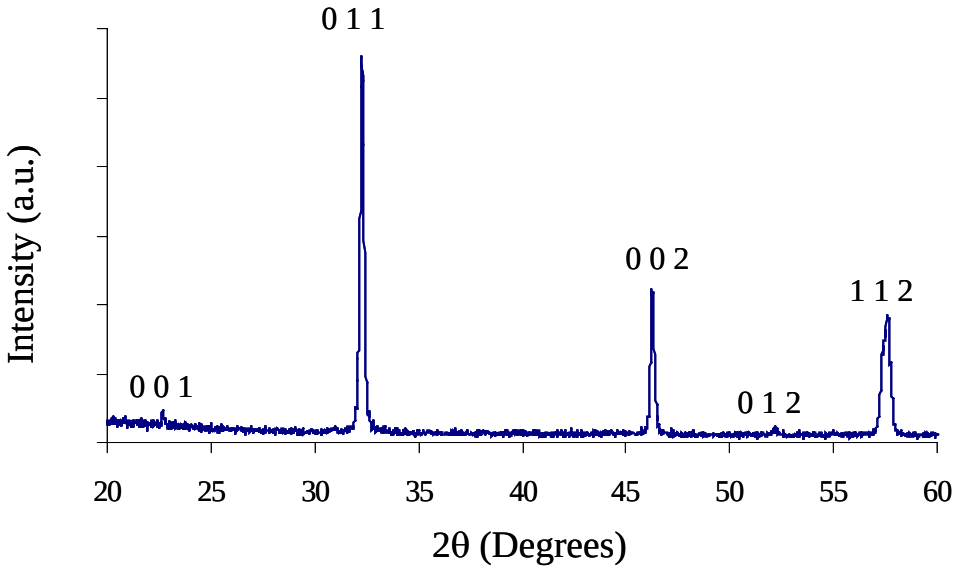


Figure **3.7**: XRD profile of Ag-$Ta_{0.5}$-$Nb_{0.5}$ solution dried powder resulted from TGA – DTA study showing formation of only $Ag(Ta_{0.5}Nb_{0.5})O_3$ with a pseudocubic perovskite crystal structure.

### 3.5 Synthesis of Solutions having Compositions other than Ag-$Ta_{0.5}$-$Nb_{0.5}$:

Ag-Ta and Ag-Nb solutions for the perovskite end member compositions of ($AgTaO_3$ and $AgNbO_3$) and several Ag deficient compositions were successfully synthesized using the developed synthesis route. Figure **3.8** shows a ternary map showing the compositions of the chemical solutions synthesized successfully.

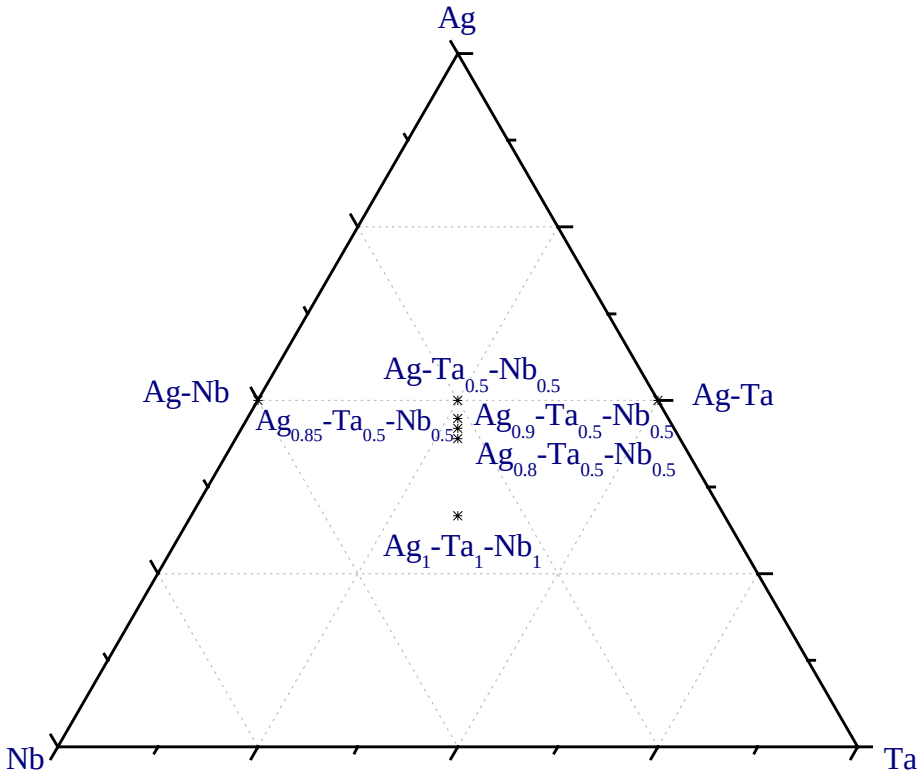


Figure **3.8**: Ternary map showing chemical compositions of successfully synthesized solutions using the synthesis steps developed for $AgTa_{0.5}Nb_{0.5}$ solutions. The oxide content is not shown.

## 3.6 Conclusions:

A stable chemical solution route was developed for the silver tantalate niobate system, $Ag_x(Ta_yNb_{1-y})O_z$. Stability of niobium and tantalum precursors with the silver precursor was a problem with the use of 2-MOE as the sole solvent, and silver precipitation was observed. Acetic acid modifications of the niobium and tantalum precursors did not eliminate the problem. However, prereacting the silver precursor with pyridine produced stable solutions having a wide range of compositions, including the Ag-Ta and Ag-Nb end members and silver deficient compositions compared to a Ag-$Ta_{0.5}$-$Nb_{0.5}$ solution.

Thermal gravimetric analysis and differential thermal analysis of a powder made by drying Ag-$Ta_{0.5}$-$Nb_{0.5}$ solution overnight at 200 °C in air, showed that most of the organics were removed when the temperature reached 350 °C and the powder crystallized at 630 °C to phase pure pseudocubic perovskite $Ag(Ta_{0.5}Nb_{0.5})O_3$.

## 3.7 References:

[1] C. J. Brinker and G. W. Scherer, *Sol-Gel Science: The Physics and Chemistry of Sol-Gel Processing,* Academic Press Inc., San Diego, CA, (1990).

[2] H. Schmidt, "Chemistry of material preparation by the sol-gel chemistry," *Journal of Non-Crystalline Solids*, **100** 51-64 (1988).

[3] D. C. Bradley, R. C. Mehrotra, I. P. Rothwell and A. Singh, *Alkoxo and Aryloxo Derivatives of Metals,* Academic Press Inc., San Diego, CA, (2001).

[4] R. C. Mehrotra, "Chemistry of alkoxide precursors," *Journal of Non-Crystalline Solids,* **121** 1-6 (1990).

[5] C. Sanchez, J. Livage, M. Henry and F. Babonneau, "Chemical modification of alkoxide precursors," *Journal of Non-Crystalline Solids*, **100** 65-76 (1988).

[6] M. Guglielmi, G. Capturan, "Precursors for sol-gel preparation," *Journal of Non-Crystalline Solids*, **100** 16-30 (1988).

[7] A. C. Pierre, *Introduction to Sol-Gel Processing*, Kluwer Academic Publisher, Norwell, MA, (1998).

[8] S. Hirano, T. Yogo, K. Kikuta, T. Morishita and Y. Ito, "Preparation of potassium tantalate niobate by sol-gel method," *Journal of the American Ceramic Society*, **75** 1701-1704 (1992).

[9] S. Wang, Z. Li, D. Zang, G. Zhang, J. Sun and P. Zheng, "Dielectric, ferroelectric properties of $KTa_{0.65}Nb_{0.35}O_3$ thin films by sol-gel process on Pt(111)/Ti/MgO(100) substrates," *Journal of Sol-Gel Science and Technology*, **17** 159-162 (2000).

[10] B. Ritzer, M. A. Villegas, and J. M. F. Navarro, "Influence of temperature and time on stability of silver in silica sol-gel glasses," *Journal of Sol-Gel Science and Technology*, **8** 917-921 (1997).

[11] M. K. Agarwala, D. L. Bournell and C. Persad, "Synthesis of high-$T_c$ dual phase $YBa_2Cu_3O_{7-x}$ superconductor composite powders by sol-gel process," *Journal of the American Ceramic Society*, **75** 1975-1977 (1992).

[12] M. Sedlar and M. Sayer, "Reactivity of titanium isopropoxide, zirconium propoxide and niobium ethoxide in the system of 2-methoxyethanol, 2,4 - pentanedione and water," *Journal of Sol-Gel Science and Technology*, **5** 27-40 (1995).

[13] S. Doeuff, M. Henry, C. Sanchez and J. Livage, "Hydrolysis of titanium alkoxides: modification of molecular precursor by acetic acid," *Journal of Non-Crystalline Solids*, **89** 206-216 (1987).

[14] P. Tomasik and Z. Ratajewicz, *Pyridine – Metal Complexes*, Interscience Publications, New York, NY, (1985).

[15] W. Ren, S. Trolier-McKinstry, C.A. Randall and T.R. Shrout, "Bismuth zinc niobate pyrochlore dielectric thin films for capacitive applications," *Journal of Applied Physics*, **89** 767-774 (2001).

[16] P. Tomasik and Z. Ratajewicz, *Pyridine – Metal Complexes*, Interscience Publications, New York, NY, (1985).

# Chapter 4

## $Ag_x(Ta_{0.5}Nb_{0.5})O_z$ Thin Films on (111)Pt/Ti/$SiO_2$/(100)Si Substrates

### 4.1 Introduction:

The first substrate used for chemical solution deposition of $Ag(Ta_{0.5}Nb_{0.5})O_3$ thin films (ATN) was (111)Pt/Ti/$SiO_2$/(100)Si, which will be referred to as Pt/Si. Platinum was anticipated to stay chemically inert with the ATN films during the heat treatment steps and serves as a bottom electrode during dielectric characterization. Deposition of the ATN films was done by spin-coating the solution on the substrate, pyrolyzing and crystallizing. Multiple layers were deposited to build up thicker films. Figure **4.1** is a flow chart showing typical spinning and heat treatment steps used during chemical solution deposition of ATN films on Pt/Si substrates. Optimization of each step was undertaken in order to prepare dense, crack-free films. It was found that it is extremely difficult to prepare phase-pure perovskite ATN in this way.

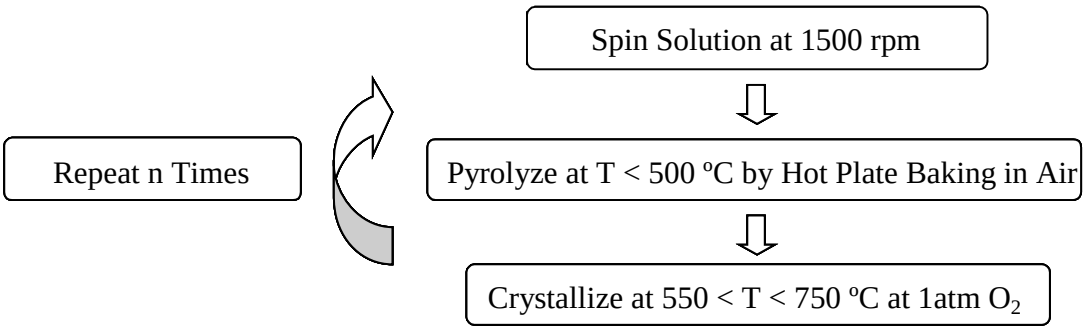


Figure **4.1**: Typical spinning and heat treatment of ATN films on (111)Pt/Ti/$SiO_2$/(100)Si substrates.

Before going through experimental results, it is important to review classical nucleation theories briefly to outline the importance of the type of substrate and heat treatment steps on the crystal structure and orientation of chemical solution deposited films. It is widely known that the type of the substrate and the heat treatment steps affect both the crystal structures and orientations of films.[1, 2]

A new phase can nucleate homogenously or heterogeneously depending on whether existing surfaces participate during the nucleation. In homogenous nucleation, the new phase forms to decrease the chemical free energy by creating a new surface without use of any existing surfaces. The total free energy change for forming a spherical nucleus by homogenous nucleation is given in Equation **4.1**.[3]

$$\Delta G = \frac{4}{3}\pi r^3 \Delta G_v + 4\pi r^2 \gamma \qquad \text{(Equation 4.1)}$$

where:

$\Delta G_v$ : Change in chemical free energy per unit volume due to forming the new phase

$r$ : Radius of nucleus

$\gamma$ : Surface energy per unit area needed to form a surface between the new phase and the existing phase

The first term in equation 4.1 shows the chemical driving force for the phase transition, which must be negative for the crystallization to proceed. The second term in the equation shows the energy required for creating a surface between the new phase and the existing phase and it is positive. In order for a phase to nucleate and grow, the chemical potential change should be negative. Based on the size of the nucleus, there is an energy barrier $\Delta G^*$ and critical nucleus size $r^*$ that are calculated by setting $d\Delta G/dr = 0$ and solving for $\Delta G^*$ (Equation **4.2**) and $r^*$ (Equation **4.3**). When momentarily forming an atomic cluster that has a radius bigger than some critical radius $r^*$, the total free energy change becomes negative, the atomic cluster becomes a stable nucleus and it grows. Having a high chemical driving force, $\Delta G_v$, lowers the energy barrier and the required critical size and therefore increases the rate of nucleation of the new phase.[3]

$$\Delta G^* = \frac{16\pi\gamma^3}{3\Delta G_v^2} \qquad \text{(Equation 4.2)}$$

$$r^* = -\frac{2\gamma}{\Delta G_v} \qquad \text{(Equation 4.3)}$$

For the case of heterogeneous nucleation, a new phase forms on an existing surface and the total free energy change depends on the change in surface energies. For example, in the case of nucleation from a substrate, the relevant surface energies are the substrate surface-pyrolyzed amorphous film, new phase-pyrolyzed amorphous film and substrate surface-new phase. For a cap-shaped nucleus of a new phase on an existing planar surface (Figure 4.2), the total free energy change is given in Equation 4.4.

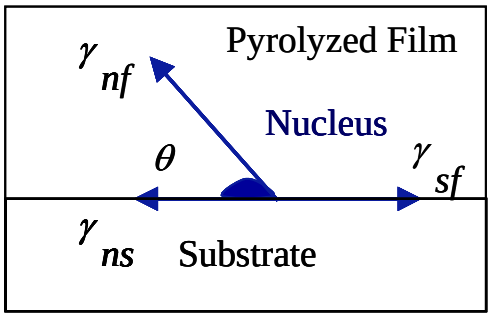


Figure 4.2: Schematic showing heterogeneous nucleation of a cap-shaped crystallite in a pyrolyzed film on an existing surface together with the related surface energy terms and contact angle θ.

$$\Delta G_h = \frac{\pi(2-3\cos\theta+\cos^3\theta)}{3} r^3 \Delta G_v + 2\pi(1-\cos\theta) r^2 \gamma_{nf} + (\pi \sin^2\theta) r^2 \gamma_{ns} - (\pi \sin^2\theta) r^2 \gamma_{sf} \qquad \text{(Equation 4.4)}$$

where:

$\Delta G_v$ : Change in chemical free energy per unit volume

$\theta$ : Contact angle of nucleus

$r$ : Radius of nucleus

$\gamma_{nf}$ : Surface energy of the new phase-pyrolyzed amorphous film per unit area

$\gamma_{ns}$ : Surface energy of the new phase-substrate surface per unit area

$\gamma_{sf}$ : Surface energy of the new phase-pyrolyzed amorphous film per unit area

The first term in equation 4.4 shows the chemical driving force for a crystallite volume of $\frac{\pi(2-3\cos\theta+\cos^3\theta)}{3}r^3$ and it must be negative for crystallization to proceed. The second and third terms show the energy required to create a new phase – pyrolyzed amorphous film surface with a curved area of $2\pi(1-\cos\theta)r^2$ and a substrate surface-new phase surface with a projected area of $(\pi\sin^2\theta)r^2$. The fourth term is the surface energy of the substrate surface-pyrolyzed amorphous film that is replaced during the nucleation of the new phase and is negative.

Thus the energy barrier for heterogeneous nucleation, $\Delta G_h^*$ depends on the surface energies and could be written as in Equation **4.5** in terms of the contact angle for a hemispherical nucleus on a planar substrate.[3] As shown in the equation, the energy barrier for heterogeneous nucleation is a fraction of the energy barrier required for homogenous nucleation. Therefore, the substrate and the surface energy terms have an important effect on the crystal structures formed for the films.[1]

$$\Delta G_h^* = \Delta G^* \left( \frac{2 - 3Cos\theta + Cos^3\theta}{4} \right)$$ (Equation **4.5**)

Both homogenous and heterogeneous nucleation can occur at the same time, depending on the driving force and surface energy terms of the amorphous film on the substrate. The driving force is based on the thermodynamic stability of the new phase.

In addition, the nucleation and growth rates of all phases encountered during the heat treatment steps introduce a kinetic aspect to the transformations. All these different aspects of phase formation make the crystal structure development of chemical solution deposited films quite interesting as well as challenging to control.

## 4.2 Crystal Structure Development of $Ag(Ta_{0.5}Nb_{0.5})O_3$ Thin Films on (111)Pt/Ti/$SiO_2$/(100)Si Substrates:

The initial processing procedure employed for the ATN films was adapted from chemical solution deposition processing of lead zirconate titanate, another perovskite.[4] ATN films on Pt/Si substrates were prepared from a 0.4 M solution by spinning at 1500 rpm. The layers were heat treated at 200 °C in air, followed by organic removal at 400 °C and crystallization between 550 to 750 °C in an $O_2$ ambient using a quartz tube furnace. Figure **4.3** shows the details of film deposition steps used for the first set of ATN films.

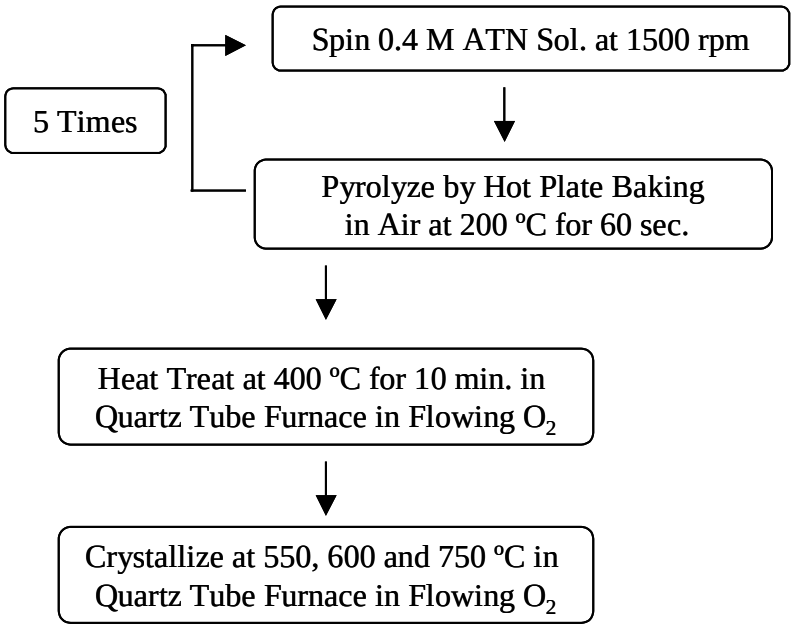


Figure **4.3**: Chemical solution deposition of first set of $Ag(Ta_{0.5}Nb_{0.5})O_3$ films on (111)Pt/Ti/$SiO_2$/(100)Si substrates crystallized using a quartz tube furnace.

X-ray diffraction profiles of the resulting ATN films as a function of crystallization temperature (Figure **4.4**) showed that crystallization was initiated at temperatures as low as 550 °C. However, the films were not phase pure and had a mixture of an unknown and a pseudocubic perovskite phases. The XRD peak at 29.02° 2θ was observed for all of the films deposited on Pt/Si substrates, but not for the chemical solution derived powder.

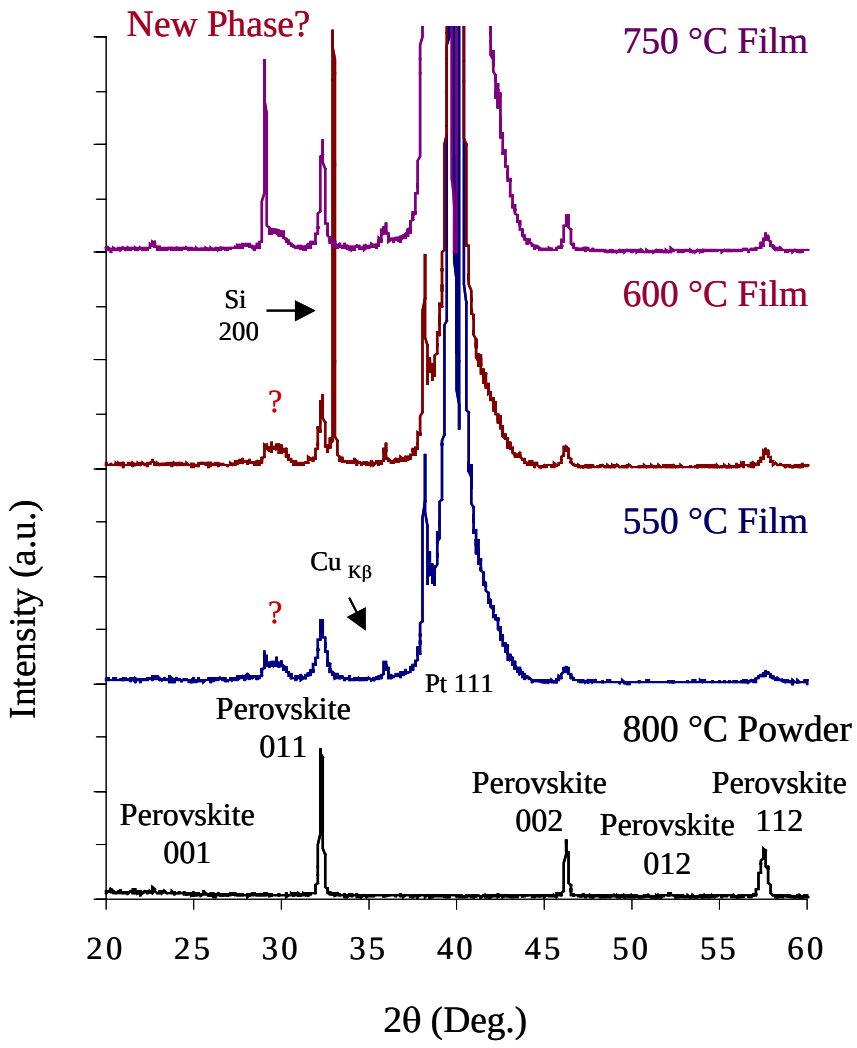


Figure **4.4**: XRD patterns of chemical solution derived $Ag(Ta_{0.5}Nb_{0.5})O_3$ powder and films crystallized on (111)Pt/Ti/$SiO_2$/(100)Si substrates using a quartz tube furnace in flowing $O_2$: (a) Powder heat treated at 800 °C for 30 min. in flowing $O_2$, (b) Film crystallized at 550 °C for 3 min., (c) Film crystallized at 600 °C for 10 min. (d) Film crystallized at 750 °C for 10 min. and unknown phase peaks are marked with a question mark.

As will be shown in section 4.3, the resulting films had comparatively low dielectric constants (ranging from 200 to 270), well below the reported value for bulk ATN 50/50 ceramics ($\varepsilon_r$ ~410).[5]

It is important to control formation of secondary phases to optimize the film dielectric properties. Both low temperature heat treatment steps and heating rates during crystallization have been shown to be critical in many lead-based perovskite films in controlling the amounts of perovskite and pyrochlore phases.[4] Therefore, the effects of the low temperature heat treatment steps and the heating rates to crystallization temperatures are described in detail in sections 4.2.3 and 4.2.4.

### 4.2.1 Transmission Electron Microscope Investigation of Films:

It was impossible to identify the new phase based on XRD patterns alone, since there were too few peaks available, so the structure was investigated by electron diffraction in the transmission electron microscope (TEM). Thus a film was prepared (as shown in Table 4.1) having strong new phase XRD peaks (as shown in Figure 4.4).

Table 4.1: Heat treatment details and resulting phases of the two ATN films for TEM investigation

| Film Number | Thickness (nm) | Crystallization Conditions | Phases Present |
|---|---|---|---|
| 1 | 330 | 11 X 175 °C and 1 X 550 °C | Mostly new phase and some perovskite |
| 2 | 450 | 5 X 200 °C, 1X 400 °C and 1 X 750 °C | Little new phase and some perovskite |

The transmission electron microscope (TEM) investigation of transverse and plan view samples was performed using three different TEMs: a 120 kV Philips 420 TEM (Eindhoven, The Netherlands), a 200 kV Jeol 2010 $LaB_6$ TEM (Peabody, MA) and a 200 kV Jeol 2010F field emission TEM (Peabody, MA) with an energy dispersive x-ray spectroscopy detector. Two different techniques were used to prepare transverse and plan view samples.[6, 7] In order to prepare transverse samples, two pieces of the film were fractured and glued face to face using quick setting epoxy resin. The sandwich structure was mounted onto a Gatan disc grinder using Crystalbond resin, ground and polished using 600, followed by 1000 grit silicon carbide paper till its thickness was reduced to around ~20 μm. The sample was removed from the grinder, epoxy glued on a copper ring and thinned to electron transparency by using a Fischione model 3000 ion mill (Export, PA). In order to prepare plan view samples, a piece was ground and polished from the silicon side, epoxy glued on a copper ring and ion milled from the silicon side to electron transparency.

A bright field image of a plan view sample (Figure **4.5**) showed that film one had second phase precipitates having a dark contrast in the image. Energy dispersive spectra of the precipitates suggested that the precipitates were rich in silver relative to the matrix. Due to their small size (<30 nm), it was not possible to determine if these were Ag, $Ag_2O$ or some other complex composition.

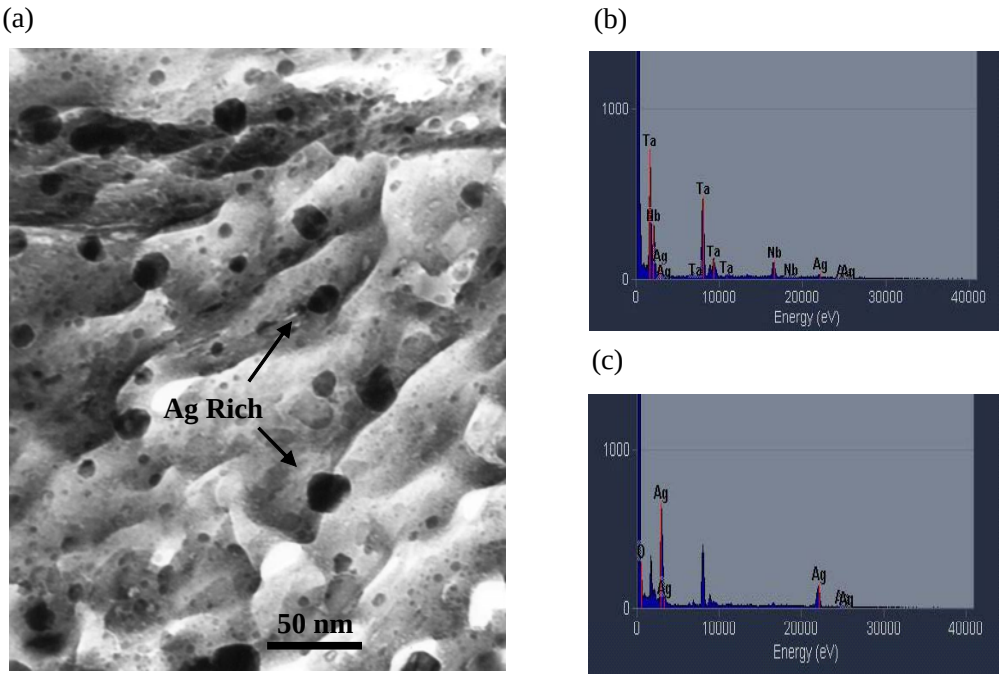


Figure **4.5**: Bright field image and energy dispersive spectroscopy profiles of sample 1 described in Table 4.1 taken at 200 kV. (a) Plan view image at 150 k magnification (b) Energy dispersion spectroscopy profile of matrix (c) Energy dispersion spectroscopy profile of a precipitate. (Courtesy of Dr. I. M. Reaney)

The cross section image (Figure **4.6**) showed that the film had some columnar grain structure in addition to silver rich precipitation. The silver rich precipitates existed throughout the thickness.

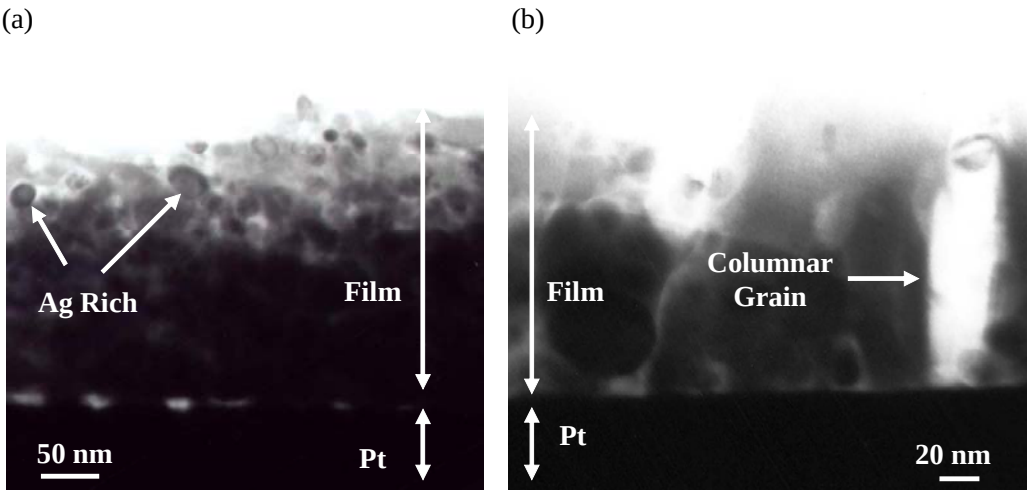


Figure **4.6**: Cross sectional images of sample one in Table 4.1 (a) Bright field image at 120 k magnification (b) Dark field image at 200 k magnification. (Courtesy of Dr. I. M. Reaney)

When the electron diffraction patterns of the samples were investigated, it was found that none of the observed patterns matched that of a pseudocubic perovskite phase. Figure **4.7** and Figure **4.8** show some of the observed electron diffraction patterns. It was possible to index these patterns based on the natrotantite crystal structure. The natrotantite crystal structure was reported for both bulk $Na_2Ta_4O_{11}$ and $Na_2Nb_4O_{11}$.[8] It has a space group of $R\bar{3}c$ and consists of two alternating layers along the z direction. Figure **4.9** shows 5 by 5 by 1 unit cells and (001) plane projections of the simulated natrotantite crystal structure for the $Ag_2(Ta_{0.5}Nb_{0.5})_4O_{11}$ composition drawn using CaRine Crystallography software with a hexagonal setting and estimated lattice parameters a = 6.2092 Å and c = 36.619 Å. The first layer along the z direction consists of edge sharing $(Ta,Nb)O_6$ octahedra embedded in a sheet of $AgO_7$ capped octahedra. The second layer

involves only edge sharing $(Ta,Nb)O_7$ pentagonal bipyramids. These two alternating adjacent layers are connected via corners and edges. The simulated powder XRD profile of $Ag_2(Ta_{0.5}Nb_{0.5})_4O_{11}$ having the natrotantite crystal structure is provided in Figure **4.10** where the most intense peaks are shown with their indices. The composition was adjusted to allow Ta and Nb solid solution (e.g. $Ag_2(Ta_{0.5}Nb_{0.5})_4O_{11}$).[9] The observed electron diffraction patterns were indexed based on simulated [210] and [001] zone axis electron diffraction patterns prepared using CaRIne Crystallography software.[10] The [210] zone axis electron diffraction pattern should be investigated in the future for whether there is any diffuse scattering.

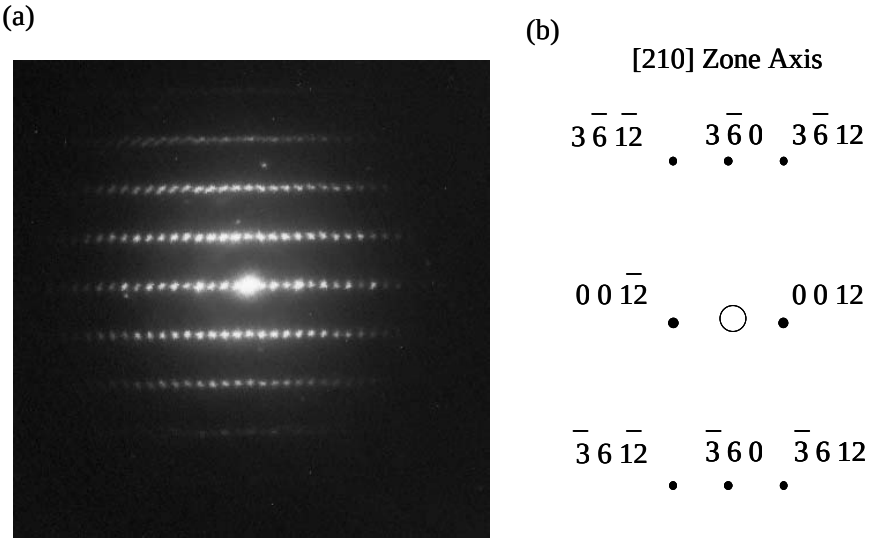


Figure **4.7**: Electron diffraction pattern of sample one in Table 4.1 (a) Observed electron diffraction pattern for a cross sectional sample taken at 200 kV (b) Simulated [210] zone axis electron diffraction pattern of $Ag_2(Ta_{0.5}Nb_{0.5})_4O_{11}$ with natrotantite crystal structure. (Courtesy of Dr. I. M. Reaney)

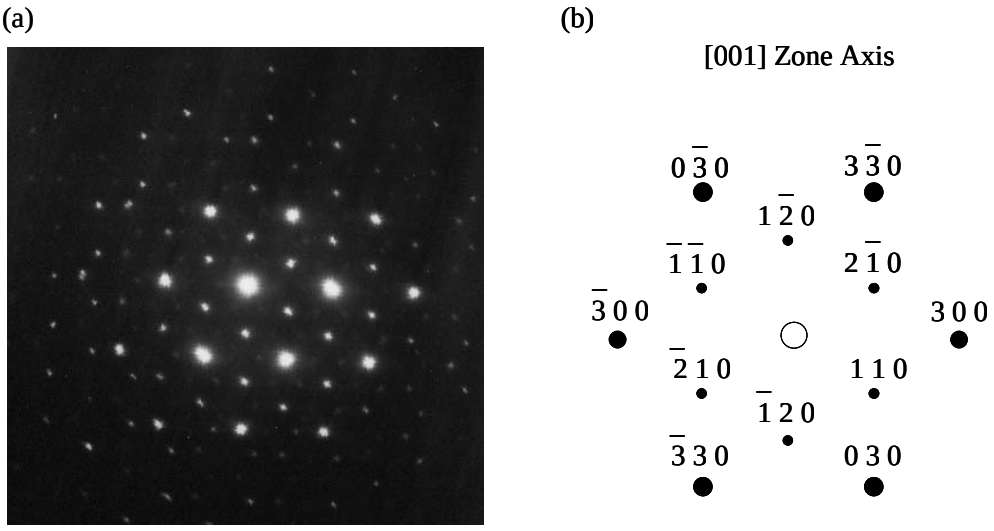


Figure **4.8**: Electron diffraction pattern of sample one in Table 4.1 (a) Observed electron diffraction pattern for a plan view sample taken at 200 kV (b) Simulated [001] zone axis electron diffraction pattern of $Ag_2(Ta_{0.5}Nb_{0.5})_4O_{11}$ with natrotantite crystal structure. (Courtesy of Dr. I. M. Reaney).

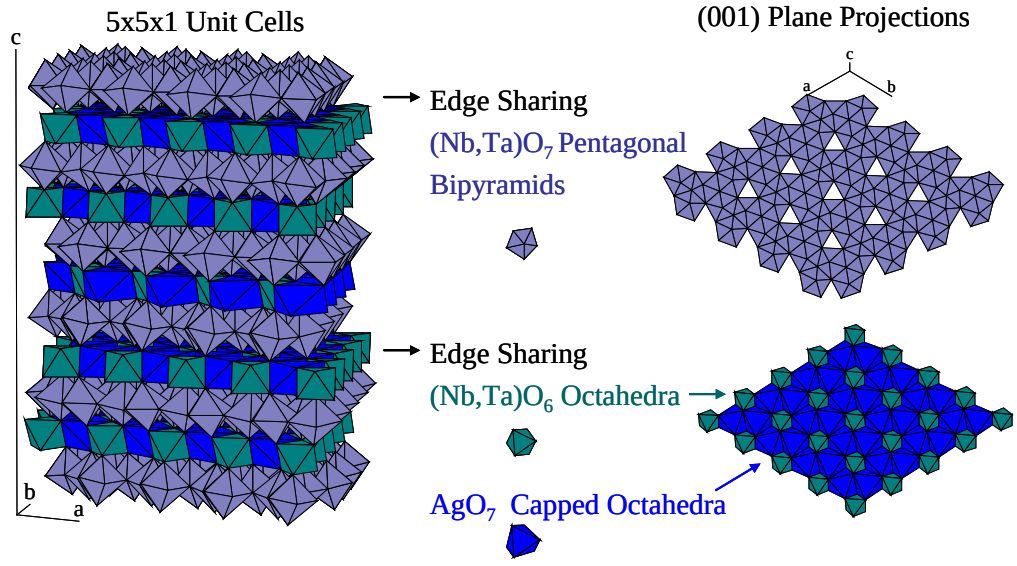


Figure **4.9**: Simulated $Ag_2(Ta_{0.5}Nb_{0.5})_4O_{11}$ with natrotantite crystal structure (space group: $R\bar{3}c$ with hexagonal setting) and (001) plane projections of two alternating layers.

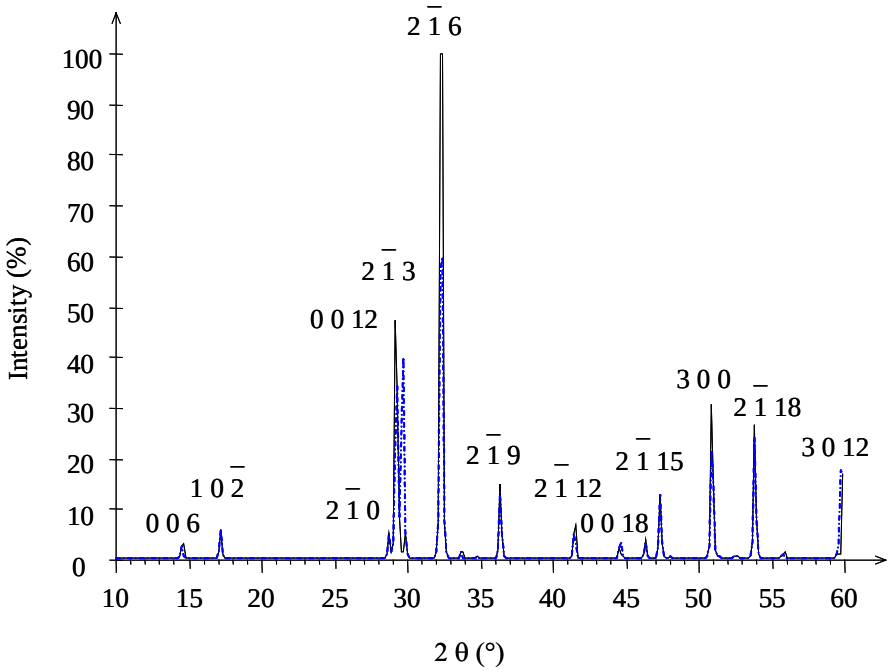


Figure **4.10**: Simulated powder XRD pattern of $Ag_2(Ta_{0.5}Nb_{0.5})_4O_{11}$ with natrotantite crystal structure.

Figure **4.11** is the XRD pattern of sample one in Table 4.1 superimposed over the simulated XRD pattern of $Ag_2(Ta_{0.5}Nb_{0.5})_4O_{11}$ with the natrotantite crystal structure. The sample had only intense 00*l* family natrotantite XRD peaks, suggesting that it had strong (00*l*) orientation. It would not have been possible to determine the crystal structure of the unknown phase based on three XRD peaks from the same family, proving the importance of the electron diffraction study for the structure determination.

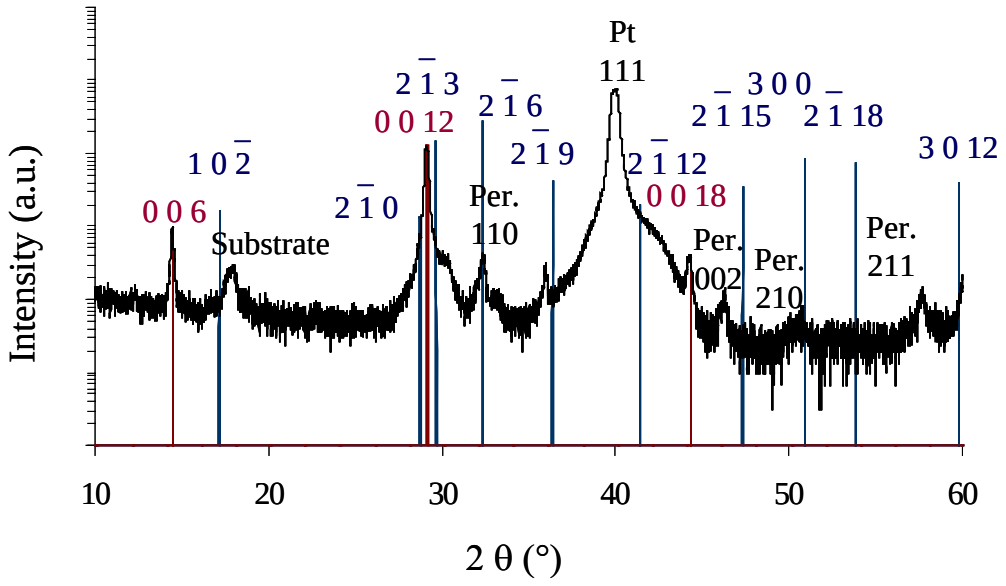


Figure **4.11**: XRD pattern of sample one in Table 4.1 superimposed over the simulated powder XRD pattern of $Ag_2(Ta_{0.5}Nb_{0.5})_4O_{11}$ with natrotantite crystal structure.

A Nelson-Riley extrapolation function (Equation **4.6**) is used to correct various systematic errors in XRD peak positions, such as displacement of the specimen from the diffractometer axis during data collection.[11] To calculate the lattice parameter $c_0$, the lattice parameters (c) of the 00*l* family peaks were plotted against the extrapolation function term $\left(\frac{\cos^2\theta}{\sin\theta}+\frac{\cos^2\theta}{\theta}\right)$ and a linear best fit to the y-intercept (where $\theta = 90°$) was used. The lattice parameter $c_0$ of $Ag_2(Ta_{0.5}Nb_{0.5})_4O_{11}$ phase was calculated as 36.24 ± 0.01 Å.

$$c = c_0 - c_0 k_2 \left( \frac{\cos^2\theta}{\sin\theta} + \frac{\cos^2\theta}{\theta} \right) \qquad \text{(Equation 4.6)}$$

where:

$c$: Lattice parameter with measurement errors

$c_0$: Lattice parameter

$\theta$: Bragg angle

$k_2$: Constant

The simultaneous appearance of silver rich precipitates and natrotantite was also consistent with the batch composition, since the composition of the natrotantite phase, $Ag_2(Ta_{0.5}Nb_{0.5})_4O_{11}$, is silver deficient compared to $Ag(Ta_{0.5}Nb_{0.5})O_3$.

The ATN film having the strongest perovskite XRD peaks (See Figure 4.4) among the films crystallized at 750 °C in a tube furnace (sample two in Table 4.1) was investigated by transmission electron microscope (TEM). The bright field TEM images (Figure **4.12**) show a cross section of the ATN film and the film-platinum interface. The film had equiaxed grains with an average size of ~150 nm and grain boundaries without any porosity. The interface between the platinum bottom electrode and ATN film was clear, suggesting that there is no extensive reaction between the two. No contrast difference for the natrotantite phase was observed in the bright field images and only the electron diffraction pattern of the pseudocubic perovskite ATN phase was seen throughout the TEM sample.

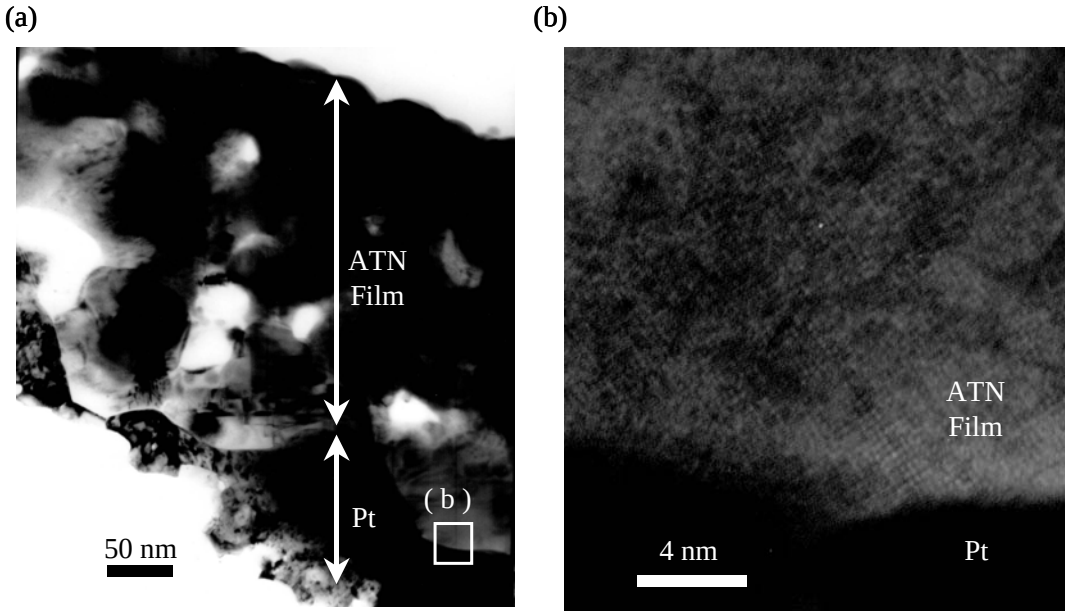


Figure **4.12**: Bright field TEM images of the ~450 nm thick two-phase ATN film (sample two in Table 4.1). (a) Cross section image at 120 k magnification (b) High resolution image of platinum-ATN film interface where lattice fringes observed for the ATN film. (Courtesy of Dr. I. M. Reaney)

Figure **4.13** shows the <001> zone axis of the perovskite electron diffraction pattern of the film. In addition to the fundamental diffraction spots, ½{hk0} type weak superlattice spots and diffuse scattering in the <100> and <010> directions were observed. There were also ½{h k l} type weak superlattice spots in the <110> zone axis diffraction pattern.

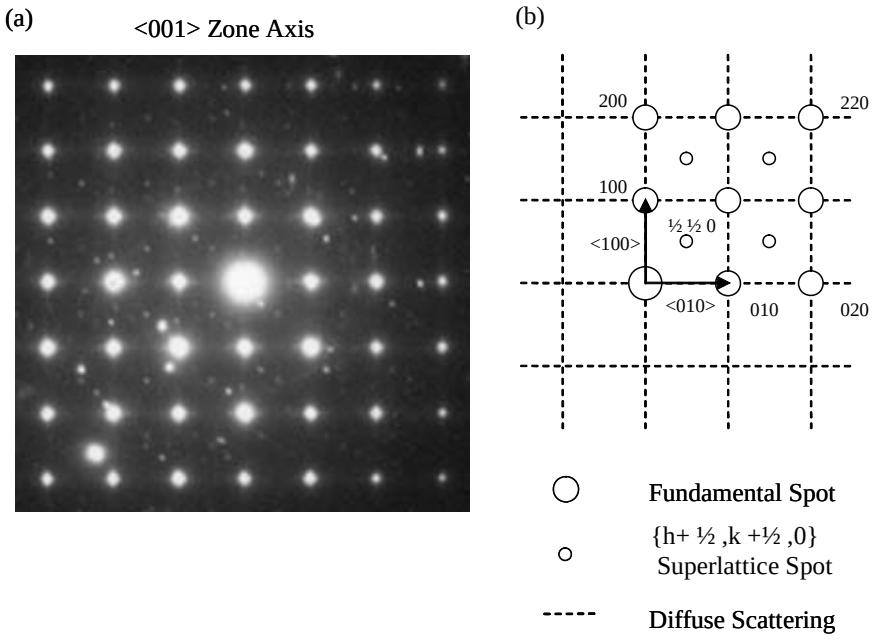


Figure **4.13**: Electron diffraction pattern of a ~450 nm thick two-phase film (sample two in Table 4.1). (a) <001> Zone axis perovskite diffraction pattern taken at 200 kV (b) Schematic explaining main features of the diffraction pattern. The remaining spots could be associated selected area aperture overlaping with different grains. (Courtesy of Dr. I. M. Reaney)

Chemical ordering, antiparallel cation displacements, tilting of oxygen octahedra and double diffraction can lead to superlattice spots in an electron diffraction pattern.[12, 13, 14, 15] Chemical ordering is expected when there is a large size and/or valence difference between the ions on the same sublattice.[16] The $Ta^{5+}$ and $Nb^{5+}$ ions were not expected to order on the B site due to their similarity in size (radius of 0.64 Å).[17] It is possible that some of the superlattice spots came from oxygen octahedral tilting consistent with the $M_3$ phase having $a^-b^0c^+$ tilts in Glazer notation.[18, 19] The $M_3$ phase is reported to be stable at temperatures above 50 °C in bulk $Ag(Ta_{0.5}Nb_{0.5})O_3$.[20] Such tilting could have been

observed here either due to a shift in the transition temperature of the films or electron beam heating of the sample. Antiphase tilting (successive octahedral tilting in opposite directions) along the a axis and in-phase tilting (successive octahedral tilting in the same direction) along the c axis observed in the $M_3$ phase doubles the original unit cell and forms a superlattice with a periodicity of $2a_0x2b_0x2c_0$.[21] Therefore, it was possible to observe superlattice spots at half integer reflections. In addition, antiphase tilting along the a axis would produce odd-odd-odd superlattice spots with $h \neq l$, like ½{113} and in-phase tilting in c axis would produce odd-odd-even superlattice spots with $h \neq k$, like ½{130}.[22] However, it would be preferable if additional TEM could be done to confirm these results.

Short range chemical ordering, low frequency optic phonons, order-disorder dipoles, or local breaks of symmetry related to uncertainty in the position of the A site ion could lead to the diffuse scattering.[18, 23, 24, 25, 26] Chemical ordering was not expected due to the similar size of $Ta^{5+}$ and $Nb^{5+}$ ions. A more complete TEM investigation would be necessary to figure out the origin of the diffuse scattering observed in the <100> and <010> directions, but it should be pointed out that in materials like $BaTiO_3$ and $KNbO_3$, there is still uncertainity regarding the origin of diffuse scattering.[23]

### 4.2.2 Effect of Low Temperature Heat Treatment Steps on Crystal Structure Formation for $Ag(Ta_{0.5}Nb_{0.5})O_3$ Thin Films Deposited on (111)Pt/Ti/$SiO_2$/(100)Si Substrates:

Because phase-pure perovskite and natrotantite ATN films were desired, a series of experiments were undertaken to determine the conditions under which these two phases form. In order to examine nucleation and growth of the new phase at low temperatures, ~30 nm ATN films were spun using a 0.2 M solution and heated on a hot plate for 2 minutes at temperatures from 140 °C to 300 °C. At this point, the films were still amorphous to the detection limit of x-ray diffraction. The films were then crystallized at 550 °C with a heating rate of 100 °C/s using a rapid thermal anneal furnace (RTP600S model). XRD patterns of the films (Figure **4.14** where the patterns are offset for clarity) show only the natrotantite ($Ag_2(Ta_{0.5}Nb_{0.5})_4O_{11}$) phase for all of the films. Based on the maximum in the XRD intensities, the natrotantite phase is believed to nucleate most effectively around 175 °C. In addition, the shape of the natrotantite 0 0 12 peak is unusually broad but origin of the diffusiveness is not known for sure.

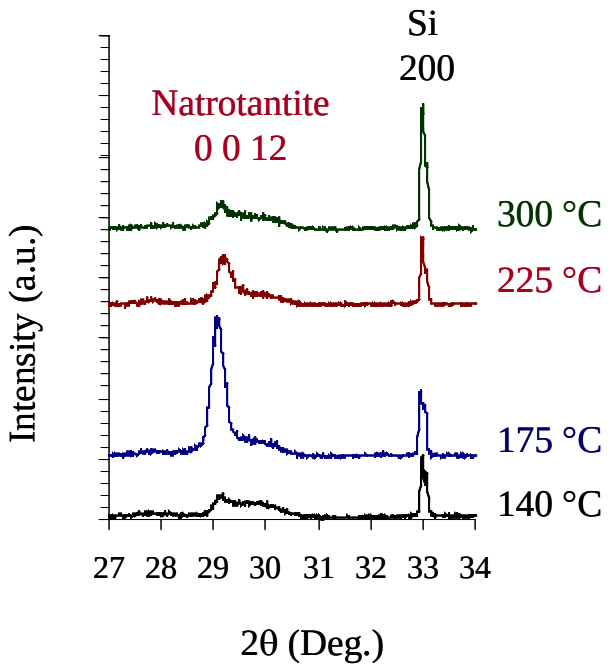


Figure **4.14**: XRD patterns of ~30 nm thick ATN films heat treated for 2 minutes at temperatures from 140 °C to 300 °C and crystallized at 550 °C for a minute in an $O_2$ ambient.

### 4.2.3 Effect of Heating Rates on Crystal Structure Formation for $Ag(Ta_{0.5}Nb_{0.5})O_3$ Thin Films Deposited on (111)Pt/Ti/$SiO_2$/(100)Si Substrates:

It has been reported in many Pb-based perovskite films that formation of a fluorite second phase can be minimized by heating rapidly through the intermediate temperature regime.[2, 5] In order to check the effect of heating rate on crystallization of ATN films, two films thicknesses were investigated at each rate. The ATN films were prepared from a 0.2 M solution. The spun layers were dried at room temperature for 10 minutes to avoid nucleation. The films were then crystallized at 550 °C with heating rates of 5 or 100 °C/s.

XRD profiles of ~60 and 120 nm films (Figure **4.15**) show that there was a strong heating rate dependence for the new phase formation. The fast heating rate, 100 °C/s, drastically reduced formation of the natrotantite phase and favored the perovskite phase for both 60 and 120 nm thick films.

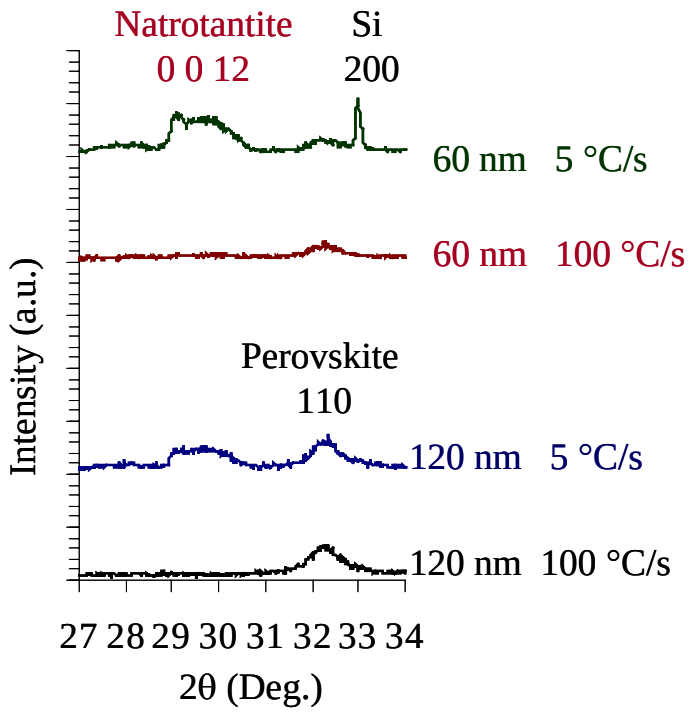


Figure **4.15**: XRD patterns of ATN films (having thicknesses of 60 and 120 nm) crystallized at 550 °C for a minute in an $O_2$ ambient with 5 or 100 °C/s heating rates.

### 4.2.4 Thickness Dependence of the $Ag_2(Ta_{0.5}Nb_{0.5})_4O_{11}$ Phase Formation for $Ag(Ta_{0.5}Nb_{0.5})O_3$ Thin Films Deposited on (111)Pt/Ti/$SiO_2$/(100)Si Substrates:

ATN films with different thicknesses were prepared from a 0.2 M solution; individual layers were heat treated at 175 °C for 5 minutes. This procedure was repeated until the desired thickness was achieved. Then, the films were crystallized in a single step with a 100 °C/s heating rate to 550 °C for 1 minute in an $O_2$ ambient. XRD profiles of 120, 210, 270 and 330 nm thick films (See Figure **4.16** where the XRD patterns are offset for clarity), showed primarily the natrotantite phase in films up to 120 nm thickness. The pseudocubic perovskite phase was more prevalent in thicker films, based on XRD intensities. This suggested that the Pt interface favors natrotantite phase formation.

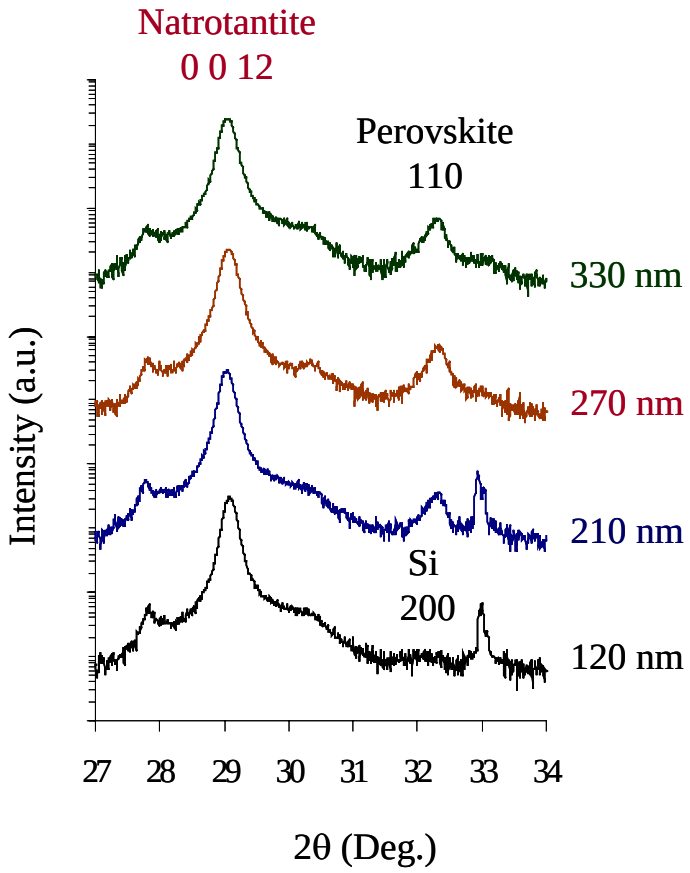


Figure **4.16**: XRD patterns of ATN films crystallized at 550 °C for 1 minute in an $O_2$ ambient showing the evolution of the perovskite phase with film thickness.

### 4.2.5 $Ag_2(Ta_{0.5}Nb_{0.5})_4O_{11}$ Natrotantite and Perovskite Phase Nucleation and Growth:

In order to determine how fast the two phases grew, a ~210 nm thick film was prepared by hot plate baking the first layer at 175 °C for 30 seconds to nucleate the natrotantite phase and heat treating the remaining 6 layers at 250 °C for 30 seconds to

remove the majority of the organics. The film was then crystallized at 550 °C with a heating rate of 100 °C/s for 1, 10, 60 or 300 seconds in an $O_2$ environment. Figure **4.17** shows the XRD patterns of the resulting films. No time dependence in the XRD intensity of the natrotantite phase was observed for the time range investigated, suggesting that the kinetics for the phase formation are quite rapid. On the other hand, the pseudocubic perovskite phase developed rather slowly at 550 °C. Kinetic models for the nucleation and growth rates of the two phases could not be developed from this data, because the volume fractions of the two phases could not be sensibly calculated from the XRD intensities due to strong diffraction intensities observed for the (00*l*) oriented natrotantite phase. An extensive TEM study would be necessary for this, and is beyond the focus of the present study.

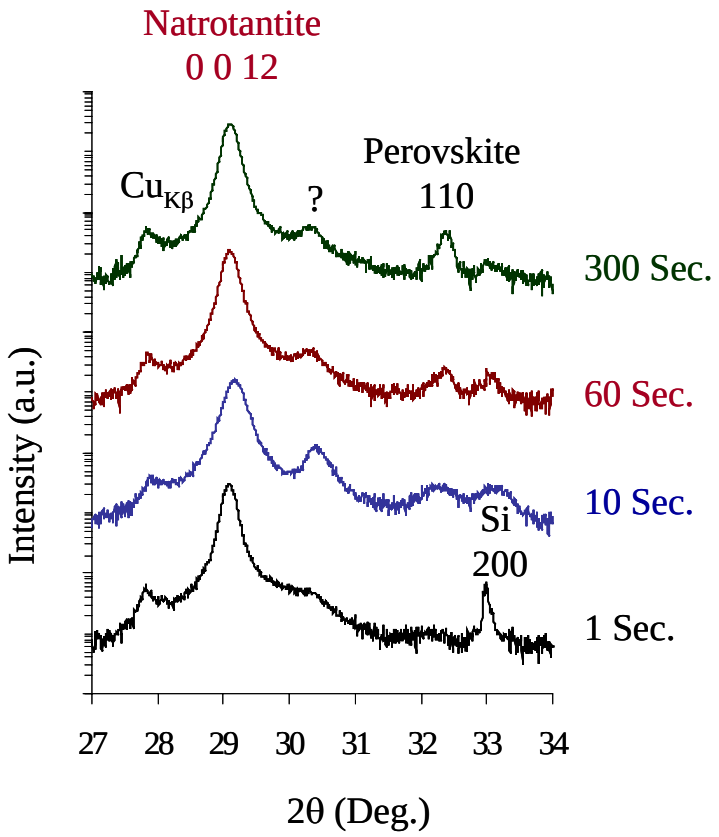


Figure **4.17**: XRD patterns of ~210 nm thick ATN films crystallized at 550 °C for different durations in an $O_2$ environment.

### 4.2.6 Use of Fast Heating Rate and High Crystallization Temperatures for Maximizing Perovskite Phase Formation:

It was shown that the natrotantite phase formation was favored by a low temperature pyrolysis step (around 175 °C) and slow heating rates (5 °C/s) to a crystallization temperature of 550 °C. In addition, the pseudocubic perovskite phase nucleation and growth was shown to be slow at 550 °C. Therefore, it was hypothesized

that it should be possible to maximize the volume fraction of pseudocubic perovskite phase by crystallizing films at higher crystallization temperatures using a fast heating rate of 100 °C/s. To test this, two films were heat treated as described in Table **4.2**. It is clear from Figure **4.18** that fast heating rates and high crystallization temperatures promoted the pseudocubic perovskite phase over the natrotantite phase (shown as Nat. in the figure). However, it did not completely eliminate the natrotantite phase. In addition, there was a new XRD peak at 36.4 ° for the 650 °C crystallized film, suggesting that a third phase might have been forming. A similar XRD patterns was observed for the films directly crystallized at 700 °C. Therefore, use of high crystallization temperatures with a fast heating rate did not result in phase pure pseudocubic perovskite films on Pt-coated Si substrates.

Table **4.2**: Heat treatment details and resulting phases of two ATN films

| Film Number | Thickness (nm) | Crystallization Conditions | Phases Present |
|---|---|---|---|
| 1 | 450 | 8 X 650 °C | Mostly perovskite, some natrotantite and a third phase |
| 2 | 330 | 11 X 175 °C and 1 X 550 °C | Mostly natrotantite and some perovskite |

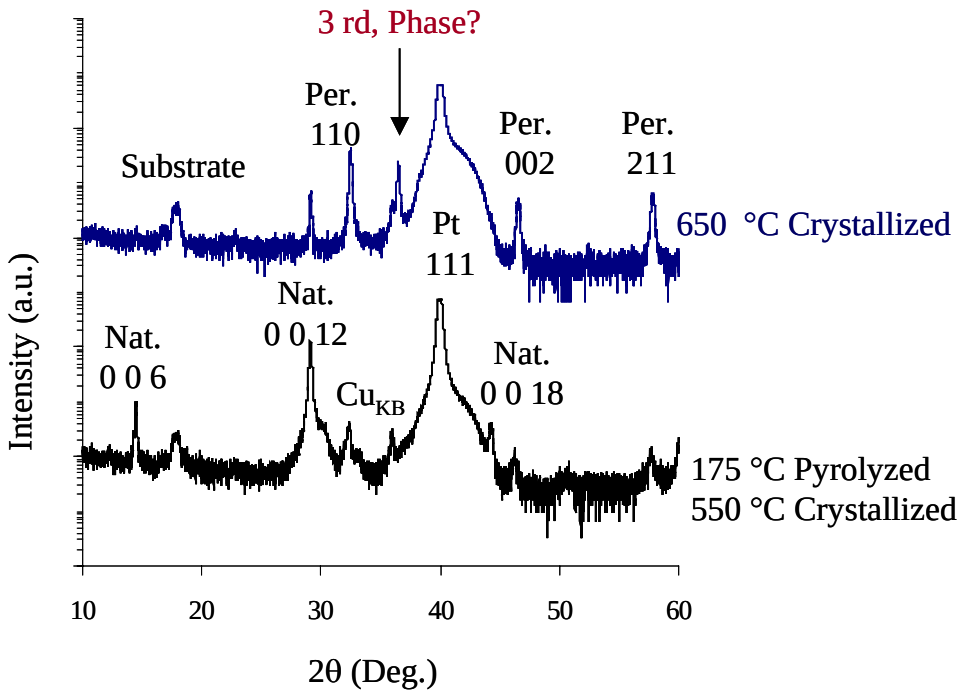


Figure **4.18**: XRD patterns of a ~450 nm thick ATN film crystallized directly at 650 °C and a ~330 nm thick ATN film pyrolyzed at 175 °C and crystallized at 550 °C.

### 4.2.7 Crystal Structure Formation of Silver Deficient Compositions:

In order to synthesize pure natrotantite phase films, silver deficient (relative to the perovskite phase) compositions were investigated. Solutions were prepared with $Ag_2(Ta_{0.5}Nb_{0.5})_4O_{11}$, $Ag_{0.8}(Ta_{0.5}Nb_{0.5})O_{2.9}$, $Ag_{0.85}(Ta_{0.5}Nb_{0.5})O_{2.925}$, and $Ag_{0.9}(Ta_{0.5}Nb_{0.5})O_{2.95}$ compositions (based on ionic compensation of silver deficiency). Films were processed using a 5 minute hot plate bake at 175 °C and a single 550 °C, 1 minute $O_2$ crystallization step. Figure **4.19** shows the ternary map, where the

compositions of the deposited films together with compositions of known binary and ternary compounds are marked.[27, 28]

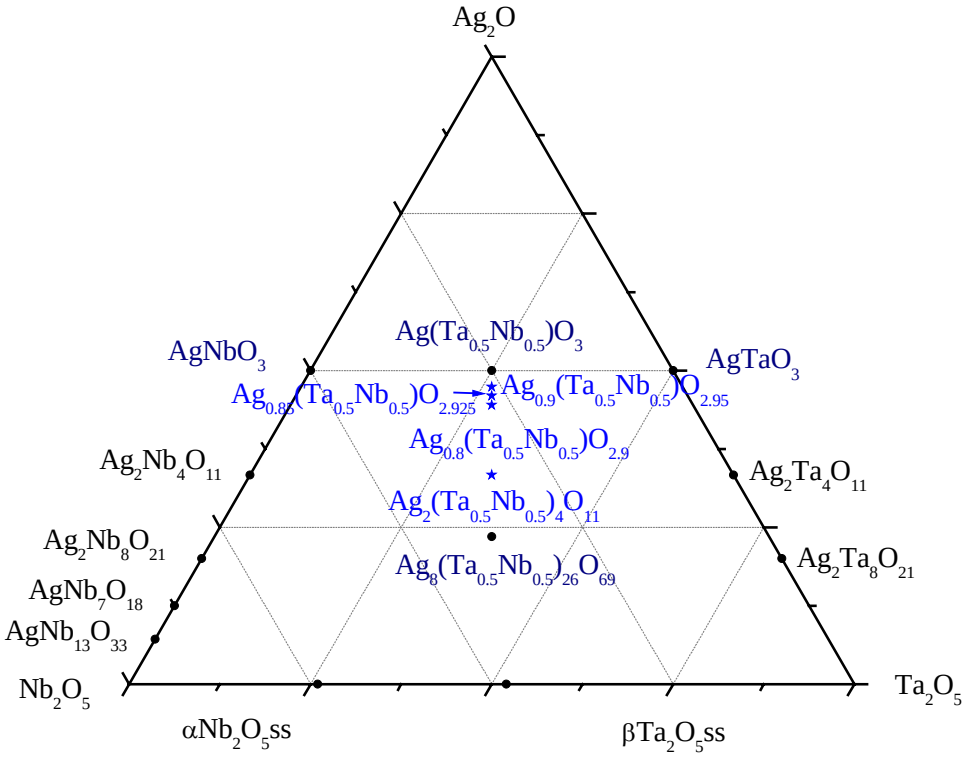


Figure **4.19**: Ternary map showing compositions of films having silver deficient compositions (relative to the perovskite phase having composition of $Ag(Ta_{0.5}Nb_{0.5})O_3$) deposited on (111)Pt/Ti/$SiO_2$ /(001)Si substrates (marked with stars) and compositions of reported binary and ternary bulk compounds and solid solutions (marked with circles). Assumption for the silver deficient composition is made based on that the silver deficiency is compensated ionicly.

Figure **4.20** shows XRD patterns of the films. The peaks are indexed either as the natrotantite phase (shown as Nat. in the figure) or pseudocubic perovskite phase. The XRD profile of the $Ag_2(Ta_{0.5}Nb_{0.5})_4O_{11}$ film (which should correspond to stoichiometric natrotantite) showed a good match to the simulated natrotantite XRD powder profile.

However, it did not show any preferred (00*l*) orientation. Increase in the silver content to $Ag_{0.8}(Ta_{0.5}Nb_{0.5})O_{2.9}$ did not increase the orientation level, but the observed XRD peaks could still be explained by the natrotantite structure. When the silver content was increased to $Ag_{0.85}(Ta_{0.5}Nb_{0.5})O_{2.925}$, strong natrotantite 00*l* family peaks were observed. Further increase in the silver content to $Ag_{0.9}(Ta_{0.5}Nb_{0.5})O_{2.95}$ produced a two phase mixture of pseudocubic perovskite phase (with broad peaks around 32, 46 and 57 degrees) and (00*l*) oriented natrotantite phase. Thus, excess silver content was required to observe a (00*l*) orientation for the natrotantite phase.

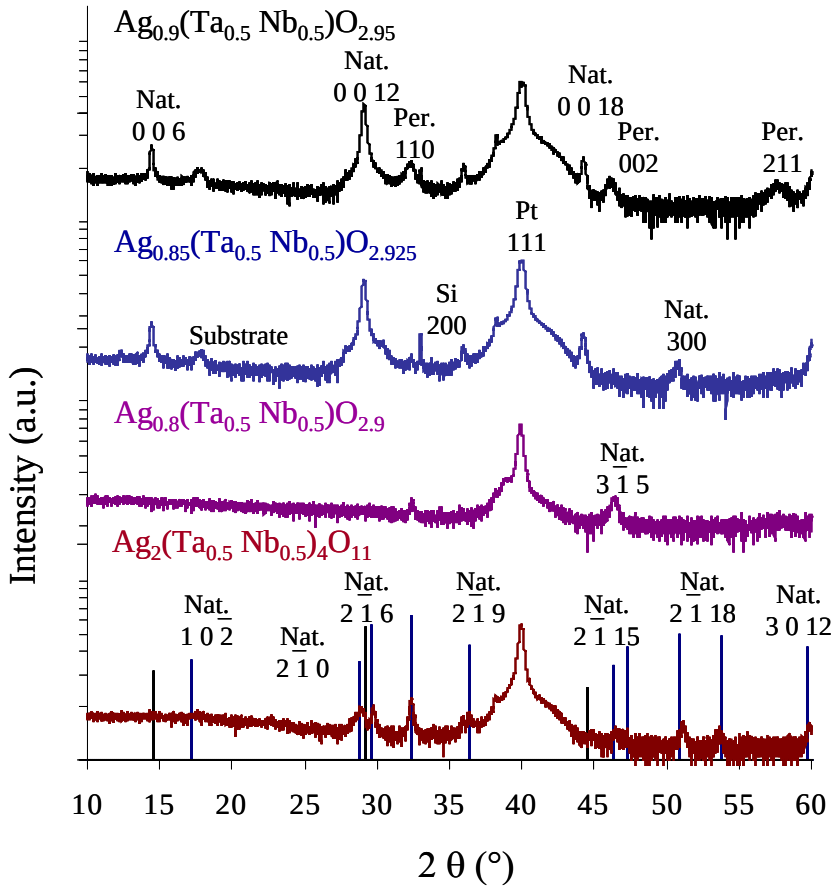


Figure **4.20**: XRD patterns of $Ag_2(Ta_{0.5}Nb_{0.5})_4O_{11}$, $Ag_{0.8}(Ta_{0.5}Nb_{0.5})O_{2.9}$, $Ag_{0.85}(Ta_{0.5}Nb_{0.5})O_{2.925}$, and $Ag_{0.9}(Ta_{0.5}Nb_{0.5})O_{2.95}$ films deposited on (111)Pt/Ti/$SiO_2$ /(001)Si substrates and prepared by hot plate baking at 175 °C for 5 minutes and undergoing a single $O_2$ crystallization at 550 °C for a minute.

### 4.2.8 Mechanism of Natrotantite Phase Formation:

It was hypothesized that the natrotantite phase formation was favored by the platinum surface, since the chemical solution used for deposition yielded a phase pure perovskite powder when heat treated at 800 °C for 30 minutes (using a heating rate of 10 °C/min.) under an $O_2$ ambient. In addition, TEM investigation of the first film described

in Table 4.1 showed that the natrotantite phase formed with some columnar grains, presumably starting at the platinum-ATN film interface and growing towards the top of the film.

In order to test the importance of a platinum surface, ~20 nm thick ATN films were deposited on both (111)Pt/Ti/$SiO_2$/(001)Si and $SiO_2$/(001)Si substrates by spinning 0.2 M solution at 4000 rpm. Both films were crystallized at 550 °C for a minute in an $O_2$ ambient with a heating rate of 100 °C/s. XRD profiles (Figure **4.21**) show clearly that the natrotatite phase forms only on the platinized silicon substrate.

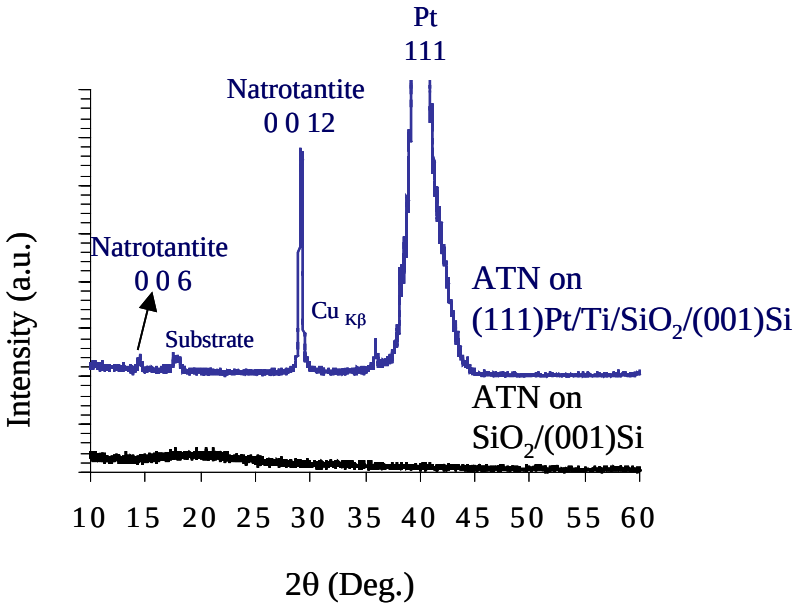


Figure **4.21**: XRD patterns of ~20 nm thick $Ag(Ta_{0.5}Nb_{0.5})O_3$ (ATN) films crystallized at 550 °C for 1 minute in $O_2$ on (111)Pt/Ti/$SiO_2$/(001)Si and $SiO_2$/(001)Si substrates.

Formation either of an intermetallic or an oxide layer at the platinum-film interface was reported to affect the orientation of $Pb(Zr_xTi_{1-x})O_3$ films deposited on

(111)Pt/Ti/$SiO_2$/(001)Si substrates.[7, 29, 30] Depending on both the heat treatment conditions and the composition of the deposited films, either a $Pt_{3-7}Pb$ intermetallic or a PbO layer formed at the platinum-film interface.[29] While (111) oriented perovskite phase was promoted when the $Pt_{3-7}Pb$ intermetallic layer was formed, (100) oriented perovskite was promoted when PbO was formed. This was attributed to the good lattice match between (111) perovskite and the (111) $Pt_{3-7}Pb$ planes and between (100) perovskite and the (001) PbO planes. In the ATN films, neither TEM nor XRD investigations suggested formation of any intermetallic or discrete oxide compounds at the platinum-film interface. So, an attempt was made to identify a structural match between (111) Pt and (00l) natrotantite that could explain the observed orientation in many of the films.

The atomic distances of $Ag^+$ cations lying close to (001) plane of natrotantite phase and Pt atoms belonging to Pt (111) plane were investigated for a potential match. It was found that $Ag^+$ cations lying in [010] and [100] directions were 6.21 Å apart. The closest matching interatomic distances were found to be 5.54 Å for the Pt atoms lying in $[\bar{1}01]$ and $[\bar{1}10]$ directions. This mismatch was within 12 %. Figure **4.22** illustrates a possible structure match based on this. The (00*1*) natrotantite plane would be parallel to the (111) platinum plane. The [010] natrotantite direction would be parallel to the $[\bar{1}01]$ platinum direction. The metallic radius of Ag (1.444 Å) is ~4% larger than that of Pt (1.38 Å). It is possible that a thin layer of Ag first forms on the Pt surfaces in Ag-excess compositions, decreasing the lattice mismatch to 7.5 % and favoring the (00*l*) orientation. In any event, high resolution TEM would be required to establish any local epitaxial arrangement in these fiber-textured samples.

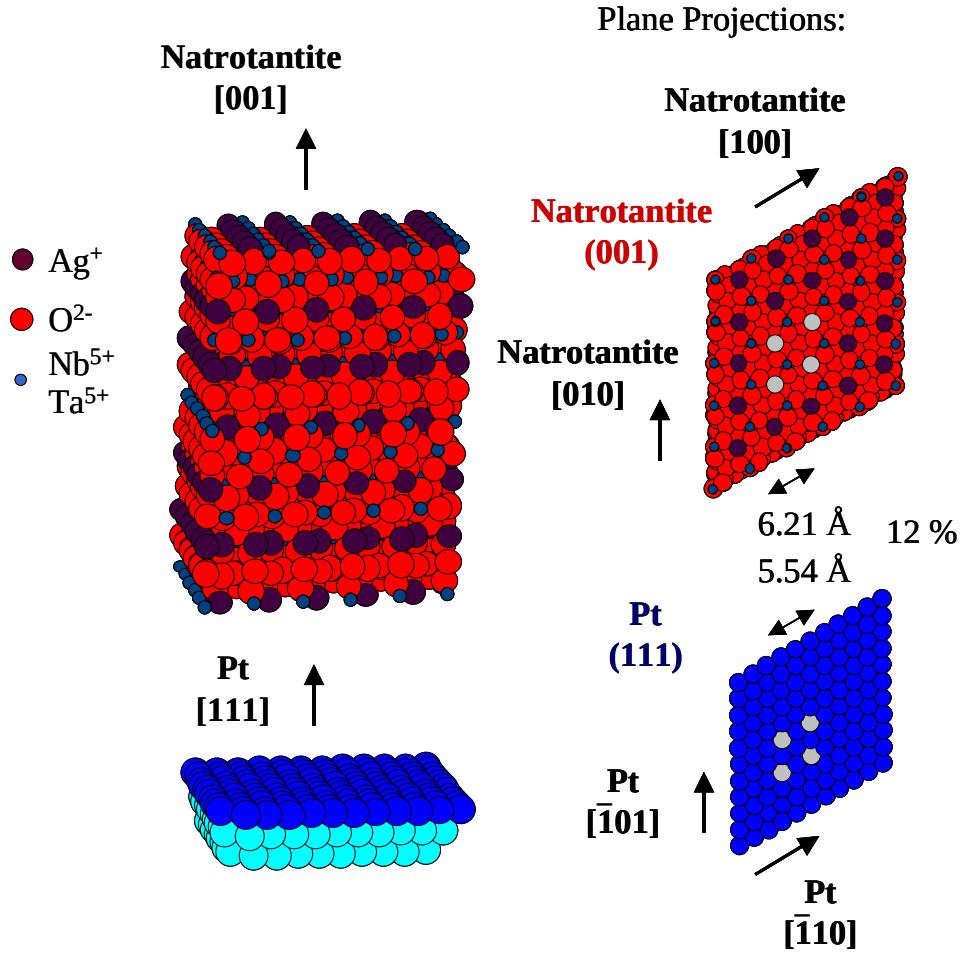


Figure 4.22: Possible orientation relationship between (00*l*) oriented $Ag_2(Ta_{0.5}Nb_{0.5})_4O_{11}$ natrotantite phase (ATNO) and (111) oriented platinum.

### 4.2.9 Crystal Structure Development of ATN Films Deposited on (111)Pt/Ti/$SiO_2$/(001)Si Substrates Based on Heat Treatment Conditions:

Crystal structure formation of the ATN films deposited on (111)Pt/Ti/$SiO_2$/(001)Si substrates involved formation of two competing phases: (00*l*)

oriented natrotantite and a randomly oriented pseudocubic perovskite phase. The natrotantite phase is favored by heat treatment at low temperatures (around 175 °C) at the platinum-film interface and grows quickly at 550 °C. The pseudocubic perovskite phase nucleates and grows randomly throughout the film at crystallization temperatures above 550 °C. Therefore, it was possible to control formation of the two phases to some extent by controlling the heat treatment conditions. One possible scenario that would be consistent with the observations is shown in Figure **4.23**. When the heat treatment steps involved low temperatures steps or a slow heating rate (5 °C/s), natrotantite phase formation was promoted. As the natrotantite phase forms more silver precipitation was observed. When the low temperature steps were minimized by using a fast heating rate (100 °C/s) and when higher crystallization temperatures ($T \geq 550$ °C) were used, pseudocubic perovskite phase formation was promoted over natrotantite phase formation (together with less silver precipitation). Another scenario would be phase separation of the gel into silver rich and silver deficient regions during low temperature heat treatment steps and formation of natrotantite in silver deficient regions. Complete removal of the natrotantite phase was not possible by using the fast heating rate. In addition, a third phase formation was observed when crystallization temperatures of 650 and 700 °C were used.

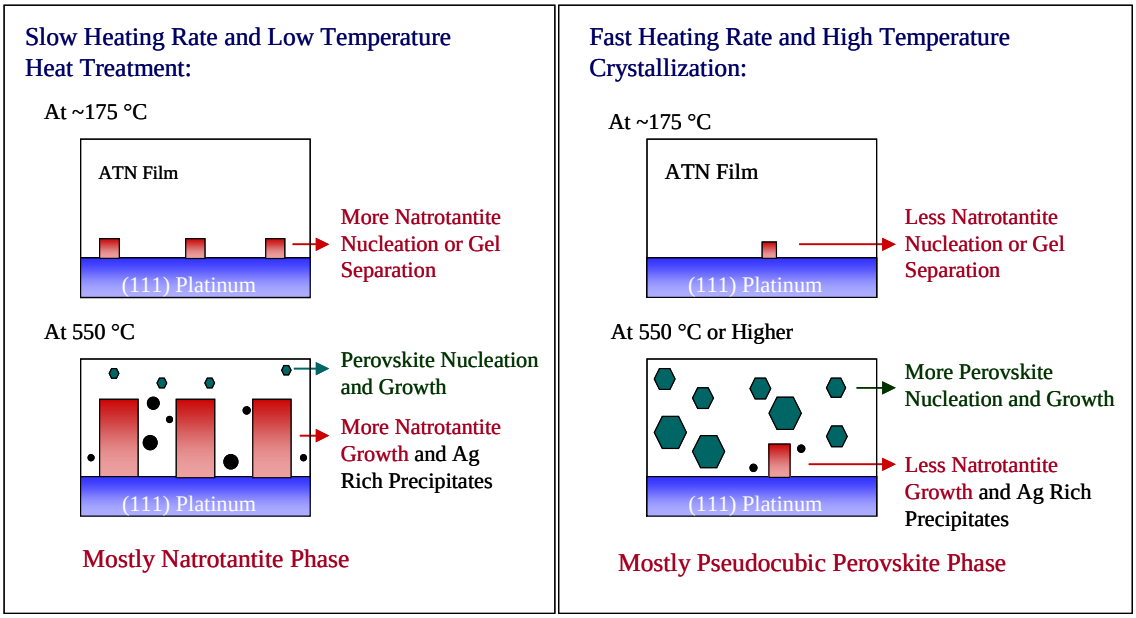


Figure **4.23**: Schematic showing a possible phase formation scheme in $Ag(Ta_{0.5}Nb_{0.5})O_3$ films deposited on (111)Pt/Ti/$SiO_2$/(001)Si substrates.

## 4.3 Dielectric Properties of $Ag(Ta_{0.5}Nb_{0.5})O_3$ and Silver Deficient Films Deposited on (111)Pt/Ti/$SiO_2$/(001)Si Substrates:

The dielectric constant and loss of the $Ag(Ta_{0.5}Nb_{0.5})O_3$ films were measured based on parallel plate capacitor structures between 1 and 100 kHz using sputtered platinum top electrodes. Figure **4.24** shows the dielectric constant, $\varepsilon_r$, and loss, tanδ, of mixed phase ATN films as a function of crystallization temperature. The dielectric constants of the films were lower than bulk ATN ceramics ($\varepsilon_r$ = 410) but remained fairly constant within the measurement frequency range. The loss decreased with increasing frequency, suggesting a space charge component, and stayed low over the measurement

frequency range. At 100 kHz, $\varepsilon_1$ and tan $\delta$ are 200±20 and 0.006±0.002 for the 550 °C crystallized film, 270±25 and 0.004±0.002 for the 600 °C crystallized film, 220±20 and 0.002±0.001 for the 750 °C crystallized film.

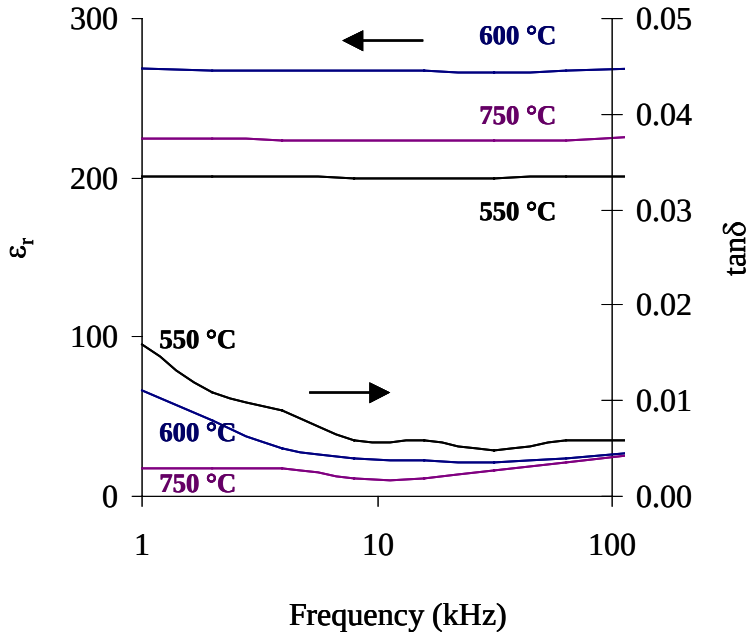


Figure **4.24**: Dielectric constant and loss of mixed phase $Ag(Ta_{0.5}Nb_{0.5})O_3$ films as a function of crystallization temperature over the frequency range from 1 to 100 kHz.

When the dielectric properties of natrotantite and silver deficient films were measured (Table **4.3**), the permittivity values were lower and and loss values were a little higher than the two phase $Ag(Ta_{0.5}Nb_{0.5})O_3$ films.

Table **4.3**: Dielectric constant and loss of the films having silver deficient compositions compared to the perovskite composition of $Ag(Ta_{0.5}Nb_{0.5})O_3$ at 100 kHz

| Film Composition | $\varepsilon_r$ | tanδ |
|---|---|---|
| $Ag_{0.9}(Ta_{0.5}Nb_{0.5})O_{2.95}$ | 130±15 | 0.008±0.002 |
| $Ag_{0.85}(Ta_{0.5}Nb_{0.5})O_{2.925}$ | 115±10 | 0.008±0.002 |
| $Ag_{0.8}(Ta_{0.5}Nb_{0.5})O_{2.9}$ | 135±15 | 0.008±0.002 |
| $Ag_2(Ta_{0.5}Nb_{0.5})_4O_{11}$ | 70±10 | 0.008±0.003 |

The reason for the lower dielectric constants of the two phase $Ag(Ta_{0.5}Nb_{0.5})O_3$ films compared to bulk ceramic values was thought to be related to the presence of the natrotantite phase. Assuming that a limited amount of (00*l*) oriented natrotantite phase formed at the platinum-film interface and that the pseudocubic perovskite phase was forming on top of the natrotantite phase (Figure **4.25**), then the dielectric constant could be modeled as two dielectric layers in series. Then, the overall dielectric constant could be calculated in terms of dielectric constants and volume fractions of two layers (Equation **4.7**).[31] In this model, the phase having a lower dielectric constant is weighted more heavily in the overall dielectric response than the high permittivity phase.

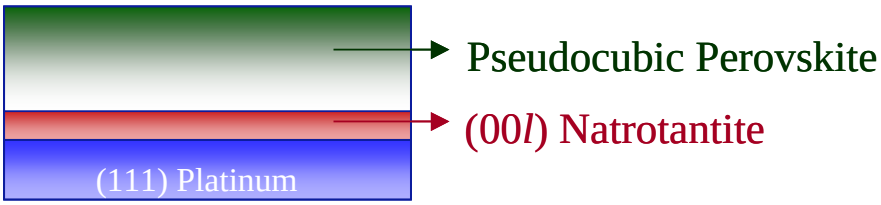


Figure **4.25**: Schematic showing distribution of natrotantite and perovskite phase in mixed phase films on Pt-coated Si substrate.

$$\frac{1}{\varepsilon_t'} = \frac{\upsilon_1}{\varepsilon_1'} + \frac{\upsilon_2}{\varepsilon_2'} \qquad \text{(Equation 4.7)}$$

where:

$\varepsilon_t$: Overall Dielectric Constant

$\varepsilon_i$: Dielectric Constant of Phase i (i = 1, 2)

$\nu_i$: Volume Fraction of Phase i (i = 1, 2)

The model predicted 23 vol. % (00*l*) oriented natrotantite having a dielectric constant of 115 (observed for $Ag_{0.85}(Ta_{0.5}Nb_{0.5})O_{2.925}$ film) was enough to lower the overall dielectric constant from 410 to 260 (assuming no shift in the perovskite phase transition).

It is important to have temperature stable dielectric properties for tunable filters. The temperature dependence of the dielectric constant and loss shown for a two phase ATN film (~600 nm thick) crystallized at 550 °C at 100 kHz is shown in Figure **4.26**. The broad maxima and slightly decreasing permittivity above room temperature is consistent

with a shifted $M_2$– $M_3$ phase transition and having $M_3$ phase for the perovskite phase at or slightly above room temperature. The capacitance changed –5.8 % at 120 °C from its room temperature value at 100 kHz. The corresponding temperature coefficient of capacitance (TCC, calculated as in Equation **4.8**) was –0.11 %/°C.

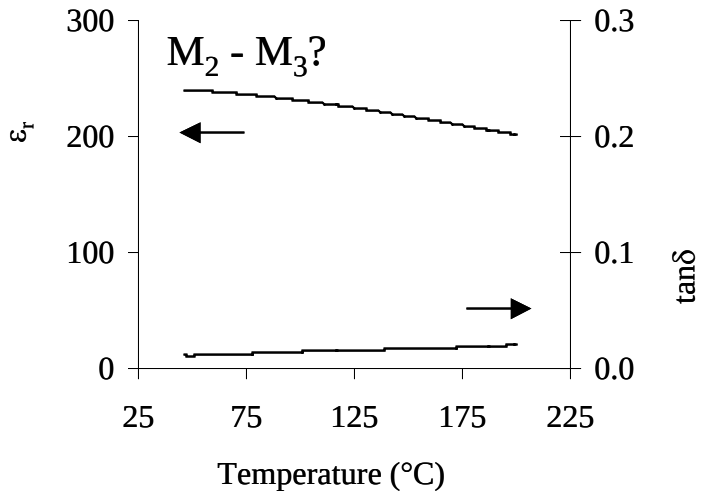


Figure **4.26**: Dielectric constant and loss of (~600 nm thick) two phase (mostly pseudocubic perovskite by XRD) ATN film crystallized at 550 °C as a function of temperature at 100 kHz.

$$TCC = \frac{1}{C}\frac{\partial C}{\partial T} \qquad \text{(Equation 4.8)}$$

The temperature dependent dielectric properties of a (00*l*) oriented natrotantite phase film was also checked (Figure **4.27**). The dielectric constant slightly decreased within the measured temperature range. The capacitance changed –8.8 % at 120 °C from

its room temperature value at 100 kHz. The corresponding temperature coefficient of capacitance (TCC) was –0.07 %/°C.

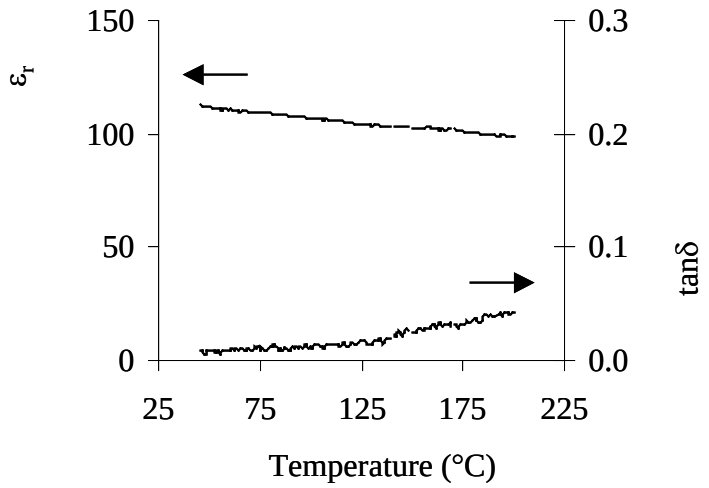


Figure **4.27**: Dielectric constant and loss of (~300 nm thick) (00*l*) oriented natrotantite film crystallized at 550 °C as a function of temperature at 100 kHz.

### 4.4 Conclusions:

$Ag(Ta_{0.5}Nb_{0.5})O_3$ films deposited on the (111)Pt/Ti/$SiO_2$/(001)Si substrates developed two phase mixtures of randomly oriented pseudocubic perovskite and a new phase that is a (00*l*) oriented natrotantite with a composition near $Ag_2(Ta_{0.5}Nb_{0.5})_4O_{11}$. Transmission electron microscope investigation of the natrotantite phase film suggested that the new phase was silver deficient compared to the perovskite composition. Silver-rich precipitates were also observed. ATN films with less natrotantite phase were mostly

a randomly oriented pseudocubic perovskite phase. The platinum–ATN film interface was clear of any reaction.

The phase development of the ATN films was found to be strongly dependent on the heat treatment steps. While the pseudocubic perovskite phase formation was favored by use of a fast heating rate (100 °C/s) to crystallization temperatures of 550 °C or higher, the natrotantite phase formation was found to be favored by a low temperature heat treatment step (~175 °C) and low heating rates (5 °C/s) to a crystallization temperatures of 550 °C. Although it was possible to affect the extent of these two phases by controlling heat treatment steps, it was not possible to eliminate the natrotantite phase formation completely on Pt coated Si substrates.

The thickness of the deposited films also affected the phase formation of $Ag(Ta_{0.5}Nb_{0.5})O_3$ films. While ATN films having thicknesses lower than ~120 nm showed only (*00l*) oriented natrotantite phase by XRD, thicker ATN films developed two phase mixtures. In addition, growth of the natrotantite phase was found to be much faster than nucleation and growth of the pseudocubic perovskite phase at 550 °C. The natrotantite phase was favored by low temperatures (e.g. 175 °C) near the platinum-film interface, and grew quickly at 550 °C. The pseudocubic perovskite phase nucleated and grew randomly throughout the film at crystallization temperatures higher than 550 °C. Phase pure (00*l*) oriented natrotantite films were only achieved for thicker films (~300 nm thick) when a solution having a composition of $Ag_{0.85}(Ta_{0.5}Nb_{0.5})O_3$ was used for the deposition. The $Ag_{0.85}(Ta_{0.5}Nb_{0.5})O_3$ composition is silver rich compared to the expected

natrotantite composition of $Ag_2(Ta_{0.5}Nb_{0.5})_4O_{11}$. Excess silver was correlated with strong (00*l*) natrotantite orientation.

The atomic distances of $Ag^+$ cations lying close to (001) plane of natrotantite phase and Pt atoms belonging to Pt (111) plane were investigated for a potential match. It was found that $Ag^+$ cations lying in [010] and [100] directions were 6.21 Å apart. The closest matching interatomic distances were found to be 5.54 Å for the Pt atoms lying in $[\bar{1}01]$ and $[\bar{1}10]$ directions. This mismatch was within 11 %. The (00*1*) natrotantite plane would be parallel to the (111) platinum plane. The [010] natrotantite direction would be parallel to $[\bar{1}01]$ platinum direction.

The dielectric constants of the two phase ATN films were lower than the bulk dielectric constant of 410. At 100 kHz, $\varepsilon_r$ and tan $\delta$ were 200±20 and 0.006±0.002 for the 550 °C crystallized film, 270±25 and 0.004±0.002 for the 600 °C crystallized film, 220±20 and 0.002±0.001 for the 750 °C crystallized film.

Natrotantite phase formation was suspected as the main reason for the lower dielectric constants for two phase ATN films. It was found that all silver deficient compositions (relative to the perovskite composition) having mainly the natrotantite phase had lower dielectric constants than ATN films having perovskite batch compositions. The dielectric constants and losses of the silver deficient compositions ranged from 70 to 135 and 0.008±0.002 respectively.

## 4.5 References:

[1] R.W. Schwartz, "Chemical solution deposition of perovskite thin films," *Chemistry of Materials*, **9** [11] 2325-2340 (1997).

[2] S.Y. Chen and I. W. Chen, "Temperature-time-texture transition of $Pb(Zr_{1-x}Ti_x)O_3$ thin films: heat treatment and compositional effects," *Journal of the American Ceramic Society*, **77** [9] 2337-2344 (1994).

[3] M. Ohring, *Materials Science of Thin Films*, Academic Press Inc., San Diego, CA, (1992).

[4] S. Y. Chen and I. W. Chen, "Texture development, microstructure evolution, and crystallization of chemically derived PZT thin films," *Journal of the American Ceramic Society*, **81** [1] 97-105 (1998).

[5] I. M. Reaney, A. Glazounov, F. Chu, A. Bell and N. Setter, "TEM of antiferroelectric-ferroelectric phase boundary in $(Pb_{1-x}Ba_x)(Zr_{1-x}Ti_x)O_3$ solid solution," *British Ceramic Transactions*, **96** [6] 217-224 (1997).

[6] I. M. Reaney, K. Brooks, R. Klissurska, C. Pawlaczyk and N. Setter, "Use of transmission electron microscopy for the characterization of rapid thermally annealed solgel lead-zirconate-titanate films," *Journal of the American Ceramic Society*, **77** [5] 1209-1216 (1994).

[7] Z. Zhou, I. M. Reaney, D. Hind, S. J. Milne, A. P. Brown and R. Brydson, "Microstructural evolution during pyrolysis of triol based sol-gel single layer $Pb(Zr_{0.53}Ti_{0.47})O_3$ thin films," *Journal of Materials Research*, **17** [8] 2066-2074 (2002).

[8] T. S. Ercit, F. C. Hawthorne and P. Cerny, "The crystal structure of synthetic natrotantite," *Bulletin de Mineralogie*, **108** 541–549 (1985).

[9] Personal Communications with D. I. Woodward and I. M. Reaney, Department of Engineering Materials, University of Sheffield, Sheffield S1 3JD, U.K

[10] http://pro.wanadoo.fr/carine.crystallography/

[11] B. D. Cullity and S. R. Stock, *Elements of X-Ray Diffraction*, Prentice Hall, Upper Saddle River, New Jersey, 2001.

[12] D. B. Williams and C. B. Carter, *Transmission Electron Microscopy*, Plenum Press, New York, N.Y., 1996.

[13] J. Ricote, D. L. Corker, R. W. Whatmore, S. A. Impey, A. M. Glazer, J. Dec and K. Roleder, "A TEM and neutron diffraction study of the local structure in the rhombohedral phase of lead zirconate titanate," *Journal of Physics: Condensed Matter*, **21** 4456-4462 (1986).

[14] H. Zheng, I. M. Reaney and W. E. Lee, "Effects of octahedral tilting on the piezoelectric properties of strontium/barium/niobium-doped soft lead zirconate titanate ceramics," *Journal of the American Ceramic Society*, **85** [9] 2337-2344 (1986).

[15] I. M. Reaney, A. Glazounov, F. Chu, A. Bell and N. Setter, "TEM of antiferroelectric-ferroelectric phase boundary in $(Pb_{1-x}Ba_x)(Zr_{1-x}Ti_x)O_3$ solid solution," *British Ceramic Transactions*, **96** [6] 217-224 (1997).

[16] C. A. Randall, D. J. Barber, R. W. Whatmore and P. Groves, "A TEM study of ordering in the perovskite, $Pb(Sc_{0.5}Ta_{0.5})O_3$," *Journal of Materials Science*, **21** [12] 4456-4462 (1986).

[17] R. D. Shannon and C. T. Prewitt, "Effective ionic radii in oxides and florides," *Acta Crystallographica Section B. Structural Crystallography and Crystal Chemistry*, **25** 925–934 (1969).

[18] Personal Communication with I. M. Reaney, Department of Engineering Materials, University of Sheffield, Sheffield S1 3JD, U.K.

[19] J. Petzelt, S. Kamba, E. Buixaderas, V. Bovtun, Z. Zikmund, A. Kania, V. Koukal, J. Pokorny, J. Polivka, V. Pashkov, G. Komandin and A. Volkov, "Infrared and microwave dielectric response of the disordered antiferroelectric $Ag(Ta,Nb)O_3$ system," *Ferroelectrics*, **223** 235-246 (1999).

[20] M. Pawelczyk, "Phase transitions in $AgTa_xNb_{1-x}O_3$ solid solutions," *Phase Transitions Part A*, **8** [4] 273 - 292 (1987).

[21] A. M. Glazer, "The classification of tilted octahedra in perovskites," *Acta Crystallographica Section B. Structural Crystallography and Crystal Chemistry*, **28** 3384-3392 (1972).

[22] A. M. Glazer, "Simple ways of determining perovskite structure," *Acta Crystallographica Section A.Crystal Physics Diffraction Theoretical and General Crystallography*, **31** 756–762 (1975).

[23] R. Comes, L. Lambert and A. Guiner, "The chain structure of $BaTiO_3$ and $KNbO_3$," *Solid State Communications*, **6** [10] 715-719 (1968).

[24] N. Menguy, C. Caranoni, B. Hilczer, K. Roleder, J. Dec, "Transmission electron microscopy studies of $Pb(Zr_{0.99}Ti_{0.01})O_3$ single crystals," *Journal of Physics and Chemistry of Solids*, **60** 625–629 (1999).

[25] C.A. Randall, *A Transmission Electron Microscope Study of Normal and Relaxor Perovskite Ferroelectric Materials*, Ph. D. Thesis in Experimental Physics, University of Essex, Colchester, U.K., 1987.

[26] J. Harada, M. Tanaka and G. Honjo, "Thermal diffuse streak in electron diffraction and low frequency transverse optic lattice waves of barrium titanate," *Journal of the Pyhsical Soceity of Japan*, **21** [5] 968-972 (1966).

[27] G. P. Mohanty, L. J. Fiegel, and J. H. Healy, "$Nb_2O_5$ – $Ta_2O_5$ system," *Journal of Physical Chemistry*, **68** [1] 209 (1964).

[28] Powder Diffraction Files: 89-7738, 51-0374, 21-1344, 21-1345, 22-473, 21-1083, 21-1084, 21-1085, 21-1086, 22-471. International Center for Diffraction Data, Newtown Square, PA, USA.

[29] Z. Huang, Q. Zhang and R. W. Whatmore, "Structural development in early stages of annealing of sol-gel prepared lead zirconate titanate thin films," *Journal of Applied Physics*, **86** 1662–1669 (1999).

[30] P. Muralt, T. Maeder, L. Sagalowicz, S. Hiboux, S. Scalese, D. Naumovic, R. G. Agostino, N. Xantopoulos, H. J. Mathieu, L. Patthey and E. L. Bullock, "Texture control of $PbTiO_3$ and $Pb(Zr,Ti)O_3$ thin films with $TiO_2$ seeding," *Journal of Applied Physics*, **83** [7] 3835-3841 (1998).

[31] W. D. Kingery, H. K. Bowen, D. R. Uhlmann, *Introduction to Ceramics: Second Edition*, Wiley –Interscience Publication, New York, NY, (1976).

# Chapter 5

## $Ag(Ta_xNb_{1-x})O_3$ Thin Films on (001)$SrRuO_3$/(001)$LaAlO_3$ Substrates

### 5.1 Introduction:

In order to provide a higher driving force to promote formation of the perovskite crystal structure, a perovskite substrate having a good lattice match with the silver tantalate niobate films was needed for the deposition. A (001)$LaAlO_3$ (LAO) substrate with a pulsed laser deposited (001)$SrRuO_3$ (SRO) conductive perovskite oxide layer was chosen. $LaAlO_3$ has a distorted perovskite structure with lattice parameters of $a_0$ = 3.79 Å and $\alpha$ of 90.12° (ICDD 85-0848). Relaxed $SrRuO_3$, with a pseudocubic lattice parameter, $a_0$ = 3.93±0.01 Å has an extremely good lattice match to $Ag(Ta_{0.5}Nb_{0.5})O_3$ (ATN), $AgTaO_3$ (ATO) and $AgNbO_3$ (ANO) ceramics.[1] The room temperature lattice parameters of the silver compounds were reported to be a: 3.929 Å b: 3.926 Å c: 3.930 Å and β: 90.49° for ATN (ICDD 89-7738), a: 3.928 Å and α: 89.30° for ATO and a: 3.940 Å b: 3.914 Å c: 3.940 Å and β: 90.52° for ANO (ICDD 22-0471).[2] The conductive $SrRuO_3$ layer is also helpful in the preparation of parallel plate capacitor structures for dielectric property characterization.

## 5.2 Preparation of Epitaxial $Ag(Ta_xNb_{1-x})O_3$ Films:

Thin films of $Ag(Ta_{0.5}Nb_{0.5})O_3$ (ATN), $AgTaO_3$ (ATO) and $AgNbO_3$ (ANO) were deposited either on (001) $LaAlO_3$ substrates (MTI Corporation, Richmond, CA) or on $SrRuO_3$ coated (001) $LaAlO_3$ (Details of the pulsed laser deposition of $SrRuO_3$ layer can be found elsewhere.[1]) using chemical solution deposition (Figure 5.1). The 0.3 M solutions were spun at 1500 rpm for 30 seconds, pyrolyzed at 200 °C and subsequently at 450 °C for 20 sec. each. The layer was then crystallized under 10 slpm $O_2$ flow for a minute at a temperature between 450 °C and 800 °C for the ATN films and at 750 °C for the ATO and ANO films by using a rapid thermal anneal furnace (RTP600S model) with a heating rate of 100 °C/s. These steps were repeated 5 times to build up 300±30 nm thick films.

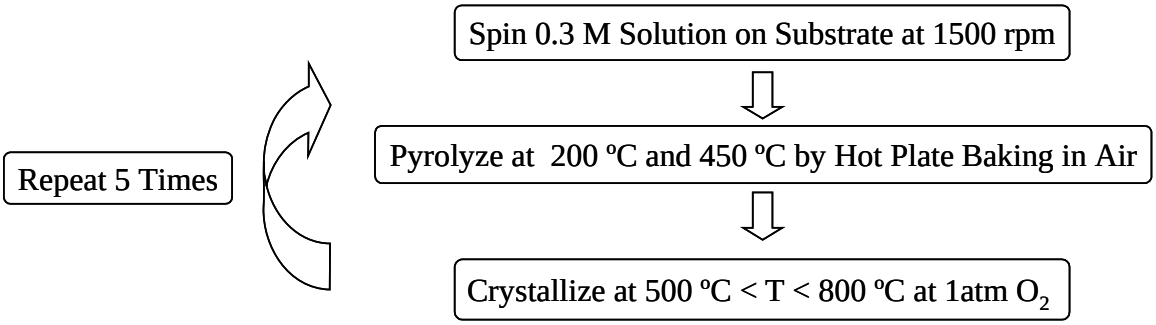


Figure 5.1: Spinning and heat treatments of $Ag(Ta_xNb_{1-x})O_3$ films deposited on (001)$LaAlO_3$ and on $SrRuO_3$ coated (001)$LaAlO_3$ substrates.

## 5.3 Crystal Structure Development of $Ag(Ta_xNb_{1-x})O_3$ Thin Films Deposited on (001) $LaAlO_3$ and (001)$SrRuO_3$/(001)$LaAlO_3$ Substrates:

XRD patterns of ATN films that were deposited directly on (001) $LaAlO_3$ substrates and then crystallized at 450 to 800 °C are shown in Figure 5.2 and Figure 5.3. The two figures were collected at two different generator settings to capture both strong and weak XRD peaks. The Miller indices of all of the perovskite peaks are given in terms of a pseudocubic unit cell. According to the figures, the ATN films showed only the pseudocubic perovskite crystal structure and were crystalline at temperatures as low as 500 °C. With an increase in crystallization temperature, the 00*l* ATN perovskite XRD peaks (Figure 5.2) became stronger, suggesting that the crystallinity of the films was also improving. Strong texture is apparent, suggesting that the substrate is, indeed, templating the crystallization in this case. Some misoriented material is apparent in Figure 5.3. It is likely that this could be minimized if the layer thicknesses used were reduced for each crystallization step. There was no reaction between the ATN and $LaAlO_3$ within the detection limits of XRD.

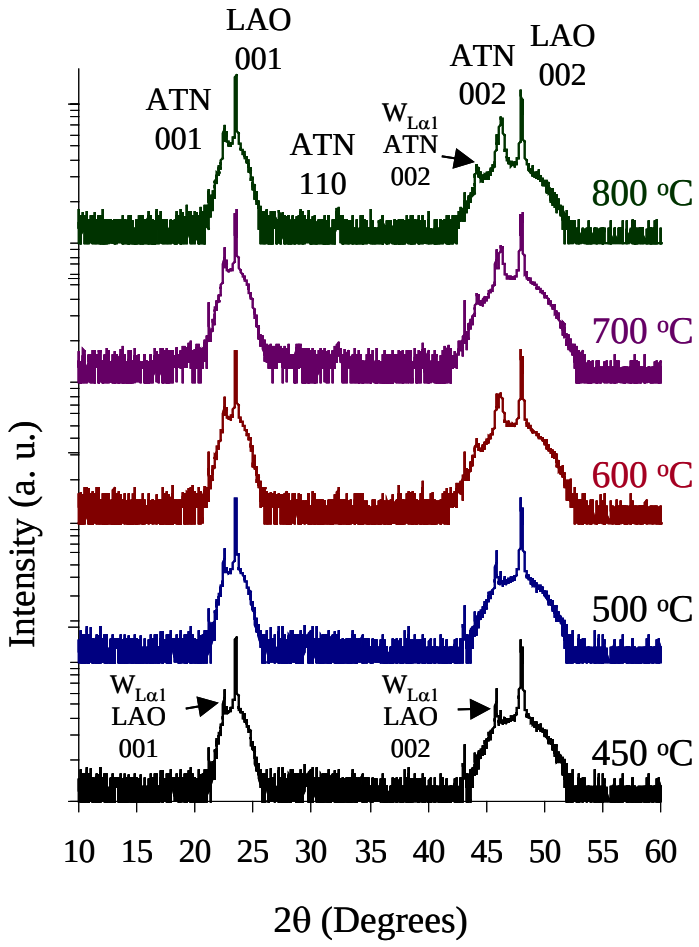


Figure **5.2**: XRD patterns of $Ag(Ta_{0.5}Nb_{0.5})O_3$ films on (001) $LaAlO_3$ substrates as a function of crystallization temperature. Patterns were taken at generator settings of 10 mA and 15 kV.

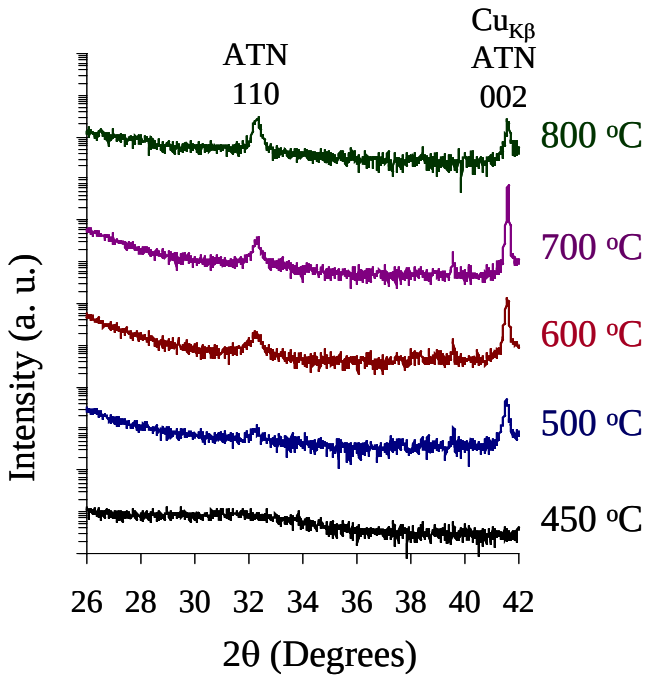


Figure **5.3**: XRD patterns of $Ag(Ta_{0.5}Nb_{0.5})O_3$ films on (001) $LaAlO_3$ substrates as a function of crystallization temperature. Patterns were taken at generator settings of 40 mA and 40 kV.

The out of plane lattice constants of the films can be calculated by using (00*l*) reflections of a 2θ scan and using a Nelson–Riley fit (Table **5.1**). The out of plane lattice constants were at the order of 3.92±0.01 Å. These values (within the error range) were similar to the room temperature lattice parameters of the ATN ceramics (a: 3.929 Å b: 3.926 Å c: 3.930 Å and β: 90.49°, ICDD 89-7738).

Table 5.1: Out of plane lattice constants of the $Ag(Ta_{0.5}Nb_{0.5})O_3$ films on (001) $LaAlO_3$ substrates

| Crystallization Temperature (°C) | Out of Plane Constant (Å) |
|---|---|
| 500 | 3.93±0.01 |
| 600 | 3.92±0.01 |
| 700 | 3.92±0.01 |
| 800 | 3.92±0.01 |

In order to confirm the improvement of the crystallinity of the ATN films with an increase in crystallization temperature, rocking curves of the 004 ATN peak were collected at generator settings of 30 mA and 35 kV with a step size of 0.01° and a step duration of 0.5 seconds. While the ATN film crystallized at 500 °C had a substantial mosaicity, with the full width at half maximum intensity (FWHM) of 1.35±0.02° (Table 5.2), the FWHM of the films decreased with an increase in crystallization temperature and was as low as 1.02±0.02° for the film crystallized at 800 °C.

Table 5.2: Full width at half maximum values from rocking curves of the 004 $Ag(Ta_{0.5}Nb_{0.5})O_3$ peak for films deposited on (001) $LaAlO_3$ substrates

| Crystallization Temperature (°C) | Full Width Half Maximum (°) |
|---|---|
| 500 | 1.35±0.02 |
| 600 | 1.20±0.02 |
| 700 | 1.07±0.02 |
| 800 | 1.02±0.02 |

As will be shown and discussed later (Figure 5.6), the ATN films that were deposited on (001)$LaAlO_3$ substrates were epitaxial.

Based on these results, ATN films were also deposited on (001)$SrRuO_3$/(001)$LaAlO_3$ substrates (Figure **5.4** and Figure **5.5**). The 00*l* XRD peaks of ATN and SRO are very close to each other and could not be observed separately. Again, very strong levels of texture are apparent. It was observed that the intensity of the 00*l* ATN reflections increased as the crystallization temperature increased, suggesting that the crystallinity of the ATN films was also improving. In addition to perovskite peaks, XRD peaks at ~28.1° and at ~35.2° were observed (Figure 5.5). While it was impossible to unambiguously identify the phase responsible for these peaks, $RuO_2$ (ICDD 71-2273) has peaks at similar positions, suggesting that there may be a limited reaction at the interface between the ATN film and $SrRuO_3$ (SRO). Based on the XRD peak intensities, the interfacial reaction was minimal at 500 °C, maximum at 600 °C and decreased with further increase in crystallization temperature.

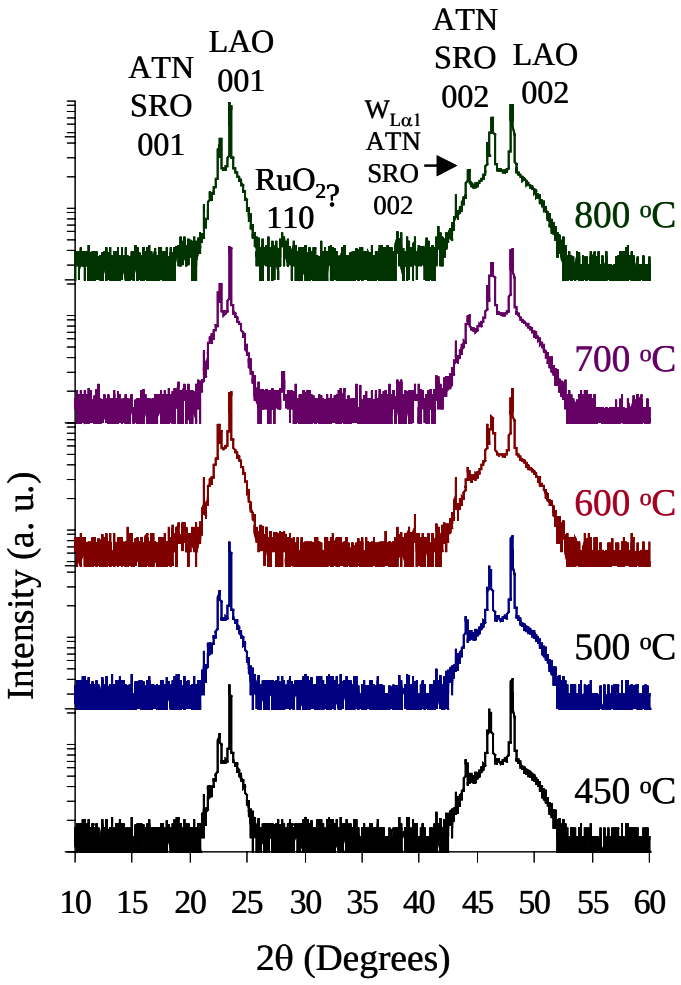


Figure **5.4**: XRD patterns of $Ag(Ta_{0.5}Nb_{0.5})O_3$ films on $(001)SrRuO_3/(001)LaAlO_3$ substrates as a function of crystallization temperature. Patterns were taken at generator settings of 10 mA and 15 kV.

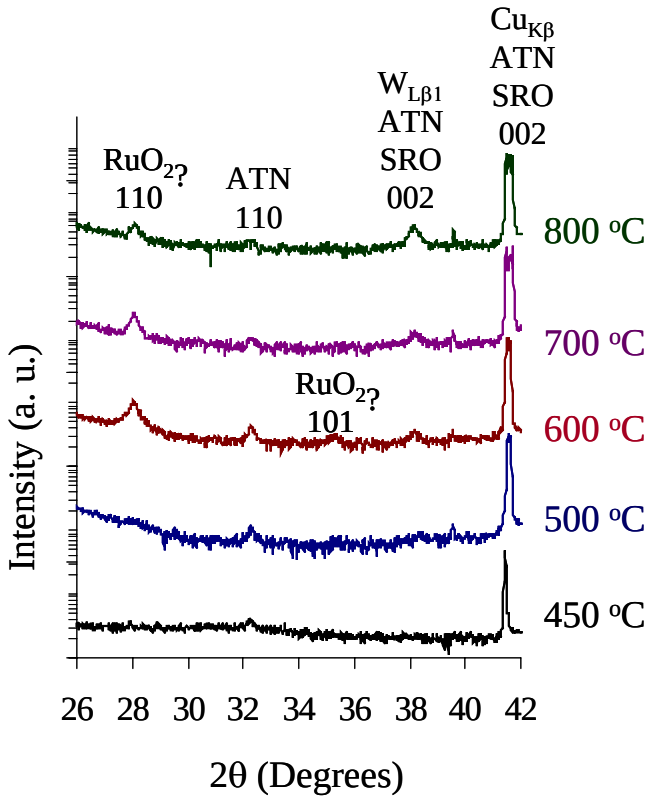


Figure **5.5**: XRD patterns of $Ag(Ta_{0.5}Nb_{0.5})O_3$ films $(001)SrRuO_3/(001)LaAlO_3$ substrates as a function of crystallization temperature. Patterns were taken at generator settings of 40 mA and 40 kV.

Out of plane lattice constants of the films were calculated using a Nelson–Riley fit (See Table **5.3**). The films had out of plane lattice constants of c=3.92±0.01 Å. These values are similar to the room temperature lattice parameters of ATN ceramics (a: 3.929 Å b: 3.926 Å c: 3.930 Å and β: 90.49°, ICDD 89-7738).

Table 5.3: Out of plane lattice constants of the $Ag(Ta_{0.5}Nb_{0.5})O_3$ films on $(001)SrRuO_3/(001)LaAlO_3$ substrates

| Crystallization Temperature (°C) | Out of Plane Constant (Å) |
|---|---|
| 500 | 3.92±0.01 |
| 600 | 3.92±0.01 |
| 700 | 3.92±0.01 |
| 800 | 3.92±0.01 |

Rocking curves of the 004 ATN perovskite peak were performed at generator settings of 30 mA and 35 kV with a step size of 0.01° and a step duration of 0.5 second. While the ATN film crystallized at 500 °C had a FWHM of 0.98±0.02° (Table 5.4), the FWHM of the films decreased with an increase in crystallization temperature and was as low as 0.65±0.02° for the film crystallized at 800 °C. A comparison of Tables 5.2 and 5.4 also demonstrates that the ATN film quality is superior on the SRO/LAO substrates, most likely due to the better lattice match ($a_0$ is 3.93 Å for relaxed $SrRuO_3$, ~3.93 Å for ATN and substantially smaller, $a_0$ = 3.79 Å and $\alpha$ of 90.12°, ICDD 85-0848 for LAO substrates).

Table 5.4: Full width half maximum values from 004 rocking curves for $Ag(Ta_{0.5}Nb_{0.5})O_3$ films deposited on $(001)SrRuO_3/(001)LaAlO_3$ substrates

| Crystallization Temperature (°C) | Full Width Half Maximum (°) |
|---|---|
| 500 | 0.98±0.02 |
| 600 | 0.72±0.02 |
| 700 | 0.67±0.02 |
| 800 | 0.65±0.02 |

It is clear that CSD ATN films on LAO and SRO/LAO are highly h00 textured. To determine whether they were oriented in-plane as well, the 321 and 231 off normal ATN reflections were checked using a four circle diffractometer. These XRD peaks were selected to distinguish ATN and PLD SRO separately in a φ scan. The θ and χ positions of these peaks were 47.13° and 15.23° for the ATN films. Based on a stereographic projection, it was determined that the comparable SRO peaks should have θ and χ positions of 47.17° and 15.50°, a difference large enough that the film peaks could be monitored separately.

Figure 5.6 shows φ scans of the 321 and 231 family reflections of ATN films that were crystallized at 500 °C both on (001) $LaAlO_3$ and $(001)SrRuO_3/(001)LaAlO_3$ substrates together with an ATN film crystallized at 800 °C on a $(001)SrRuO_3/(001)LaAlO_3$ substrate. All of these films were well-aligned in-plane, demonstrating that epitaxy is possible at crystallization temperatures as low as 500 °C.

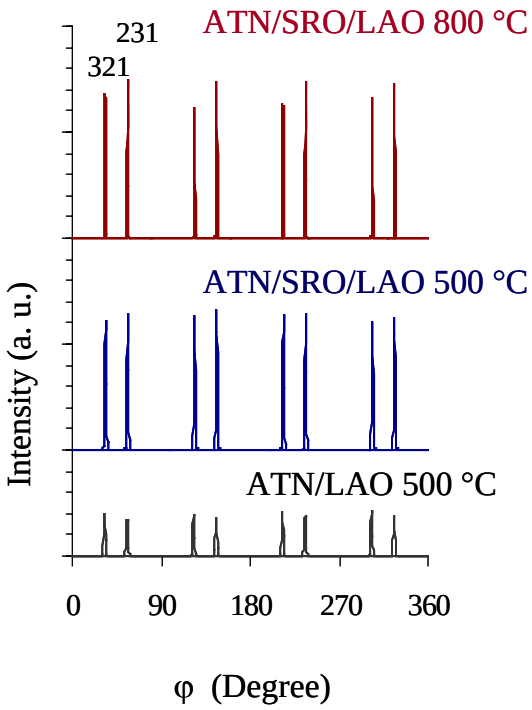


Figure **5.6**: (321) and (231) family XRD reflections of ATN films deposited on (001)$LaAlO_3$ and crystallized at 500 °C and (001)$SrRuO_3$/(001)$LaAlO_3$ substrates for crystallizations at 500 °C and 800 °C. Patterns were taken using generator settings of 40 kV and 18 mA. (Data are courtesy of M. D. Biegalski.)

A stereographic projection based on the lattice parameters of a room temperature ATN ceramic (ICDD 89-7738) is shown in Figure **5.7**. Inspection of the figure demonstrates that the 321 and 231 family planes of the ATN films should be observed together in the φ scans, because they share similar θ and χ positions. The θ values are quite close since the d-spacings are similar, and the χ positions because they are a comparable angular distance away from the [001] direction. Therefore, when the substrate is tilted off axis from [001] to a χ position of ~15.23° for a φ scan, these reflections were observed together for the ATN film.

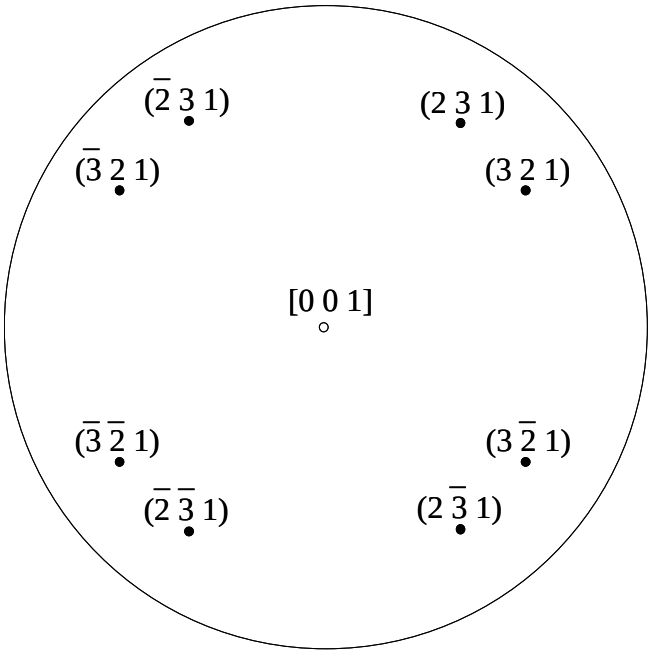


Figure 5.7: A simulated stereographic projection of ATN based on ICDD 89-7738 ($a_0$: 3.929 Å $b_0$: 3.926 Å and $c_0$: 3.930 Å, β: 90.49°) showing that poles of the (321) and (231) family planes have similar angular distances from the [001] direction.

The χ positions of the ATN films were observed at ~15.23° which was slightly different than the χ positions of ATN ceramics at ~15.49°. The difference suggested that films were distorted from the room temperature crystal structure of ATN ceramics.

Using the available four circle XRD patterns, in plane lattice parameters of ATN films were calculated using Nelson–Riley fits and d-spacings of (321) and (231) ATN family planes (Table 5.5). The in-plane lattice parameters were around a=3.94±0.01 Å. These values are similar to the room temperature lattice parameters of ATN ceramics (a:

3.929 Å b: 3.926 Å c: 3.930 Å and β: 90.49°, ICDD 89-7738), demonstrating that the films were relaxed.

Table **5.5**: In plane lattice parameters of $Ag(Ta_{0.5}Nb_{0.5})O_3$ films deposited on (001)$LaAlO_3$ or (001)$SrRuO_3$/(001)$LaAlO_3$ substrates

| Type of Substrate | Crystallization Temperature (°C) | In Plane Lattice Parameter (Å) |
|---|---|---|
| LAO | 500 | 3.94±0.01 |
| SRO/LAO | 500 | 3.95±0.01 |
| SRO/LAO | 800 | 3.94±0.01 |

The θ – 2θ XRD patterns of the $AgTaO_3$ (ATO) and $AgNbO_3$ (ANO) thin films deposited on SRO/LAO substrates and crystallized at 750 °C (Figure **5.8**) were similar to those of the 00*l* epitaxial ATN films. Namely, the (00*l*) perovskite family ATO and ANO peaks were strong and there was an unknown peak at 28.3° matching $RuO_2$ for both films. In addition, φ scans of the 321 and 231 family reflections of ATO and ANO films showed that these films were also (00*l*) epitaxial (Figure **5.9**).

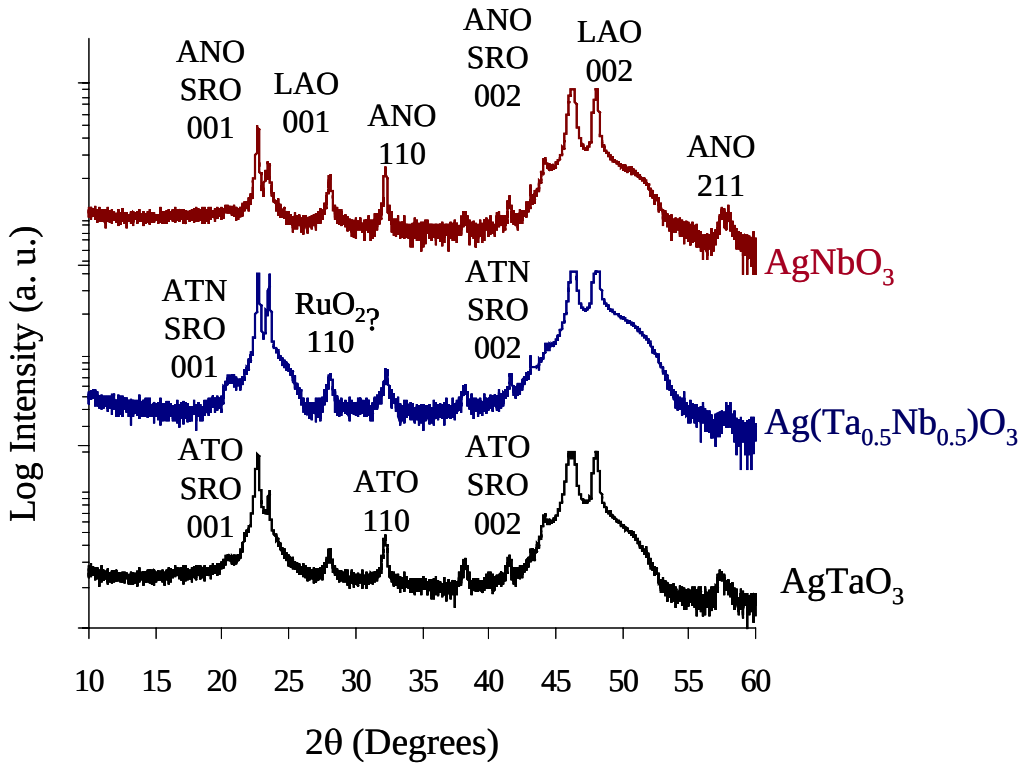


Figure **5.8**: XRD patterns of ~ 300 nm thick $AgNbO_3$, $Ag(Ta_{0.5}Nb_{0.5})O_3$ and $AgTaO_3$ films deposited on (001)$SrRuO_3$/(001)$LaAlO_3$ substrates and crystallized at 750 °C. Patterns were taken at X-ray generator settings of 30 mA and 35 kV.

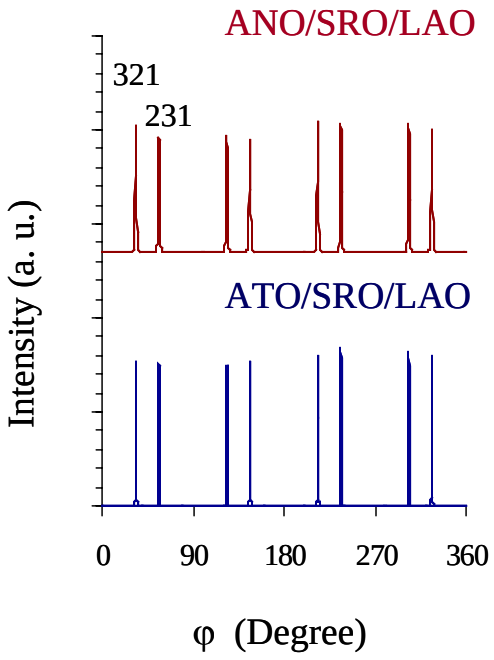


Figure **5.9**: (321) and (231) family XRD reflections of $AgTaO_3$ and $AgNbO_3$ films deposited on (001)$SrRuO_3$/(001)$LaAlO_3$ substrates and crystallized at 750 °C. Patterns were taken using generator settings of 40 kV and 18 mA. (Data are courtesy of M. D. Biegalski.)

The in and out of plane lattice parameters of the ATO and ANO films were calculated using Nelson–Riley fits (Table **5.6**). For ATO, both lattice parameters were 3.94±0.01 Å. This value (within the error range) is comparable to the room temperature lattice parameters of ATO ceramics (a: 3.928 Å and α: 89.30°.[2] ). The out of plane lattice parameter of 3.93±0.01 Å for the ANO film was similar to that of ANO ceramics (a: 3.940 Å b: 3.914 Å c: 3.940 Å and β: 90.52°, ICDD 22-0471). The in plane lattice parameter was 3.94±0.01 Å.

Table 5.6: Lattice parameters of $AgTaO_3$ and $AgNbO_3$ films deposited on $(001)SrRuO_3/(001)LaAlO_3$ substrates and crystallized at 750 °C

| Film Composition | Out of Plane Lattice Parameter (Å) | In Plane Lattice Parameter (Å) |
|---|---|---|
| $AgTaO_3$ | 3.94±0.01 | 3.94±0.01 |
| $AgNbO_3$ | 3.93±0.01 | 3.94±0.01 |

## 5.4 Dielectric Properties of $Ag(Ta_xNb_{1-x})O_3$ Films Deposited on $(001)SrRuO_3/(001)LaAlO_3$ Substrates:

Electrical characterization of ATN, ATO and ANO films was performed by preparing parallel plate capacitor structures. While the SRO layer acted as a bottom electrode, platinum top electrodes with diameters from 120 to 250 μm were sputtered onto the film through a shadow mask. After top electrode deposition, the samples were annealed at 500 °C for 30 min. under flowing $O_2$ in a quartz tube furnace to decrease the dielectric loss values.

### 5.4.1 Dielectric Properties of $Ag(Ta_{0.5}Nb_{0.5})O_3$ Films Deposited on $(001)SrRuO_3/(001)LaAlO_3$ Substrates:

Table 5.7 shows the dielectric constant and loss of ATN films at 100 kHz as a function of crystallization temperature. The dielectric constant of the films increased from 260±25 to 360±35 with an increase in the crystallization temperature from 500 to

800 °C. The previously noted improvement in the crystallinity of the ATN films with higher crystallization temperatures was likely to be responsible for the higher dielectric constants. The maximum dielectric constant of 360±35 is slightly lower than the value of 410 reported for ceramic samples at room temperature. But, as will be discussed in temperature dependent dielectric property section, there is shift in the $M_2$-$M_3$ phase transition for the ATN film from 50 to –190 °C, and the peak dielectric constants of both ceramics and films are similar ~410 around this phase transition temperature. Typical loss tangent values at room temperature were on the order of ~0.015 at 100 kHz for the ATN films and the smallest loss value was observed for a 700 °C crystallized film with a value of 0.007±0.002.

Table **5.7**: Dielectric constant and loss of (001) epitaxial ATN films on (001)$SrRuO_3$/(001)$LaAlO_3$ substrates as a function of crystallization temperature. Measured with a 30 mV oscillation level at 100 kHz

| Crystallization Temperature (°C) | $\varepsilon_r$ | tanδ |
|---|---|---|
| 500 | 260±25 | 0.017±0.001 |
| 600 | 330±30 | 0.009±0.004 |
| 700 | 350±35 | 0.007±0.002 |
| 800 | 360±35 | 0.011±0.002 |

The dielectric constant and loss of a (00*1*) epitaxial ATN film deposited on a (001)$SrRuO_3$/(001)$LaAlO_3$ substrate at 750 °C were measured from 1 Hz to 1 kHz using an HP/Agilent 3562A dynamic signal analyzer and from 1 to 100 kHz using an

HP/Agilent 4284A precision LCR meter with an oscillation level of 30 mV (Figure **5.10**). It is apparent from the figure that the ATN film had some frequency dependence in the range of 1 Hz to 100 kHz, probably associated with a finite level of space charge polarizability.

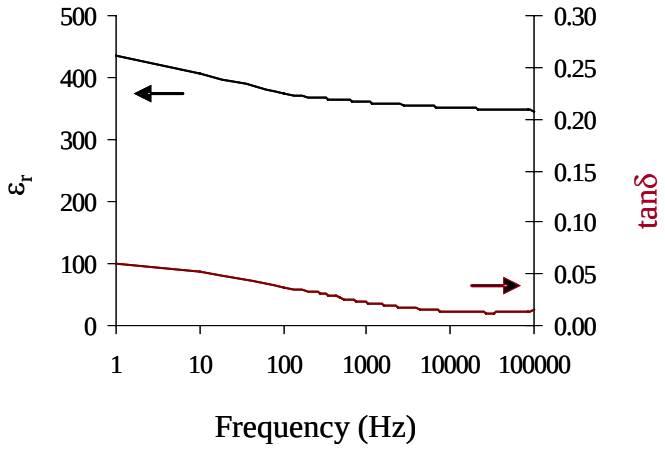


Figure **5.10**: Frequency dependence of the dielectric constant and loss for a (00*l*) epitaxial $Ag(Ta_{0.5}Nb_{0.5})O_3/001)SrRuO_3/(001)LaAlO_3$ film crystallized at 750 °C. Measurement was performed using a 30 mV oscillation level.

The temperature dependence of the dielectric constant and loss of the same sample were measured by heating the sample from room temperature to 450 °C with a heating rate of 2 °C/min on a probe station and cooling the sample in a Delta design chamber to –190 °C with a cooling rate of 2 °C/min. (Figure **5.11**). The capacitance change and instantaneous TCC values at 100 kHz were +5.7 % and -0.066 %/°C at –55 °C and –12.1 % and -0.148 %/°C at 120 °C. The shoulder of a diffuse maximum

observed in the dielectric constant near –190 °C may correspond to the phase transition between the $M_2$ and $M_3$ phases. For ATN ceramics, the $M_2$-$M_3$ phase transition is associated with a diffuse maximum in the dielectric constant occurring at 50 °C (Figure **5.12**).[3, 4] Therefore, the $M_2$-$M_3$ phase transition temperature for the film is shifted substantially. Large shifts in transition temperatures are common in thin films for a variety of reasons, including variations in stoichiometry, growth stresses, and clamping of the films by substrates, among others.[5, 6] For example, strain and stress fields have previously been shown to affect the stability regions of the ferroelectric phases in a number of perovskite, and therefore can lead to large shifts in phase transition temperatures of the films.[5-7]

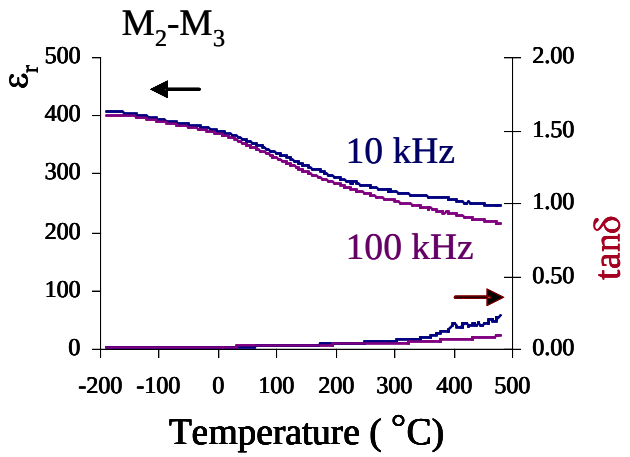


Figure **5.11**: Temperature dependence of the dielectric constant and loss for a (00*l*) epitaxial $Ag(Ta_{0.5}Nb_{0.5})O_3$/(001)$SrRuO_3$/(001)$LaAlO_3$ film crystallized at 750 °C. Measurements were performed at 10 and 100 kHz using a 30 mV oscillation level.

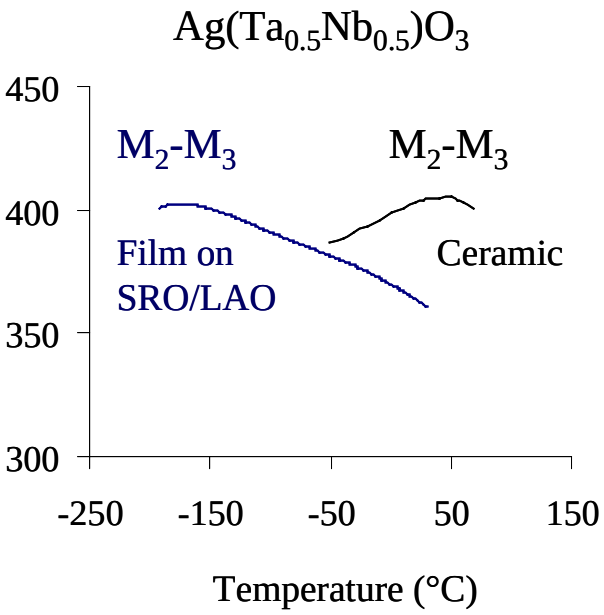


Figure **5.12**: Temperature dependence of the dielectric constants for a (00*l*) epitaxial $Ag(Ta_{0.5}Nb_{0.5})O_3/(001)SrRuO_3/(001)LaAlO_3$ film crystallized at 750 °C and $Ag(Ta_{0.5}Nb_{0.5})O_3$ ceramic. Measurements were performed at 100 kHz using a 30 mV oscillation level for the film and at 1.5 GHz for the ceramic.[4]

The $M_1$–$M_2$ phase transition is not well defined for ceramic ATN samples structurally, but is reported to be within 50 °C of the $M_2$–$M_3$ phase transition.[2, 8] For a composition of $Ag(Ta_{0.4}Nb_{0.6})O_3$, the $M_1$–$M_2$ phase transition is associated with a slight maximum in the dielectric constant and a strong DC field dependence (a dc field of 5 kV/cm shifts maximum value of dielectric constant ~20 % down) for the ceramic samples.[9] In order to probe the $M_1$–$M_2$ phase transition for ATN films, the temperature dependent dielectric properties were acquired with a 66 kV/cm DC field bias with a superimposed small ac field at 100 kHz (Figure **5.13**). However, there was not much DC bias field dependence for the film observed to temperatures as low as –180 °C, suggesting that $M_1$–$M_2$ phase transition may be below the measurement range.

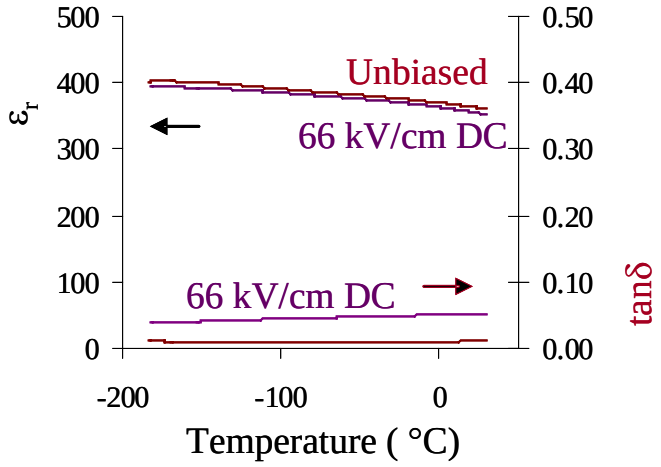


Figure **5.13**: Temperature dependence of the dielectric constant and loss for a (00*l*) epitaxial $Ag(Ta_{0.5}Nb_{0.5})O_3/(001)SrRuO_3/(001)LaAlO_3$ film crystallized at 750 °C. Measurements were performed at 100 kHz with a 30 mV oscillation level with a DC bias of 66 kV/cm or without any DC bias.

None of the higher temperature phase transitions were observed in the dielectric response of the film. In ceramic ATN samples, a phase transition between $M_3$-O takes place at 370 °C and is associated with a sharp but small increase in dielectric constant. The absence of such a sharp increase in the dielectric constant for the film suggests either that the $M_3$-O phase transition might be shifted to a temperature higher than 450 °C or that it is difficult to detect for the film. Ceramic ATN samples show O-T and T-C transitions at 420 °C and at 600 °C. These were reported to show small dielectric anomalies with temperature.[2, 8] No clear evidence for either transition was observed in the films within the measurement range.

In order to check for ferroelectricity in the ATN film, polarization - electric field (P-E) hysteresis–loop measurements were performed at 0.5 kHz at room temperature and at –125 °C (Figure **5.14**). Polarization curves were found to be very similar and linear with the applied electric fields suggesting that the film did not show any ferroelectricity within the applied field range. This is also consistent with suppression of the $M_2$-$M_3$ transition to lower temperatures (i.e. the film is likely to be in the $M_3$ phase at these measurement temperatures). The $M_3$ and $M_2$ phases were reported to be antiferroelectric and the $M_1$ phase was reported to be weakly ferroelectric in ceramics.[4] If the films are antiferroelectric, it was not possible to confirm this at the field levels probed.

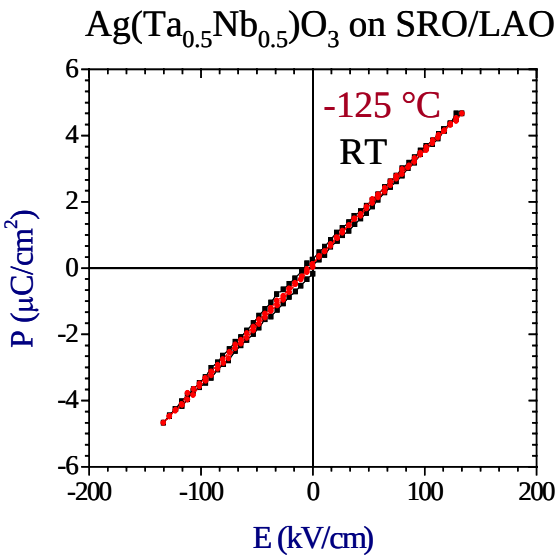


Figure **5.14**: Polarization – electric field responses for a (00*l*) epitaxial $Ag(Ta_{0.5}Nb_{0.5})O_3$ /(001)$SrRuO_3$/(001)$LaAlO_3$ film crystallized at 750 °C. Measurements were performed at 0.5 kHz at room temperature and at –125 °C by using a 30 mV oscillation level.

It is possible to calculate the dielectric constants from the polarization measurements based on the susceptibility equation (Equation **5.1**). In order to calculate the dielectric constants of the film, the polarization was plotted against the electric field and a linear regression passing through zero was fitted. The slope was used to calculate the dielectric constants. According to these calculations, the ATN film had dielectric constants of 400±40 at RT and 405±40 at –125 °C at 0.5 kHz. These values agree with the dielectric constants calculated from capacitance measurements (Table **5.8**).

$$\chi = \varepsilon_r - 1 = \frac{P}{\varepsilon_0 E} \qquad \text{(Equation 5.1)}$$

Table **5.8**: Dielectric constants from capacitance and polarization-electric field response measurements at room temperature and at –125 °C at 0.5 kHz for a (00*l*) epitaxial $Ag(Ta_{0.5}Nb_{0.5})O_3$/(001)$SrRuO_3$/ (001)$LaAlO_3$ film crystallized at 750 °C

| Temperature (°C) | $\varepsilon_r$ from capacitance | $\varepsilon_r$ from P-E trace |
|---|---|---|
| 25 | 380±40 | 400±40 |
| -125 | 410±40 | 405±40 |

The DC field tunability, the % change in dielectric constant under DC bias from its unbiased value, of the film at room temperature (Figure **5.15**) was not hysteretic but was small. The breakdown strength of the film was ~230 kV/cm. This relatively low dielectric breakdown strength also limited the tunability to 4.8 % at 100 kHz and a 150 kV/cm bias. The corresponding K factor (calculated by taking the ratio of the tunability

to the loss) of the film was low ~3.4 due to limited tunability and relatively high loss. When the measurement was repeated at 77 K to decrease the electrical conductivity and therefore to increase dielectric breakdown strength, the capacitance change (Figure **5.16**) became hysteretic and complex and DC field tunability did not improve. The observed hysteresis results might be due to the appearance of ferroelectricity at low temperatures or might show migration of ionic defects.

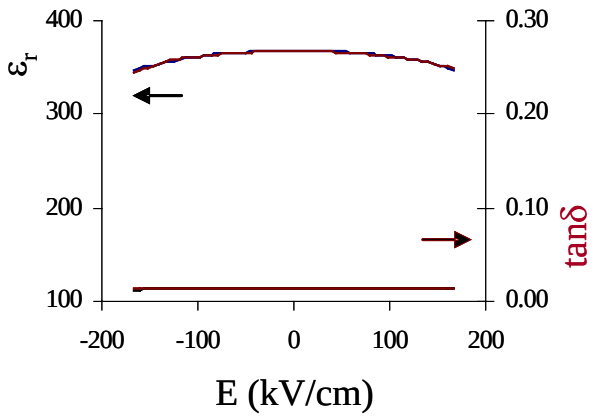


Figure **5.15**: DC field tunability for a (00*l*) epitaxial $Ag(Ta_{0.5}Nb_{0.5})O_3/(001)SrRuO_3/(001)LaAlO_3$ film crystallized at 750 °C. Measurement was performed at 100 kHz at room temperature using a 30 mV oscillation level.

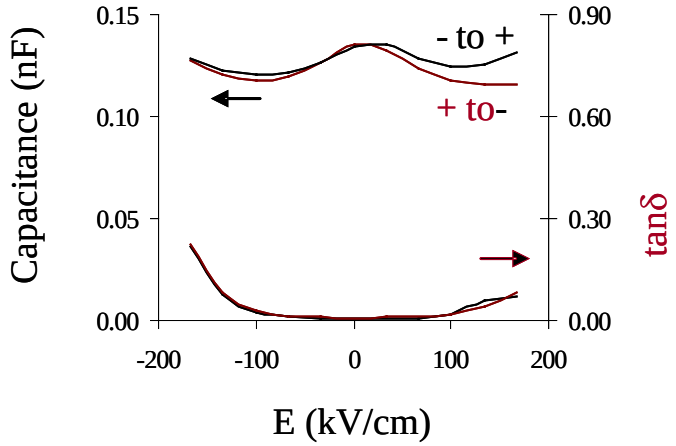


Figure **5.16**: DC field tunability for a (00*l*) epitaxial $Ag(Ta_{0.5}Nb_{0.5})O_3$/ (001)$SrRuO_3$/(001)$LaAlO_3$ film crystallized at 750 °C. Measurements were performed at 100 kHz at 77 K using a 30 mV oscillation level.

### 5.4.2 Dielectric Properties of $AgTaO_3$ and $AgNbO_3$ Films Deposited on (001)$SrRuO_3$/(001)$LaAlO_3$ Substrates:

The dielectric constant and loss as a function of frequency of the $AgTaO_3$ (ATO) and $AgNbO_3$ (ANO) films deposited on the (001)$SrRuO_3$/(001)$LaAlO_3$ substrate are shown in Figure **5.17** and Figure **5.18**. According to the figures, both films had modest frequency dependence in the dielectric constant (–16.0 % for ATO film and –8.1% for the ANO film) from 10 Hz to 100 kHz. At 100 kHz the dielectric constant of the ATO film was 110±10. This is slightly lower than the bulk value of 150. In contrast, the dielectric constant of the $AgNbO_3$ film was 550±55. This is considerably higher than the dielectric constant of 120 observed for ANO ceramics at room temperatures. The loss tangent

values were 0.025±0.005 for the ATO film and 0.020±0.005 for the ANO film at room temperature.

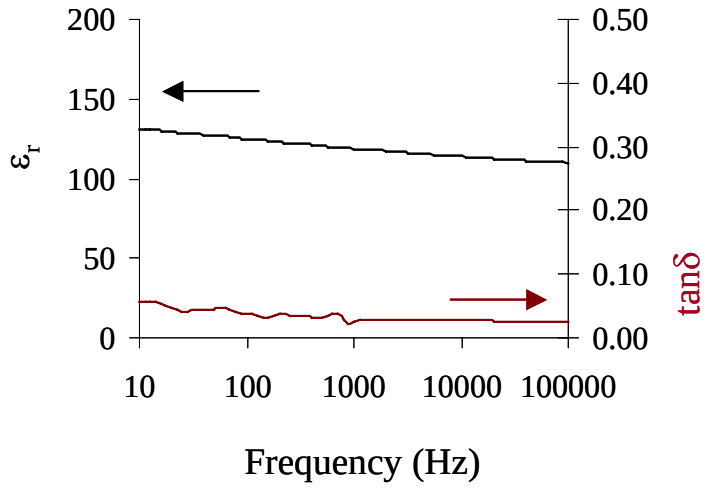


Figure **5.17**: Frequency dependence of the dielectric constant and loss for a (00*l*) epitaxial $AgTaO_3$/(001)$SrRuO_3$/(001)$LaAlO_3$ film crystallized at 750 °C. Measurement was performed using a 30 mV oscillation level.

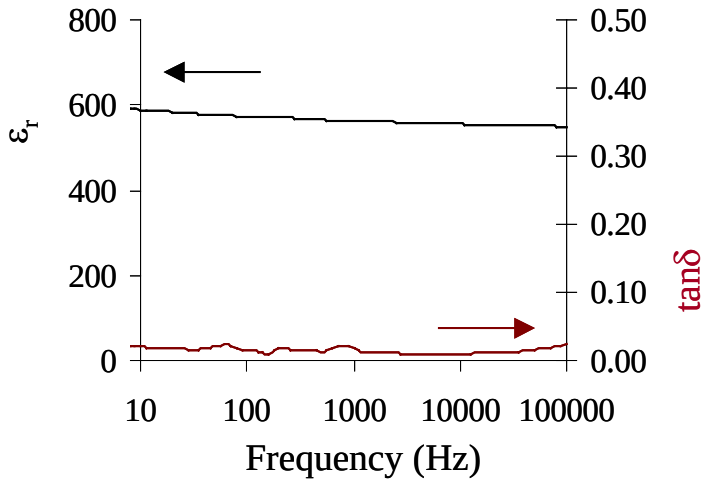


Figure **5.18**: Frequency dependence of the dielectric constant and loss for a (00*l*) epitaxial $AgNbO_3$/(001)$SrRuO_3$/(001)$LaAlO_3$ film crystallized at 750 °C. Measurement was performed using a 30 mV oscillation level.

ATO and ANO ceramics have been reported to be weakly ferroelectric at room temperature.[10, 3] In order to check for ferroelectricity in these films, polarization–electric field response measurements were performed at 0.5 kHz at room temperature (Figure **5.19** and Figure **5.20**). The polarization curves were found to be linear, suggesting that the films did not show any ferroelectricity within the applied field range. The dielectric constants derived from the polarization – electric field measurements were 150±15 for the ATO film, and 570±55 for the ANO film. Those values agreed with the small signal dielectric constants calculated from capacitance measurements (Table **5.9**). P-E measurements could not be performed at higher fields and temperatures because of higher losses seen for the films.

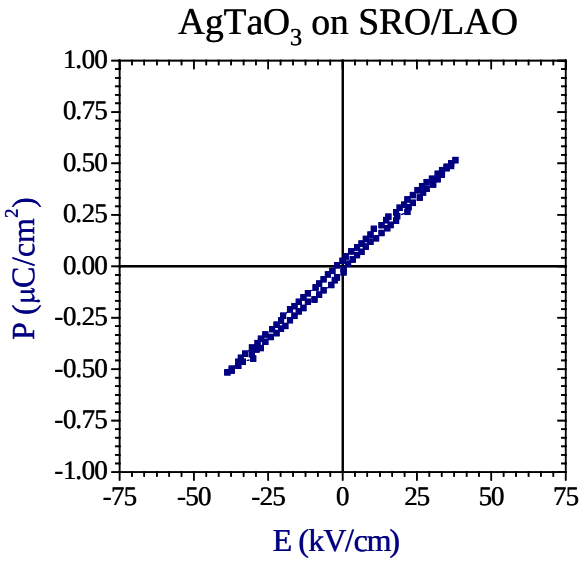


Figure **5.19**: Polarization – electric field response for a (00*l*) epitaxial $AgTaO_3$ /(001)$SrRuO_3$/(001)$LaAlO_3$ film crystallized at 750 °C. Measurement was performed at 0.5 kHz.

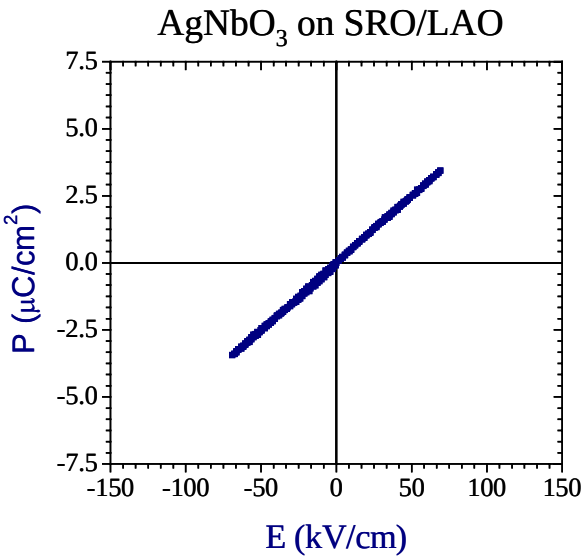


Figure **5.20**: Polarization – electric field response for a (00*l*) epitaxial $AgNbO_3$ /(001)$SrRuO_3$/(001)$LaAlO_3$ film crystallized at 750 °C. The measurement was performed at 0.5 kHz.

Table **5.9**: Dielectric constants from capacitance and polarization-electric field response measurements at room temperature and at 0.5 kHz for a (00*l*) epitaxial $AgTaO_3$ and $AgNbO_3$ films crystallized at 750 °C

| Film composition | $\varepsilon_r$ from capacitance | $\varepsilon_r$ from P-E trace |
|---|---|---|
| $AgTaO_3$ | 120±10 | 150±15 |
| $AgNbO_3$ | 570±55 | 570±55 |

Figure **5.21** shows the temperature dependent dielectric constants of $AgTa_{1-x}Nb_xO_3$ ceramics. $AgTaO_3$ has a weakly ferroelectric rhombohedral phase (R) with a dielectric constant of 150 and $AgNbO_3$ has a weakly ferroelectric monoclinic phase ($M_1$) with a dielectric constant of 120 at room temperature at 1 MHz.[8]

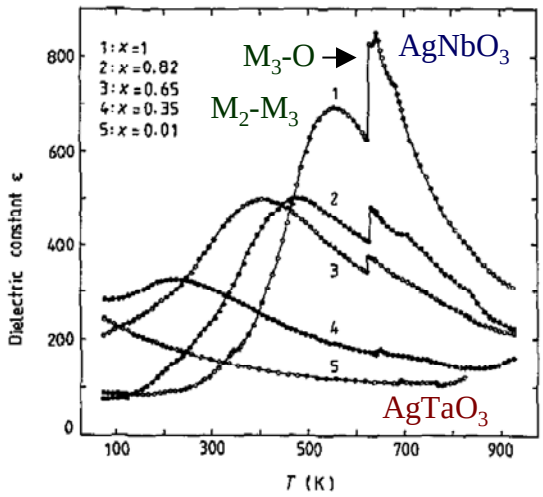


Figure **5.21**: Temperature dependent dielectric constants of bulk $AgTa_{1-x}Nb_xO_3$ ceramics at 1 MHz.[8]

The temperature dependent dielectric properties of $AgTaO_3$ and $AgNbO_3$ films on (001)SRO/(001)LAO substrates are shown in Figure **5.22** and Figure **5.23** at 10 and 100 kHz with a 30 mV oscillation level. While the $AgTaO_3$ film had a similar temperature dependent dielectric constant response as the ceramic sample, with a slight decrease in permittivity with increasing temperature, the $AgNbO_3$ film did not show the rapid increase seen in the dielectric constant from 120 to 700 of the ceramic sample with the temperature increase from room temperature to ~270 °C (Figure **5.24**). Instead, the dielectric constant of the $AgNbO_3$ film increased slightly from 550±50 till ~200 °C and then increased to 600±50 with a diffuse maximum at ~300 °C. The capacitance change and corresponding TCC were –5.6 % and –0.010 %/°C for ATO film and 1.1 % and 0.011 %/°C for the ANO film at 120 °C at 100 kHz. The high dielectric constant values of 550±50 for the ANO film at room temperature, coupled with the slight jump in dielectric constant near ~300 °C suggested that either the $M_2$-$M_3$ or the $M_3$–O phase transitions might be taking place at ~300 °C. Thus, either the $M_2$ or the $M_3$ phase might be stable at room temperature for the ANO film. However, the large shift seen in the $M_2$-$M_3$ phase transition observed for the $Ag(Ta_{0.5}Nb_{0.5})O_3$ film was not seen for the ANO film. The reason is not clear at this point and needs further investigation. Stabilization of higher temperature phases either the $M_2$ or the $M_3$ phase in the ANO film might be related to clamping of the film by substrate.[5-7] The lower temperature phase transition, $M_1$-$M_2$, observed in ANO ceramics, were not detected clearly for the film.

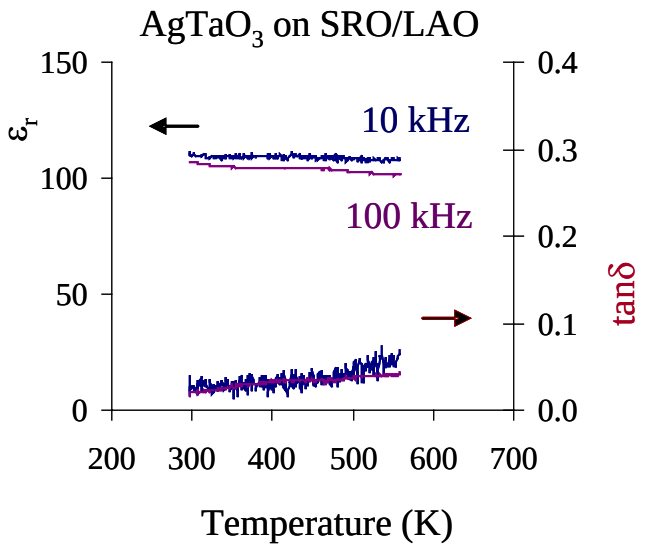


Figure **5.22**: Temperature dependence of the dielectric constant and loss for a (00*l*) epitaxial $AgTaO_3$/(001)$SrRuO_3$/(001)$LaAlO_3$ film crystallized at 750 °C. Measurements were performed at 10 and 100 kHz using a 30 mV oscillation level.

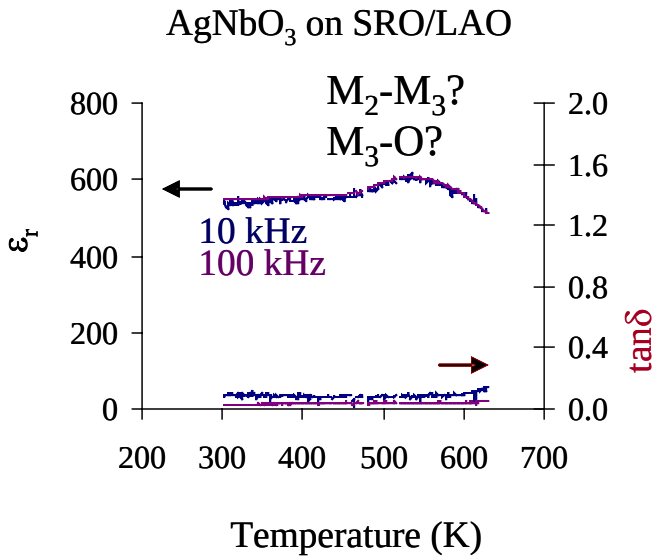


Figure **5.23**: Temperature dependence of the dielectric constant and loss for a (00*l*) epitaxial $AgNbO_3$/(001)$SrRuO_3$/(001)$LaAlO_3$ film crystallized at 750 °C. Measurements were performed at 10 and 100 kHz using a 30 mV oscillation level.

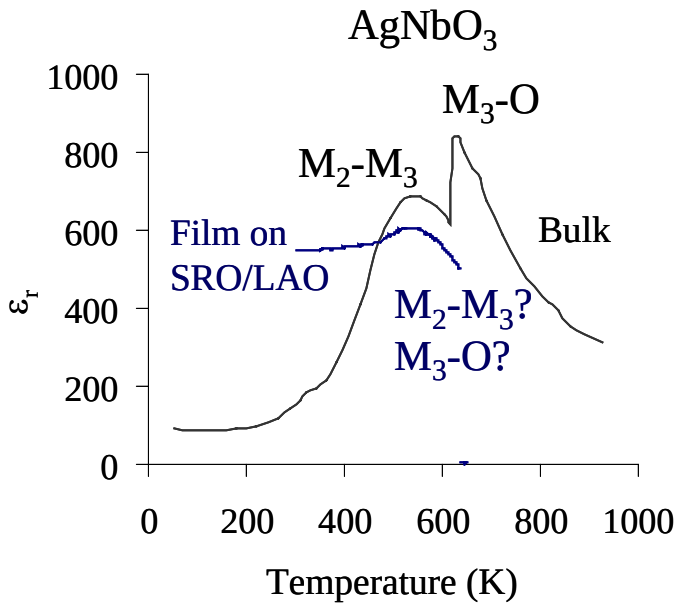


Figure **5.24**: Temperature dependence of the dielectric constants for a (00*l*) epitaxial $AgNbO_3$/(001)$SrRuO_3$/(001)$LaAlO_3$ film crystallized at 750 °C and $AgNbO_3$ ceramic. Measurements were performed at 100 kHz using a 30 mV oscillation level for the film and at 1 MHz for the ceramic.[8]

The capacitance and loss responses of the $AgTaO_3$ film (Figure **5.25**) were not hysteretic, and the loss stayed low. The breakdown strength of the $AgTaO_3$ film was 300 kV/cm. The tunability was limited to 1.6 % at 230 kV/cm for the $AgTaO_3$ film. The corresponding K factor of 0.6 was the lowest of all the investigated silver tantalate niobate compositions. For the $AgNbO_3$ film, the capacitance and loss responses (Figure **5.26**) were not hysteretic, but the loss was higher under negative bias (i.e. when the top Pt electrode was kept at negative DC bias), probably due to the asymmetry in the electrodes.[11, 12] The breakdown strength of the $AgNbO_3$ film was also lower under negative bias (-200 kV/cm compared to 275kV/cm when DC bias was applied to the top Pt electrode). The tunability of the $AgNbO_3$ film was higher, with changes of 12.8 % at a

negative bias of -140 kV/cm and 21.4 % at 190 kV/cm. This higher tunability is most likely linked with the higher dielectric constant. The corresponding K factors for the ANO film at negative and positive DC field bias were ~6.1 and ~10.2. These values were the highest among the investigated silver tantalate niobate film compositions.

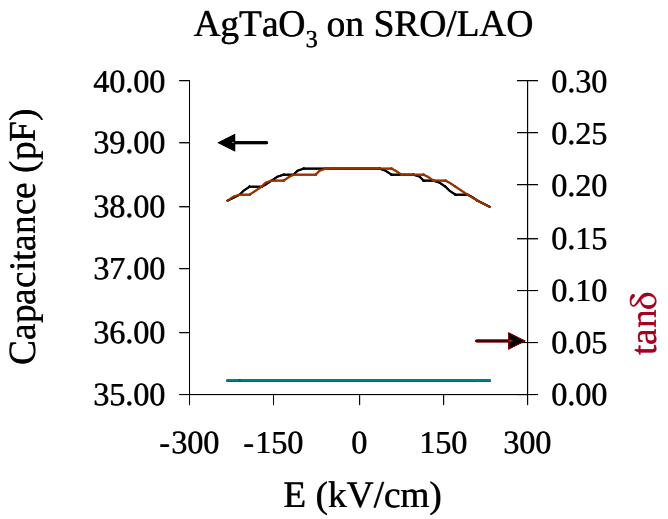


Figure **5.25**: Capacitance as a function of DC field bias for a (00*l*) epitaxial $AgTaO_3$/(001)$SrRuO_3$/(001)$LaAlO_3$ film crystallized at 750 °C. Measurement was performed at 100 kHz using a 30 mV oscillation level.

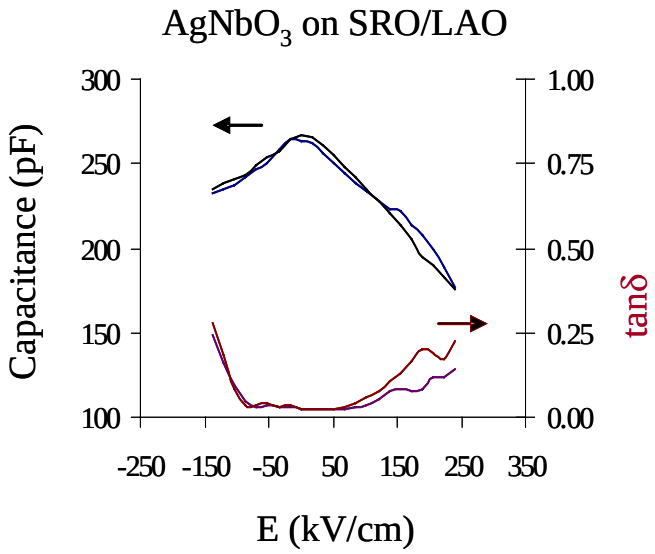


Figure **5.26**: Capacitance as a function of DC field bias for a (00*l*) $AgNbO_3$/(001)$SrRuO_3$/(001)$LaAlO_3$ film crystallized at 750 °C. Measurement was performed at 100 kHz using a 30 mV oscillation level.

### **5.5** Conclusions:

(00*l*) epitaxial thin films of $Ag(Ta_{0.5}Nb_{0.5})O_3$ (ATN), $AgTaO_3$ (ATO) and $AgNbO_3$ (ANO) were prepared by chemical solution deposition. ATN films that were deposited on (001)$LaAlO_3$ and (001)$SrRuO_3$/(001)$LaAlO_3$ substrates were crystalline for heat treatments of 500 °C or higher. Based on the XRD intensities, a limited reaction was suspected between the ATN film and SRO layer, but no reaction was detected between ATN films and LAO substrates. The ATN films deposited on SRO/LAO substrates had a better crystallinity than those on LAO substrates due to the better lattice match between ATN and SRO/LAO. The crystallinity of the ATN films improved on both substrates with an increase in crystallization temperature from 500 to 800 °C. Dielectric constants of

ATN films that were deposited on SRO/LAO substrates were also found to increase from 260±25 to 360±35 at 100 kHz at room temperature with an increase in crystallization temperature. Loss values were ~0.015 at 100 kHz, with the lowest values of 0.007±0.002 observed for a film crystallized at 700 °C. For an ATN film deposited on SRO/LAO at 750 °C, the frequency dependence of the dielectric properties was small for a measurement range of 1 Hz to 100 kHz. Based on temperature dependent dielectric constant, the transition between $M_2$ and $M_3$ phases was shifted from 50 °C (bulk ceramic value) to –190 °C for the film. The capacitance change and instantaneous TCC values at 100 kHz were +5.7 % and -0.066 %/°C at –55 °C and –12.1 % and -0.148 %/°C at 120 °C. Linear P-E curves at room temperature and at –125 °C suggested that the film was not ferroelectric at either temperature. The DC field tunability was not hysteretic but small, 4.8 % at 100 kHz and 150 kV/cm, due to limited breakdown strength of 230 kV/cm. The corresponding K factor of the film was low ~3.4 due to limited tunability and relatively high loss. The capacitance change of the film with DC field bias was hysteretic and complex at 77 K. This low tunability level could probably be increased substantially with process improvements.

$AgTaO_3$ (ATO) and $AgNbO_3$ (ANO) films that were deposited on SRO/LAO substrates at 750 °C had similar crystal structure features as (00*l*) epitaxial ATN films. The ATO film had a slightly lower dielectric constant of 110±10 at 100 kHz at room temperature than the bulk ceramic value of 150. In contrast, the ANO film had a considerably higher dielectric constant of 550±55 at 100 kHz at room temperature, than the bulk ceramic value of 120. Loss values were 0.025±0.005 for the ATO film and

0.020±0.005 for the ANO film at room temperature. Both films had small frequency dependence of the dielectric properties within the measurement range of 10 Hz to 100 kHz. While the $AgTaO_3$ film had similar temperature dependence in the dielectric constant as ceramic samples, the $AgNbO_3$ film had high dielectric constant values of 550±55 at room temperature and a slight increase in dielectric constant ~300 °C suggested that the ANO films might have either the $M_2$ or the $M_3$ phase at room temperature and either the $M_2$-$M_3$ or the $M_3$–O phase transition at ~300 °C. However, the large shift seen in the $M_2$-$M_3$ phase transition for the ATN film was not observed for the ANO film. The capacitance change and corresponding TCC values were –5.6 % and –0.010 %/°C for ATO film and 1.1 % and 0.011 %/°C for ANO film at 120 °C at 100 kHz. Both films had linear P-E traces at room temperature and therefore were not ferreoelectric within the applied field range. The room temperature DC field tunability of ATO film was not hysteretic, but limited to 1.6 % at 100 kHz and at 230 kV/cm field. The corresponding K factor of 0.6 was the lowest of the investigated silver tantalate niobate film compositions. In contrast, the DC field tunability of the ANO film was higher with a 12.8 % at negative bias of -140 kV/cm (where negative DC bias was applied to top Pt electrode) and 21.4 % at 190 kV/cm. Highest tunability values also resulted in the highest the K factors for the ANO film among the investigated film compositions. K-factors of the ANO film were ~6.1 and ~10.2 at negative and positive DC field bias. Use of asymmetric electrodes (top platinum and bottom SRO electrodes) yielding different leakage current characteristics for the different polarities was suspected

to be the reason for seeing higher breakdown strengths, and therefore higher tunability under positive bias for the film.

## 5.6 References:

[1] J.P. Maria, S.Trolier-McKinstry, D.G. Schlom, M.E. Hawley and G. W. Brown, "The influence of energetic bombardment on the structure and properties of epitaxial $SrRuO_3$ thin films grown by pulsed laser deposition," *Journal of Applied Physics*, **83** [8] 4373-4379 (1998).

[2] M. Pawelczyk, "Phase transitions in $AgTa_xNb_{1-x}O_3$ solid solutions," *Phase Transitions*, **8** 273-292 (1987).

[3] A. Kania, "$Ag(Nb_{1-x}Ta_x)O_3$ solid solutions, dielectric properties and phase transitions," *Phase Transitions*, **3** [2] 131-139 (1983).

[4] J. Petzelt, S. Kamba, E. Buixaderas, V. Bovtun, Z. Zikmund, A. Kania, V. Koukal, J. Pokorny, J. Polivka, V. Pashkov, G. Komandin and A. Volkov, "Infrared and microwave dielectric response of the disordered antiferroelectric $Ag(Nb,Ta)O_3$ system," *Ferroelectrics*, **223** 235-246 (1999).

[5] J. H. Haeni, P. Irvin, W. Chang, R. Uecker, P. Reiche, Y. L. Li, S. Choudhury, W. Tian, M. E. Hawley, B. Craigo, A. K. Tagantsev, X. Q. Pan, S. K. Streiffer, L. Q. Chen, S. W. Kirchoefer, J. Levy and D. G. Schlom, "Room –temperature ferroelectricity in strained $SrTiO_3$," *Nature*, **430** 758-761 (2004).

[6] N.A. Pertsev, A. G. Zernbilgotov, S. Hoffmann, R. Waser and A. K. Tagantsev, "Ferroelectric thin films grown on tensile substrates: Renormalization of the Curie-Weiss law and apparent absence of ferroelectricity," *Journal of Applied Physics*, **85** [3] 1698-1700 (1999).

[7] N.A. Pertsev, A. G. Zernbilgotov and A. K. Tagantsev, "Effect of mechanical boundary conditions on phase diagrams of epitaxial ferroelectric thin films," *Physical Review Letters*, **80** [9] 1988-1991 (1998).

[8] M. Hafid, G. E. Kugel, A. Kania, K. Roleder and M. D. Fontana, "Study of the phase transition sequence of mixed silver tantalate niobate $Ag(Nb_{1-x}Ta_x)O_3$ by inelastic light scattering," *Journal of Physics Condensed Matter*, **4** [9] 2333-2345 (1992).

[9] F. Zimmermann, W. Menesklou, E. Ivers-Tiffee, “Investigation of $Ag(Ta,Nb)O_3$ as tunable microwave dielectric,” *Journal of European Ceramic Society*, **24** 1811-1814 (2004).

[10] A. Kania and K. Roleder, “Ferroelectricity in $Ag(Nb_{1-x}Ta_x)O_3$ solid solutions,” *Ferroelectric Letters*, **2** 51-54 (1984).

[11] W. Hofman, S. Hoffmann and R. Waser, “Dopant influence on dielectric losses, leakage behaviour and resistance degradation of $SrTiO_3$ thin films,” *Thin Solid Films*, **305** 66-73 (1997).

[12] I. Stolichnov, A. Tagantsev, N. Setter, J. S. Cross and M. Tsukada, “Control of leakeage conduction of high fatigue endurance $(Pb,La)(Zr,Ti)O_3$ film ferroelectric capacitors with $Pt/SrRuO_3$ electrodes,” *Applied Physics Letters*, **75** [12] 1790–1792 (1999).

# Chapter 6

## $Ag(Ta_{0.5}Nb_{0.5})O_3$ Thin Films on Ag, $Ag/SiO_2/Si$ and $Ag/Ti/SiO_2/Si$ Substrates

### 6.1 Introduction:

Silver electrodes are widely investigated for high frequency applications because of their good electrical properties and low cost.[1, 2] As a result, it was important to check whether $Ag(Ta_{0.5}Nb_{0.5})O_3$ (ATN) films could be deposited on silver electrodes without having an extensive reaction. Thus, ATN films were deposited on silver foils, $Ag/SiO_2/Si$ and $Ag/Ti/SiO_2/Si$ substrates.

### 6.2 Deposition and Crystal Structure Development of $Ag(Ta_{0.5}Nb_{0.5})O_3$ Thin Films on Silver Substrates:

ATN films (~300 nm thick) were deposited on silver foils (99.998% purity, 0.25 mm thick, Alfa-Aesar Company, Ward Hill, MA) in a similar way as for (001) $SrRuO_3$/ (001)$LaAlO_3$ substrates (Figure **6.1**). Each layer was spun at 1500 rpm using 0.3 M solution, hot plate baked at 200 °C and 450 °C for 20 seconds and crystallized either at 550 or 750 °C for 1 minute in an $O_2$ environment using the RTA.

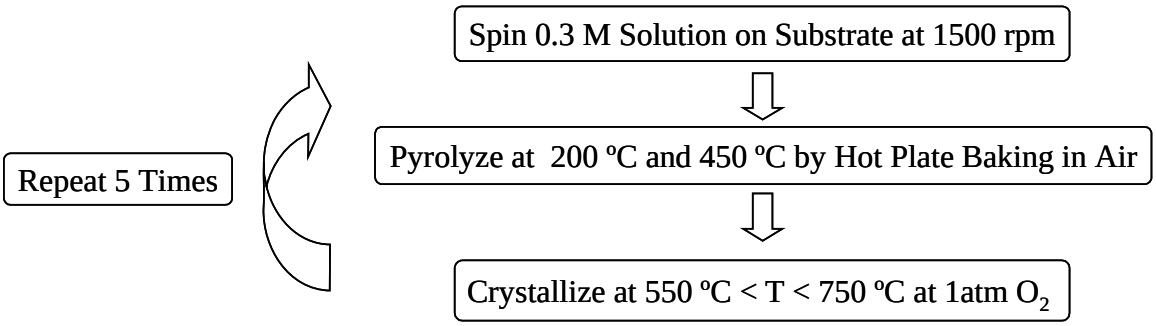


Figure **6.1**: Spinning and heat treatments steps of $Ag(Ta_{0.5}Nb_{0.5})O_3$ films that were deposited on silver foils.

Figure **6.2** shows XRD patterns of ATN films that were deposited on the silver foils at 550 and 750 °C as well as the XRD pattern of the silver foil. All the peaks in the XRD patterns matched to either pseudocubic perovskite ATN (ICDD 89-7738) or silver (ICDD 4-783). This suggested that there was no extensive reaction between the ATN film and the substrate leading to a crystalline reaction layer. In addition, the 00*l* family perovskite peaks of the ATN films had a higher relative intensity than the 00*l* family peaks of the standard powder X-ray pattern for ATN. In order to estimate the degree of 00*l* texture for the ATN film, the Lotgering method was used. The Lotgering factor (f) describes the area fraction of the material having 00*l* texture and was calculated using Equation **6.1**.[3, 4] The relative XRD peak intensities of the film and the ATN powder standard (ICDD 89-7738) were used for the Lotgering factor calculations. Based on the 2θ scans between 10 to 60°, both ATN films had Lotgering factors (f values) within 0.24±0.02. This suggested that ATN films had slight 00*l* preferred orientation when they were deposited on silver substrates.

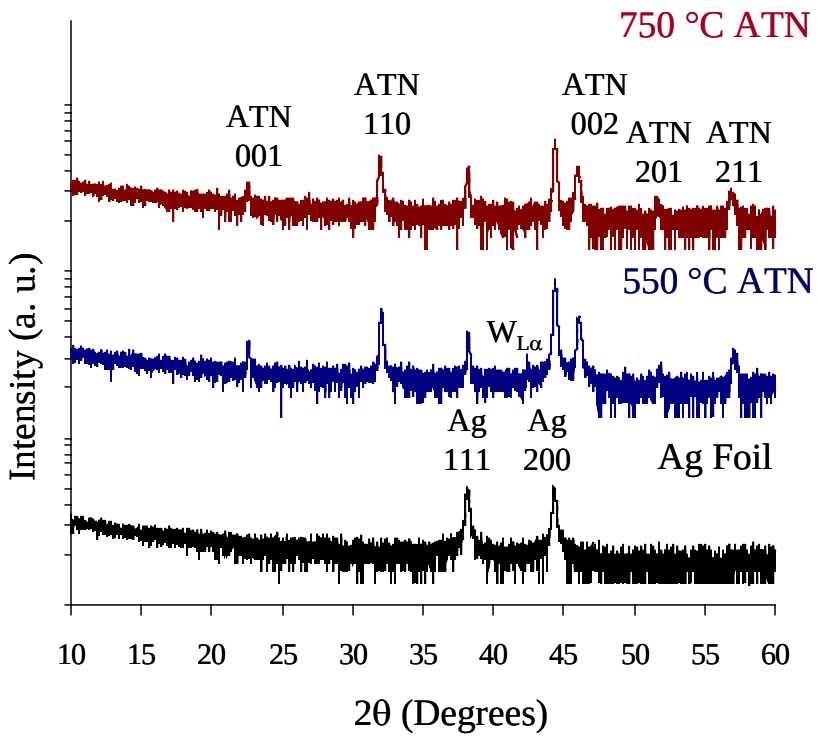


Figure **6.2**: XRD patterns of the silver foil and 550 and 750 °C crystallized ATN films on silver foils. Patterns were taken at generator settings of 35 kV and 30 mA.

$$f_{(00l)} = \frac{\frac{\sum I_{(00l)}}{\sum I_{(hkl)}} - \frac{\sum I_{0(00l)}}{\sum I_{0(hkl)}}}{1 - \frac{\sum I_{0(00l)}}{\sum I_{0(hkl)}}}$$ (Equation **6.1**)

where;

$\sum I_{(00l)}$ : Summation of intensities for the 00*l* XRD peaks.

$\sum I_{(hkl)}$ : Summation of intensities for the hkl XRD peaks.

$\sum I_{0(00l)}$ : Summation of intensities for the 00*l* XRD peaks for the randomly oriented sample.

$\sum I_{0(hkl)}$ : Summation of intensities for the hkl XRD peaks for the randomly oriented sample.

Getting dielectric data for the ATN films that were deposited on silver foils was problematic due to the rough silver surface and the low ATN film thickness (~300 nm). Attempts to polish the foils by using fine grit silicon carbide papers (600, 2400 and 4000 grit) failed due to the ductility of silver.

## 6.3 Deposition and Crystal Structure Development of $Ag(Ta_{0.5}Nb_{0.5})O_3$ Thin Films on $Ag/SiO_2/Si$ Substrates:

Use of a sputtered silver layer (~100 nm thick) on $SiO_2$/Si substrates (Silicon Quest Int., Santa Clara, CA) was investigated for ATN film deposition to achieve the smooth silver surface required for dielectric characterization of the films. An ATN film was crystallized at 750 °C on the $Ag/SiO_2/Si$ substrate in a similar way as films were deposited on (001) $SrRuO_3$ coated (001)$LaAlO_3$ substrates (Figure 6.1). The resulting XRD patterns of the ATN film (Figure **6.3**) had only XRD peaks corresponding to the pseudocubic perovskite phase, silver and the $SiO_2$/Si substrate. The fact that there were no additional XRD peaks suggested that there were no extensive crystalline reaction between sputtered silver and the ATN film. In addition, 00*l* family perovskite peaks of the ATN films were very intense and the film had a Lotgering factor of 0.80±0.02, i.e. the

ATN film had a strong 00*l* preferred orientation when deposited on a $Ag/SiO_2/Si$ substrate.

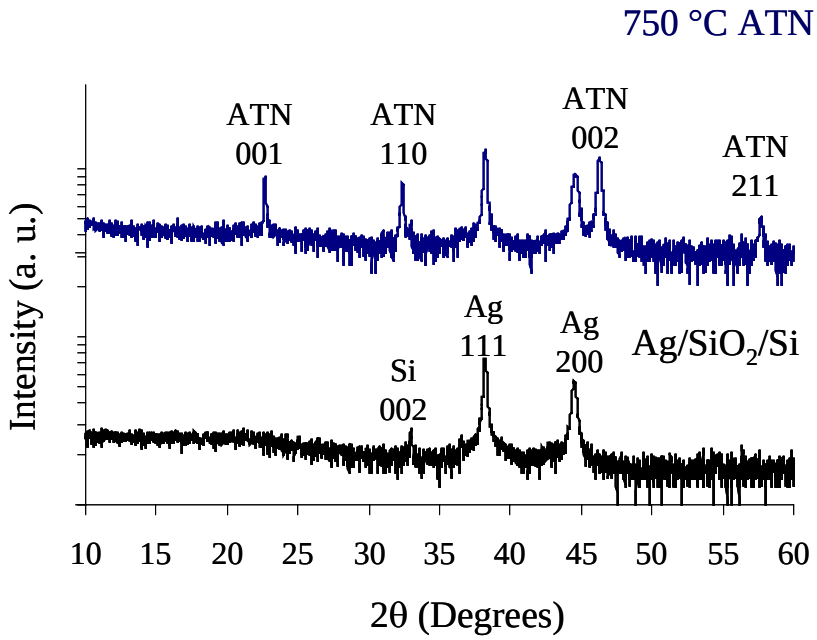


Figure **6.3**: XRD patterns of $Ag/SiO_2/Si$ substrate and 750 °C crystallized ATN film on $Ag/SiO_2/Si$ substrate. Patterns were taken at generator settings of 35 kV and 30 mA.

Getting dielectric data for the ATN film that was deposited on the $Ag/SiO_2/Si$ substrate was also problematic. Hillocking of silver during low temperature hot plate baking steps and peeling of the film/sputtered Ag layer from the $SiO_2/Si$ substrate following Pt top electrode annealing at 500 °C were observed.

## 6.4 Deposition and Crystal Structure Development of $Ag(Ta_{0.5}Nb_{0.5})O_3$ Thin Films on $Ag/Ti/SiO_2/Si$ Substrates:

A thin titanium layer (~20 nm thick) is often used as an adhesion layer between Pt electrodes and $SiO_2/Si$ substrates.[5] In order to test whether Ti could be used as an adhesion layer here, a thin Ti layer (~20 nm thick) was sputtered prior to sputtering the silver layer (~100 nm thick) on $SiO_2/Si$ substrate (Silicon Quest Int., Santa Clara, CA). In order to minimize hillocking observed with use of 450 °C hot plate baking and 700 °C RTA anneals prior to ATN film deposition, the $Ag/Ti/SiO_2/Si$ substrates were kept in a drying oven at 110 °C for 5 sec. to remove any absorbed water prior to film deposition and spun films were crystallized at temperatures from 550 to 750 °C in an $O_2$ ambient without using a 450 °C hot plate baking step (Figure 6.4). None of the ATN films peeled off during Pt top electrode anneals. Thus, use of 20 nm thick Ti layer as an adhesion layer was quite effective in preventing peeling.

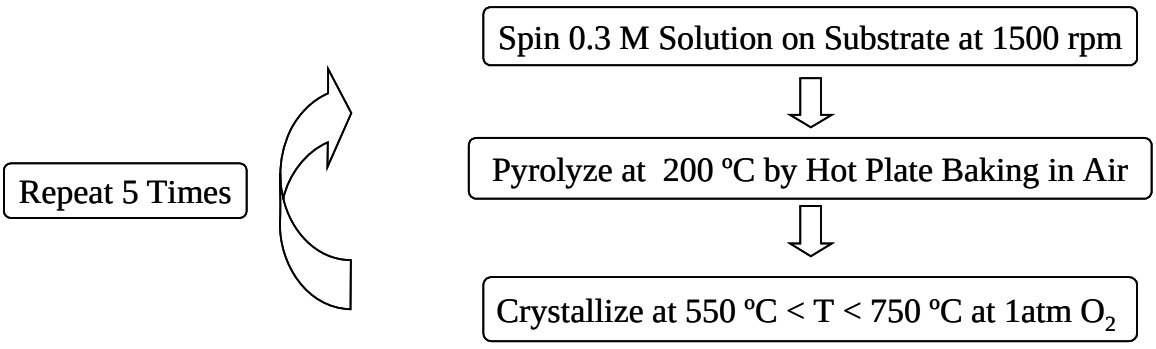


Figure 6.4: Spinning and heat treatments of $Ag(Ta_{0.5}Nb_{0.5})O_3$ films deposited on $Ag/Ti/SiO_2/Si$ substrates.

XRD patterns of ATN films that were deposited on Ag/Ti/$SiO_2$/Si substrate and crystallized between 550 and 750 °C (Figure **6.5**) demonstrated that all the XRD peaks could be explained by a pseudocubic perovskite ATN thin film, Ag and the $SiO_2$/Si substrate. There were no additional XRD peaks suggesting reaction between silver and the ATN films. The relative intensity of the 00*l* family perovskite peaks of the ATN films was weaker than the 00*l* family peaks in the powder ATN XRD file (ICDD 89-7738) when no 450 °C hot plate baking step was used.

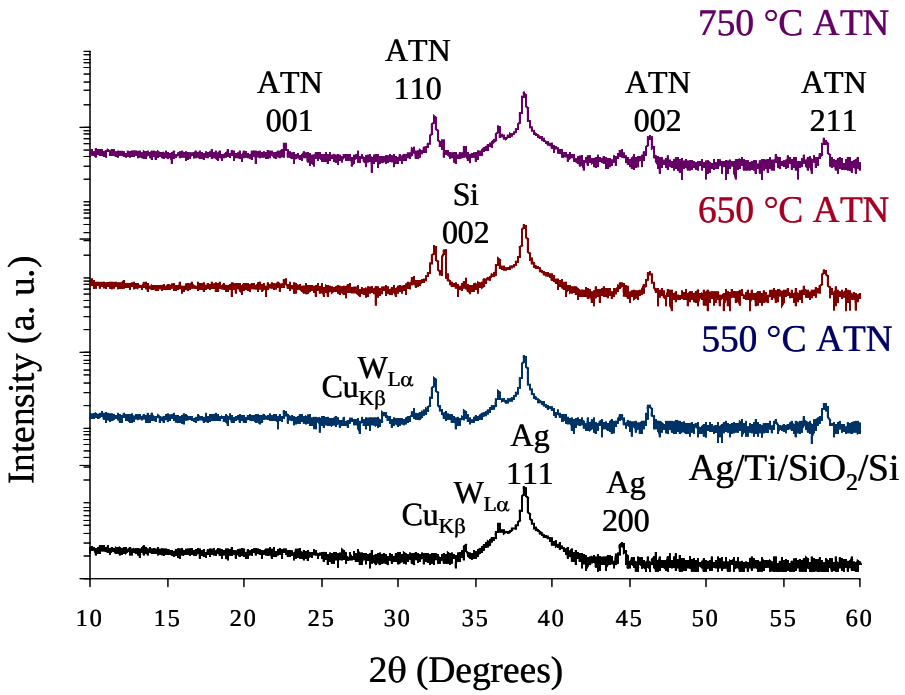


Figure **6.5**: XRD patterns of Ag/Ti/$SiO_2$/Si substrate and ATN films deposited on Ag/Ti/$SiO_2$/Si substrate as a function of crystallization temperature. Patterns were taken at X-ray generator settings of 35 kV and 30 mA.

Hillocking of the silver layer was a problem for the Ag/Ti/$SiO_2$/Si substrate. The light microscope images (Figures 6.6-8) show as sputtered Ag/Ti/$SiO_2$/Si substrate and Ag/Ti/$SiO_2$/Si substrates that were heat treated the same way the ATN films were deposited. While there was not extensive hillocking for the as sputtered substrate (Figure **6.6**) detected within the magnification limits, the substrates that were heat treated at 550 °C (Figure **6.7**) and 750 °C (Figure **6.8**) hillocked extensively.

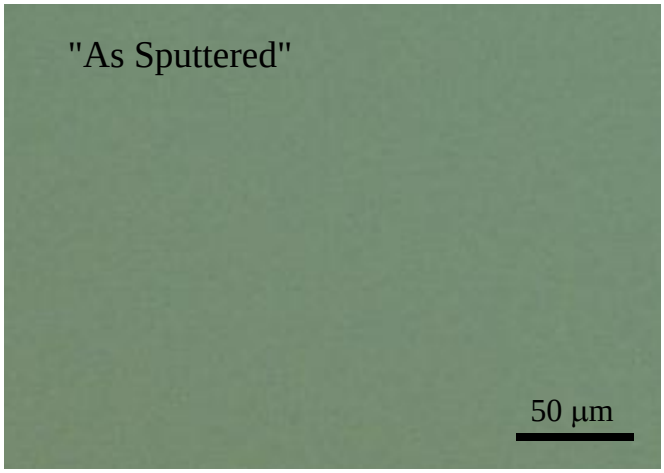


Figure **6.6**: Light microscope image of as sputtered Ag/Ti/$SiO_2$/Si substrate

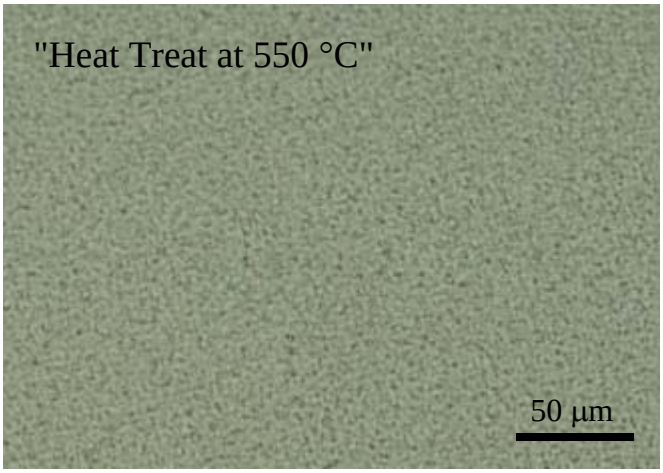


Figure **6.7**: Light microscope image of Ag/Ti/$SiO_2$/Si substrate that was heat treated 5 times at 550 °C for 1 min. in $O_2$ ambient

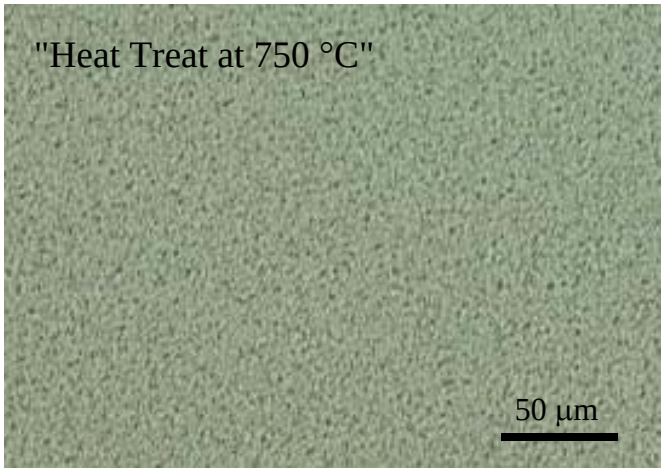


Figure **6.8**: Light microscope image of Ag/Ti/$SiO_2$/Si substrate that was heat treated 5 times at 750 °C for 1 min. in $O_2$ ambient.

Metallic thin films hillocks to relieve intrinsic compressive stresses generated during metallic film deposition and/or during annealing due to the thermal expansion

mismatch between the metal films and substrates.[6, 7] Silver thin films (~110 nm thick) that were evaporated on amorphous silica were reported to hillock when they were annealed at temperatures of 210 °C and higher in an $O_2$ ambient to relieve compressive stresses developed due to thermal expansion mismatch between the silver and amorphous silica.[8] In much the same way, the Si substrate used here has a lower thermal expansion coefficient than Ag, so hillocking is not unexpected.

In order to get dielectric data for the ATN thin films that were deposited on silver or Ag/Ti/$SiO_2$/Si substrates, a smooth silver surface is required to prevent shorts caused by surface roughness or hillocks. Thus, both silver foils and Ag/Ti/$SiO_2$/Si substrates need to have smoother surfaces before they could be used for the dielectric characterization. A smoother silver surface could be achieved for the silver foils by a combination of optimized electropolishing (e.g. using silver and potassium cyanide solution) in addition to mechanical conventional polishing.[9] For the Ag/Ti/$SiO_2$/Si substrates, use of a thicker silver layer may help to reduce hillocking.[8]

It is intriguing that none of the Ag substrates used here promoted formation of the (00*l*) oriented natrotantite phase. It was shown in Chapter 4 that excess Ag in a solution deposited on (111)-oriented Pt favored the oriented natrotantite phase, possibly through a local epitaxial arrangement. Perhaps the main difference here is that all of the Ag surfaces were exposed to air prior to the ATN film deposition. It is possible that the surface oxide that formed prevented the possibility of a structure match, and so facilitated crystallization of the perovskite phase.

## 6.5 Conclusions:

There was no extensive reaction between $Ag(Ta_{0.5}Nb_{0.5})O_3$ thin films and silver when the films were deposited on Ag foils, $Ag/SiO_2/Si$ and $Ag/Ti/SiO_2/Si$ substrates at temperatures from 550 to 750 °C. The crystallographic orientation of the films depended on the type of substrates used and the heat treatment steps followed. While the ATN films had slight 00*l* preferred orientation with a Lotgering factor of 0.24±0.02 when deposited on silver foils, stronger 00*l* preferred orientation with a Lotgering factor of 0.80±0.02 was observed for the film deposited on $Ag/SiO_2/Si$ substrates. However, no 00*l* preferred orientation was observed for the films that were prepared on $Ag/Ti/SiO_2/Si$ substrates without a 450 °C hot plate baking step.

Dielectric characterization of the films was problematic. Surface roughness and polishing difficulties for the silver foils, peeling of film/silver layer from $Ag/SiO_2/Si$ substrates during the top electrode anneal and hillock formation on the $Ag/Ti/SiO_2/Si$ substrates during heat treatment steps prevented electrical measurements. Although the peeling problem for $Ag/SiO_2/Si$ substrates was solved by using a thin (~20 nm thick) Ti adhesion layer, both silver foils and $Ag/Ti/SiO_2/Si$ substrates need to have smoother surfaces before they could be used for dielectric measurements. Electropolishing of silver substrates or optimization of sputtered Ag and Ti layer thicknesses to minimize hillocking may help achieving the smoother silver surfaces required.

## 6.6 References:

[1] K. B. Shim, N. T. Cho, S. W. Lee, "Silver diffusion and microstructure in LTCC multilayer couplers for high frequency applications," *Journal of Materials Science*, **35** 813-820 (2000).

[2] http://www.webelements.com

[3] E. M. Sabolsky, *Grain-oriented $Pb(Mg_{1/3}Nb_{2/3})O_3$–$PbTiO_3$ Ceramics Prepared by Templated Grain Growth*, Ph. D. Thesis, The Pennsylvania State University, 2001.

[4] F. K. Lotgering, "Topotactical reactions with ferrimagnetic oxides having hexagonal crystal structures-I," *Journal Inorganic and Nuclear Chemistry*, **9** 113-123 (1959).

[5] G. Bernhardt, C. Silvestre, N. LeCursi, S. C. Moulzolf, D. J. Frankel, R. J. Lad, "Performance of Zr and Ti adhesion layers for bonding of platinum metallization to sapphire substrates," *Sensors and Actuators B*, **77** 368-374 (2001)

[6] D. Kim, W. D. Nix, R. P. Vinci, M. D. Deal and J. D. Plummer, "Study of the effect of grain boundary migration on hillock formation in Al thin films," *Journal of Applied Physics*, **90** [2] 781-788 (2001).

[7] R. Jakkaraju and A. L. Greer, "Texture and hillocking in sputter-deposited copper thin films," *Journal of Materials Science: Materials in Electronics*, **13** 285-294 (2002).

[8] A. E. B. Presland, G. L. Price and D. L. Trimm, "Hillock formation by surface diffusion on thin silver films," *Surface Science*, **29** 424-434 (1972).

[9] J. K. Zhang, G. N. Okeke and C. H. B. Mee, "Simple apparatus for electropolishing metal single crystals," *Journal of Physics E Scientific Instruments*, **19** [4] 314 (1986).

# Chapter 7

## Conclusions and Future Work

### 7.1 Conclusions:

Chemical solution deposited $Ag_x(Ta_yNb_{1-y})O_z$ thin films on (111)Pt/Ti/$SiO_2$/(001)Si, (001)$LaAlO_3$, (001)$SrRuO_3$/(001)$LaAlO_3$, Ag, Ag/$SiO_2$/(001)Si and Ag/Ti/$SiO_2$/(001)Si substrates were investigated. Deposition of the films involved synthesis of stable chemical solutions, spinning and heat treatments of the spun layers. The crystal structures and phase evolution and dielectric properties developed were found to be affected by the substrate used for deposition and the heat treatment steps followed during crystallization of the films.

Stable chemical solutions of the silver tantalate niobate system, $Ag_x(Ta_yNb_{1-y})O_z$, were synthesized successfully. Stability of niobium and tantalum precursors with the silver precursor was problematic when 2-methoxyethanol was used alone as the solvent, and silver precipitation was observed. Acetic acid modifications of niobium and tantalum precursors did not eliminate the problem. However, prereacting the silver precursor with pyridine produced stable solutions having a wide range of compositions, including the Ag-Ta and Ag-Nb end members and silver deficient compositions compared to Ag-$Ta_{0.5}$-$Nb_{0.5}$ solution.

$Ag(Ta_{0.5}Nb_{0.5})O_3$ films that were deposited on (111)Pt/Ti/$SiO_2$/(001)Si substrates contained a minimum of two phases: a randomly oriented pseudocubic perovskite and a new phase. According to electron diffraction patterns, the new phase had a natrotantite crystal structure with a space group of $R\bar{3}c$ and a composition near $Ag_2(Ta_{0.5}Nb_{0.5})_4O_{11}$. The natrotantite phase had strong (00*l*) preferred orientation when prepared with excess silver. For films batched with a perovskite composition, the natrotantite phase was favored at low temperatures (~ 175 °C) at the platinum-film interface. The material then crystallized rapidly at 550 °C. In contrast, the pseudocubic perovskite phase was favored at crystallization temperatures higher than 550 °C. The crystal structure formation of $Ag(Ta_{0.5}Nb_{0.5})O_3$ films was therefore found to be strongly dependent on the heat treatment steps. While the pseudocubic perovskite phase formation was favored by use of a fast heating rate (100 °C/s) to crystallization temperatures of 550 °C or higher, the natrotantite phase was favored by use of a low temperature heat treatment step (~175 °C) and slow heating rates (5 °C/s) to crystallization temperatures of 550 °C. Although it was possible to affect the extent of these two phases by controlling the heat treatment steps, it was not possible to eliminate the natrotantite phase completely for films having perovskite batch compositions on Pt-coated Si substrates. Phase pure (00*l*) oriented natrotantite films were achieved with a batch composition of $Ag_{0.85}(Ta_{0.5}Nb_{0.5})O_{2.925}$. This composition was silver rich compared to natrotantite composition, $Ag_2(Ta_{0.5}Nb_{0.5})_4O_{11}$.

The dielectric constants of the two phase ATN films were lower than that observed at 100 kHz for ceramics (~ 410). The dielectric constants and losses of the films

were 200±20 and 0.006±0.002 for films crystallized at 550 °C, 270±25 and 0.004±0.002 for the 600 °C film, and 220±20 and 0.002±0.001 for the film crystallized at 750 °C. Natrotantite phase formation at the film-Pt interface was suspected to be the main reason for the lower dielectric constants for two phase ATN films. It was found that all predominantly natrotantite films had lower dielectric constants (70 to 135) than those with the perovskite structure.

$Ag(Ta_{0.5}Nb_{0.5})O_3$ (ATN), $AgTaO_3$ (ATO) and $AgNbO_3$ (ANO) films were prepared on (001)$LaAlO_3$ (LAO) and (001)$SrRuO_3$/(001)$LaAlO_3$ (SRO/LAO) substrates to improve the stability of the perovskite phase. In all cases, (00*l*) epitaxial perovskite phases were obtained at crystallization temperatures of 500 °C and above. The ATN films that were deposited on SRO/LAO substrates had a better crystallinity than those on LAO substrates due to the excellent lattice match between ATN and SRO. Based on XRD intensities, a limited reaction was suspected between the ATN film and SRO, but no reaction was detected between ATN and LAO. The crystallinity of the ATN films improved on both substrates with an increase in crystallization temperatures from 500 to 800 °C. The dielectric constants of ATN films on SRO/LAO substrates also increased from 260±25 to 360±35 at 100 kHz at room temperature with an increase in crystallization temperature. Loss values were ~0.015 at 100 kHz, with the lowest value of 0.007±0.002 observed for films crystallized at 700 °C. For an ATN film that was deposited on SRO/LAO at 750 °C, the frequency dependence of the dielectric properties was small over the measurement range of 1 Hz to 100 kHz. Based on the temperature dependent dielectric constant, the transition between $M_2$ and $M_3$ phases was shifted from

50 °C (bulk ceramic value) to –190 °C for the film. The capacitance change and instantaneous TCC values at 100 kHz were +5.7 % and -0.066 %/°C at –55 °C and –12.1 % and -0.148 %/°C at 120 °C. Linear polarization – electric field traces at room temperature and at –125 °C suggested that the film was not ferroelectric. The DC field tunability was not hysteretic but small, 4.8 % at 100 kHz and 150 kV/cm, due to the limited breakdown strength of 230 kV/cm. The corresponding K factor of the film was low ~3.4 due to limited tunability and relatively high loss. The capacitance change of the film with DC field bias was hysteretic and complex at 77 K.

$AgTaO_3$ (ATO) and $AgNbO_3$ (ANO) films that were deposited on SRO/LAO substrates at 750 °C were well-crystallized into a perovskite-type structure. The ATO film had a slightly lower dielectric constant of 110±10 at 100 kHz at room temperature than the bulk ceramic value of 150. In contrast, the ANO film had a considerably higher room temperature dielectric constant of 550±55 at 100 kHz than the bulk ceramic value of 120. The loss values were 0.025±0.005 for the ATO film and 0.020±0.005 for the ANO film at room temperature. The change in dielectric constant at 100 kHz from its value at 10 Hz was –16.0 % for ATO film and –8.1% for the ANO film. $AgTaO_3$ films had similar temperature dependence in the dielectric response as ceramic samples. In contrast, the $AgNbO_3$ film had high room temperature permittivities, and displayed a slight jump in dielectric constant near 300 °C, suggesting that the ANO films might have either the $M_2$ or the $M_3$ phase at room temperature and either the $M_2$-$M_3$ and the $M_3$–O phase transition at ~300 °C. However, the large shift seen for the $M_2$-$M_3$ phase transition in the $Ag(Ta_{0.5}Nb_{0.5})O_3$ film was not observed for the ANO film. The capacitance change

and corresponding TCC values were –5.6 % and –0.010 %/°C for an ATO film and 1.1 % and 0.011 %/°C for an ANO film at 120 °C at 100 kHz. Both films had linear polarization – electric field responses at room temperature and therefore were not ferroelectric within the applied field range. The room temperature DC field tunability of ATO film was not hysteretic but limited to 1.6 % at 100 kHz and at 230 kV/cm field. The corresponding K factor of 0.6 was the lowest of the investigated silver tantalate niobate film compositions. In contrast, the DC field tunability of the ANO film was higher, with a 12.8 % at a negative bias of -140 kV/cm (where Pt top electrode kept at negative DC bias) and 21.4 % at 190 kV/cm. Higher tunability values also resulted in ANO having the highest K factors among the investigated film compositions. The K-factors of the ANO film were ~6.1 and ~10.2 at negative and positive DC field bias. Use of asymmetric electrodes (top platinum and bottom SRO electrodes) having different leakage current characteristics with $AgNbO_3$ film was suspected to be responsible for the polarity dependence. It is very likely that if the dielectric strength of the films could be improved, ANO films would be viable replacements for BST in tunable dielectric applications.

$Ag(Ta_{0.5}Nb_{0.5})O_3$ thin films that were deposited on Ag foils, $Ag/SiO_2/Si$ and $Ag/Ti/SiO_2/Si$ substrates at temperatures from 550 to 750 °C, did not have any extensive reaction with silver. The orientation of the films was dependent on the substrate used as well as the heat treatment steps. While the ATN films had slight (00*l*) preferred orientation with the Lotgering factor of 0.24±0.02 when deposited on silver foils, stronger (00*l*) preferred orientation with a Lotgering factor of 0.80±0.02 was observed for the film deposited on $Ag/SiO_2/Si$ substrates. However, no 00*l* preferred orientation was

observed for the films that were deposited on $Ag/Ti/SiO_2/Si$ substrates without having a 450 °C hot plate baking step. Although peeling of the $Ag/SiO_2/Si$ substrates was minimized by using a thin (~20 nm thick) Ti layer, both silver foils and $Ag/Ti/SiO_2/Si$ substrates need to be optimized before they could be used for any dielectric data characterization.

## 7.2 Future Work:

There are several areas where it is proposed that additional work should be done, including: a TEM and vibrational spectroscopy investigation to identify the origin of the superlattice reflections and the diffuse scattering observed in the electron diffraction patterns, deposition of natrotantite $Ag_2(Ta_{0.5}Nb_{0.5})_4O_{11}$ films on silver – coated (111) platinum surfaces to understand why excess silver was needed for 00*l* orientation, and a high resolution TEM study to establish any local epitaxial arrangement of the 00*l* oriented natrotantite films relative to (111) platinum layers (with or without Ag coating), deposition of $Ag(Ta_yNb_{1-y})O_3$ films having different Nb/Ta compositions than the studied ones on the $(001)SrRuO_3/(001)LaAlO_3$ substrates to investigate the effects of composition on the dielectric properties, use of different electrodes and investigation of their leakage behavior to improve dielectric breakdown strengths and therefore tunabilities of the films, optimization of silver substrates to investigate dielectric properties of the films deposited on the silver surfaces and investigation of the dielectric properties of the films at high frequencies. These are discussed below.

One of the remaining unanswered questions is the nature of the distortions in the perovskite lattice for the $AgTa_xNb_{1-x}O_3$ films prepared. The ATN phase diagram is a complex one, and there is no available theoretical guidance on how the diagram should be affected by stresses and strains. As a first step, additional transmission electron microscope (TEM) investigations and vibrational spectroscopy studies could be used to identify the origin of the superlattice reflections and the diffuse scattering observed in the electron diffraction patterns of the $Ag(Ta_{0.5}Nb_{0.5})O_3$ films that were deposited on (111)Pt/Ti/$SiO_2$/(001)Si substrates. Comparable studies should be performed on the epitaxial ATN, ATO, and ANO films as a function of temperature to identify the phase transition sequence undergone. Thermodynamic studies of the stability of the ferroic phases under lateral constraints, following the work of Pertsev and Chen could then be performed to determine if the observed phase transition sequence is more strongly influenced by the mechanical boundary conditions, or by other factors such as defect chemistry.[1, 2]

Deposition of natrotantite $Ag_2(Ta_{0.5}Nb_{0.5})_4O_{11}$ films on silver - coated (111) platinum surfaces will be helpful to understand why excess silver was required for the 00*l* orientation. In addition, a high resolution TEM investigation is necessary to establish any local epitaxial arrangement. Alternatively, it would be possible to grow an epitaxial Pt or Ag layer on a (111) oriented perovskite substrate such as $LaAlO_3$ or $SrTiO_3$. The orientation of the natrotantite phase on such a layer could then be investigated using four-circle X-ray diffraction.

The dielectric properties and the shifts observed in the phase transitions strongly depend on the compositions of the films that were deposited on

(001)$SrRuO_3$/(001)$LaAlO_3$ substrates. While there is a big shift (~250 °C) in the $M_2$-$M_3$ phase transition for the $AgTa_{0.5}Nb_{0.5}O_3$ film, no such big shift was observed for $AgTaO_3$ and $AgNbO_3$ films. However, the dielectric permittivity of the $AgNbO_3$ film at room temperature is higher than the room temperature values reported for bulk samples. In order to understand the compositional dependence of the dielectric properties of the films and the shifts observed in phase transitions, films having different Nb/Ta ratios (especially having high Nb/Ta ratios, where high tunabilities were seen) need to be investigated on (001)$SrRuO_3$/(001)$LaAlO_3$ substrates. This will also facilitate selection of optimized Nb/Ta compositions having required dielectric constants and tunabilities for different applications. In addition, tunability measurements for the films should be performed at various temperatures to determine if the tunability, like the dielectric constants, shows acceptable temperature stability.

If the dielectric breakdown strength of the films is improved, the tunability of the films might be increased by applying higher DC fields. Both the leakage characteristics and the ultimate dielectric breakdown strength of films often depend on the type of the electrodes used.[3] At present, the majority carrier type in the films is not known, nor is it clear whether electronic or ionic carriers dominate the failure. Consequently, it is suggested that the field-dependence of the leakage current of the films be monitored to determine the conduction mechanism. This would be done in part by measuring the leakage characteristics with other top electrode materials with different work functions such as Al, Ag and Au. Measurements would also need to be made as a function of temperature. Once the conduction mechanism is known, it will be clearer whether or not it is possible to engineer improved leakage behavior into ATN dielectric films.

In addition, it would be important to investigate the primary failure mechanism under long-term dc bias exposure. There are two potentially mobile ionic defects that may be important, oxygen vacancies and silver vacancies. To examine the feasibility of using silver tantalate niobate films for tunable applications, highly accelerated lifetime tests should be conducted, and the failure mode identified. It will be particularly important to determine if either ionic defect has a high mobility. If so, then doping of the films to control vacancy contents and mobilities will be necessary.

It would also be interesting to investigate further the lower temperature characteristics of all of the Ag-containing perovskite films. Of particular interest would be a determination of the phase diagram as it pertains to ferroelectric distortions. In cases where ferroelectricity is suspected, checking the pyroelectric response of the films will provide a measure of the magnitude of the available polarization.

For dielectric data characterization of the $AgTa_xNb_{1-x}O_3$ films that were deposited on silver surfaces, either electropolishing of the Ag foil or optimization of $Ag/Ti/SiO_2/(001)Si$ substrates needs to be done. Electropolishing requires toxic potassium and silver cyanide solutions.[4] Therefore, optimization of $Ag/Ti/SiO_2/(001)Si$ substrates seems to be a more reasonable way to achieve smoother silver surfaces. Increasing the silver layer thickness was shown to reduce the compressive stresses developed in evaporated silver layers on silica substrates and may also help to reduce hillocking observed with $Ag/Ti/SiO_2/(001)Si$ substrates.[5] After minimization of the massive hillocking observed, deposition of $AgTa_xNb_{1-x}O_3$ films might still need to be modified. Elimination of hot plate baking steps and crystallization of spun films directly might be helpful to keep the silver layer from further hillocking.

The dielectric properties of the films including tunabilities need to be characterized at the high frequencies (1-40 GHz) for films to be considered for device applications. Figure 7.1 shows main types of dielectric property characterization techniques and their typical frequency limitations.[6] A combination of reflection coefficient measurements using a network analyzer and resonance methods such as transmission line resonator might be necessary to cover the anticipated frequency range.

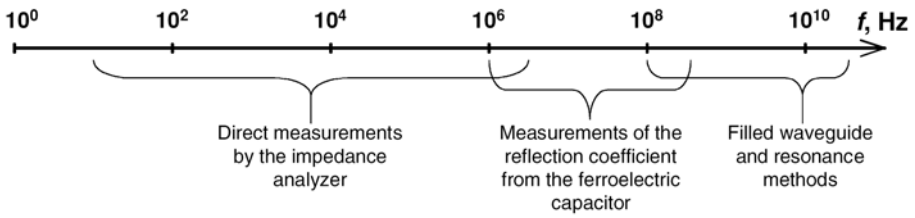


Figure 7.1: Frequency range of applicability of the main types of techniques used for dielectric characterization of materials.[6]

## 7.3 References:

[1] M. A. Pertsev, A. G. Zembilgotov and A. K. Tagantsev, "Effect of mechanical conditions on phase diagrams of epitaxial ferroelectric thin films," *Physical Review Letters*, **80** [9] 1988-1991 (1998).

[2] S. Y. Chen and H. Y. Lu, "Sintering and compensation effect of donor- and acceptor codoped 3 mol % $Y_2O_3$-$ZrO_2$," *Journal of Materials Science*, **27** 4791-4796 (1992).

[3] I. Stolichnov, A. Tagantsev, N. Setter, S. Okhonin, P. Fazan, J. S. Cross and M. Tsukada, "Dielectric breakdown in (Pb,La)(Zr,Ti)$O_3$ thin films with Pt and oxide electrodes," *Journal of Applied Physics*, **87** [4] 1925-1931 (1999).

[4] J. K. Zhang, G. N. Okeke and C. H. B. Mee, “Simple apparatus for electropolishing metal single crystals,” *Journal of Physics E Scientific Instruments*, **19** [4] 314 (1986).

[5] A. E. B. Presland, G. L. Price and D. L. Trimm, “Hillock formation by surface diffusion on thin silver films,” *Surface Science*, **29** 424-434 (1972).

[6] A. K. Tagantsev, V. O. Sherman, K. F. Astafiev, J. Venkatesh and N. Setter, “Ferroelectric materials for microwave tunable applications,” *Journal of Electroceramics*, **11** 5-66 (2003).

# VITA

Mustafa Burak Telli was born in Malatya, Turkey on September 25, 1971. He graduated from The Middle East Technical University, Ankara, Turkey with a B.S. degree in Metallurgical Engineering (1993). He came USA in 1996 to pursue his M.S. and Ph. D. in Materials Science and Engineering. He received his M.S. degree in Materials Science and Mechanics at The Michigan State University in 1998 and his Ph. D. degree in Materials Science and Engineering at The Pennsylvania State University in 2005. He presented his research work in meetings and conferences such as Center for Dielectric Studies Meetings, Materials Research Society Meetings and American Ceramic Society Conference. He is currently a member of the American Ceramic Society.